Modeling wind forcing in phase resolving simulation of nonlinear wind waves

by

Alexander G. Kalmikov

B.Sc., Physics and Mathematics, The Hebrew University of Jerusalem, 1999

M.Sc., Geophysics and Planetary Sciences, Tel-Aviv University, 2006

Submitted to the Department of Mechanical Engineering in partial fulfillment of the requirements for the degree of

MASTER OF SCIENCE

in Mechanical and Oceanographic Engineering

at the

MASSACHUSETTS INSTITUTE OF TECHNOLOGY

and

WOODS HOLE OCEANOGRAPHIC INSTITUTION

February 2010

Signature of Author: _____

Joint Program in Oceanography/Applied Ocean Science and Engineering
Department of Mechanical Engineering, MIT
November 30, 2009

Certified by: _____

Dick K.P. Yue
Philip J. Solondz Professor of Mechanical and Ocean Engineering
Thesis Supervisor

Accepted by: _____

James C. Preisig
Associate Scientist, Department of Applied Ocean Physics and Engineering, WHOI
Chair, MIT/WHOI Joint Committee on Applied Ocean Science and Engineering

Accepted by: _____

David E. Hardt
Ralph E. and Eloise F. Cross Professor of Mechanical Engineering
Chairman, Committee on Graduate Students

Modeling wind forcing in phase resolving simulation of nonlinear wind waves

by

Alexander G. Kalmikov

Submitted to the Department of Mechanical Engineering on November 30, 2009
in partial fulfillment of the requirements for the Degree of Master of Science in
Mechanical and Oceanographic Engineering

ABSTRACT

Wind waves in the ocean are a product of complex interaction of turbulent air flow with gravity driven water surface. The coupling is strong and the waves are non-stationary, irregular and highly nonlinear, which restricts the ability of traditional phase averaged models to simulate their complex dynamics. We develop a novel phase resolving model for direct simulation of nonlinear broadband wind waves based on the High Order Spectral (HOS) method (Dommermuth and Yue 1987). The original HOS method, which is a nonlinear pseudo-spectral numerical technique for phase resolving simulation of free regular waves, is extended to simulation of wind forced irregular broadband wave fields. Wind forcing is modeled phenomenologically in a linearized framework of weakly interacting spectral components of the wave field. The mechanism of wind forcing is assumed to be primarily form drag acting on the surface through wave-induced distribution of normal stress. The mechanism is parameterized in terms of wave age and its magnitude is adjusted by the observed growth rates. Linear formulation of the forcing is adopted and applied directly to the nonlinear evolution equations.

Development of realistic nonlinear wind wave simulation with HOS method required its extension to broadband irregular wave fields. Another challenge was application of the conservative HOS technique to the intermittent non-conservative dynamics of wind waves. These challenges encountered the fundamental limitations of the original method. Apparent deterioration of wind forced simulations and their inevitable crash raised concerns regarding the validity of the proposed modeling approach. The major question involved application of the original HOS low-pass filtering technique to account for the effect of wave breaking. It was found that growing wind waves break more frequently and violently than free waves. Stronger filtering was required for stabilization of wind wave simulations for duration on the time scale of observed ocean evolution. Successful simulations were produced only after significant sacrifice of resolution bandwidth.

Despite the difficulties our modeling approach appears to suffice for reproduction of the essential physics of nonlinear wind waves. Phase resolving simulations are shown to capture both - the characteristic irregularity and the observed similarity that emerges from the chaotic motions. Energy growth and frequency downshift satisfy duration limited evolution parameterizations and asymptote Toba similarity law. Our simulations resolve

the detailed kinematics and the nonlinear energetics of swell, windsea and their fast transition under wind forcing. We explain the difference between measurements of initial growth driven by a linear instability mechanism and the balanced nonlinear growth. The simulations validate Toba hypothesis of wind-wave nonlinear quasi-equilibrium and confirm its function as a universal bound on combined windsea and swell evolution under steady wind.

Thesis Supervisor: Dick K.P. Yue
Title: Philip J. Solondz Professor of Mechanical and Ocean Engineering

Acknowledgment

I would like to thank my advisor, Professor Dick K. P. Yue, for giving me the opportunity to contribute to nonlinear wind wave research. I am grateful to Professor Yue for introducing me to engineering, for his valuable guidance, generous support and practical advice throughout this project. I would also like to thank my teachers Professor Triantaphyllos R. Akylas and Professor Chiang C. Mei for teaching me the fundamentals of nonlinear wave hydrodynamics with much rigor and insight, and Dr John Trowbridge and Dr Gene Terray for introducing me to the exciting field of Air-Sea interaction. Special thanks to my colleagues Wenting Xiao and Grgur Tokic for many insightful discussions which significantly contributed to the research reflected in this thesis. This research was supported by the Office of Naval Research and by the MIT/WHOI Joint Program.

Table of contents

"It seems much more difficult to utilize in truly constructive ways the methods and techniques of hydrodynamic simulations than to develop them. However, the yield from successful numerical experiments can be very high ..." M.P. Tulin, 2003.

Chapter 1. Introduction

Gravity waves on ocean surface are a powerful phenomenon of central importance in ocean engineering (Mei, Stiassnie and Yue 2005). Surface waves are also a major factor in ocean-atmosphere interaction with significant implications on weather and climate dynamics (Csanady 2001). Mechanical energy contained and dissipated in surface waves is the largest component in the energetics of global oceans (Wang and Huang 2004). Most of this energy is transferred to waves by the action of wind, and these waves are known as *wind waves* (Kinsman 1965).

Study of wind blowing waves is a classical problem in hydrodynamics. Early standardized descriptions of wind forcing in the sea can be traced back to 1806 when Beaufort Wind Force Scale was first documented (Kinsman 1969). Theoretical attempts to explain the process of wind-wave generation (Helmholtz 1868, Thomson 1871) as well as the general dynamics of surface waves (see Craik 2004, 2005 for a review of early 19^{th} century progress) attracted considerable attention from the earliest days of study of physics of fluids. Yet, in 1956 in a widely quoted critical review Ursell concluded that "the present state of our knowledge is profoundly unsatisfactory". This review inspired extensive research activity and many profound developments took place in last 50 years. Nevertheless, in 2006 Donelan, Babanin, Young and Banner reviewed this progress and concluded that the current state of knowledge is "incomplete and often contradictory", "no fully consistent and conclusive theory of wave generation by wind exists", the suggested theoretical mechanisms are "sometimes incompatible", the available experimental data is "scattered by an order of magnitude and the parameterizations result in estimates that can differ by more than 100%". Therefore, wind-blown waves appear to

remain a 200 year old unresolved problem, while modern applications provide an increasing demand for their better understanding and high precision modeling.

Contemporary state of the art wind-wave models (Cavaleri et al. 2007, Komen et al. 1994) are based on statistical formulation. The surface of the ocean is assumed to be a random wavefield comprised of statistically independent spectral components. The wavefield is assumed to be represented by a stationary random process and only statistically relevant properties are being quantified. The description is *phase averaged* in the sense that only power spectrum is considered, the phases of the spectral components are disregarded. Thus, the actual geometry and kinematics of the wave field are not described and quantitative statements are only of probabilistic nature. These statistical models do not fully account for the nonlinearity of wind forced wave field. Their formulation is based on linearized description and superposition principle extended to only partially account for weak interactions and broadband effects (Kinsman 1965). A simple example is the fact that they consider only linear estimates of energy and momentum (Komen et al. 1994). Effects beyond the ability of these models, like modulations and non-resonant nonlinear interactions start being recognized in the recent literature (Janssen 2003).

On the other hand, advanced theoretical methods and elaborate numerical wave tanks have been developed to study the phase resolved dynamics of nonlinear surface waves (Tsai and Yue 1996, Dias and Bridges 2006). However, application of these models to the real ocean wind-wave problem is severely limited due to high computational cost and oversimplifying theoretical assumptions.

The objective of this thesis is to develop a numerical model for direct simulation of ocean wind waves. Our mechanistic approach is based on basic principles and is set in phase resolving framework. Unlike the contemporary phase averaged models we do not imply random phase approximation or ergodic statistical ensembles. Model formulation starts from the primitive equations and explicitly resolves the dynamics, kinematics and geometry of nonlinear wave surface. We utilize the High Order Spectral (HOS) method (Dommermuth and Yue 1987), which is a pseudo-spectral numerical technique for phase

resolving simulation of free regular waves in periodic domain. In this thesis we extend this technique to simulation of wind forced irregular quasi-periodic wave fields. The two principal contributions to the HOS method are, therefore, development of suitable wind forcing model for HOS and development of broadband irregular wavefield simulation capabilities for the method.

The proposed wind forcing model is physics based. We review the observed physics of wind waves, focusing on the modern concept of windsea and its similarity properties. We base the phenomenological framework for development of the model on observed growth laws of windsea and parameterize the evolution in terms of wave age. Wind forcing mechanism is shown to be primarily a wave induced form drag due to slope coherent surface pressure distribution. Linear formulation of the forcing is adopted and applied directly to the nonlinear evolution equations.

The attempts of extension of the HOS method to simulation of broadband irregular wavefield encountered the basic limitations of the original method. We examine the advantages and drawbacks of the proposed phase-resolving model formulation. The major weakness is identified in the inadequacy of the original HOS approach to consistently account for the effect of wave breaking when the conservative dynamics of free regular waves are substituted by the intermittent non-conservative physics of irregular wind waves. The original low-pass filtering technique is shown to have effects which are not consistent in the existing theoretical framework and raise concerns regarding the validity of our modeling approach. Nonetheless, we discover that the results of our simulations are consistent with the observed similarity laws of wind waves, which suggests that our modeling approach is sufficient to reproduce the relevant wind wave physics.

Our analysis of the successful simulations advances understanding of the observed wind wave physics and contributes to study of wind-wave interaction mechanisms. The nonlinear non-conservative wind wave simulations lay a basis for development of advanced nonlinear phase resolving models of wind forcing on waves. The simulations clarify the observed dynamics of ocean swell and windsea, and explain the process of

their transition under wind forcing. The proposed nonlinear phase resolving simulation method is shown to have the computational capabilities and basic theoretical coherence for development of new generation of highly accurate realistic wind wave forecasting models.

Chapter 2. Background

2.1. *Wind wave physics*

2.1.1. Modern view of wind waves: Windsea and Swell

Wind waves are the most energetic type of gravity waves on ocean surface if compared to tides and seismic waves (Kinsman 1965, p. 23). Wind wave category, which includes gravity waves, capillary waves, infra- and ultra-gravity waves is energetically dominated by pure gravity waves with periods of 1-30 seconds. Oceanographers distinguish between two types of these waves – swell and "windsea" (or "sea" in older nautical literature). Swells are round and smooth. These are regular waves propagating on calm ocean surface away from regions of strong winds. Wave breaking is relatively rare, turbulence and white capped regions are limited. Windsea, in contrast, is characterized by steep, rough and irregular surface waves continuously generated by the action of wind at the air-sea interface. Wave breaking is frequent, white caps cover significant portions of the surface. The distinction between the two types is parallel to distinction between free and forced waves. Indeed, swells have been proved to be reasonably well described as superposition of infinitesimal spectral components, governed by linear theory and weakly nonlinear interactions. Windsea, however, is a different more complicated phenomenon inherently coupled to the forcing of wind. The actual wind waves are "extremely intricate blending of free and forced waves" (Kinsman 1965, p. 24) and their physics is very complicated – "Many details are indistinct, and the parts played by the various dynamical processes involved are clearly not simple, changing constantly as the waves develop. Indeed, a dynamical kaleidoscope!" (Phillips 1977, p. 170).

Modern view of wind waves (Csanady 2001; Toba 1998, 2003), we will now use this term to generally refer to "windsea", is different from earlier conceptual model seeing them as stochastic "assembly of freely propagating gravity waves, independent of and unaffected by the air-water shear flow" (Csanady 2001, p. 61). That simplification to an ergodic ensemble of independent infinitesimal linear free waves is the legacy of the outdated theories of Sverdrup, Munk, Peirson and Newman (see Kinsman 1965). "Wind

waves are very special phenomena, which are generated at a sheared interface between the air and water, and which connect two turbulent boundary layers of air and water" (Toba 1998). The coupling of these two different viscous fluids is strong and nonlinear. Waves are inherently forced by the wind, break intermittently and interact strongly with surrounding turbulence. This nonlinear non-stationary dynamics is substantially different from what is described by the theory of free surface waves, the special characteristics of wind waves may not be expressed merely as a combination of gravity and capillary waves. However, within all the irregularity and chaotic complexity of the detailed motions wind waves appear to satisfy simple macroscopic laws.

2.1.2. Wind forced evolution and wave age

Observations of wind waves evolving under the forcing of wind reveal two primary features: waves grow to become higher and longer. To simplify the description of the complex evolution observed in the real situations, two idealized settings are customarily introduced. In *fetch limited* conditions constant wind is assumed to blow for sufficiently long time, so that the state of the wave field is only dependent on the length of the upwind domain. In *duration limited* conditions the upwind domain is assumed to be unlimited, constant wind starts to blow waves on a clam water surface and wave field depends only on the duration of this wind. In these idealized settings the development of wave field is described by energy growth and frequency downshift. Although for infinitesimal periodic waves these processes can be straightforwardly quantified within the framework of linear theory, for the irregular broadband ocean wavefield the measure of these processes requires spectral consideration.

Energy growth is interpreted geometrically in view of its leading order estimate by the variance of wave elevation record, or twice potential energy, in other words. The growing variance is traditionally quantified by significant wave height, which measures the observed crest to trough distance:

$$H_s \approx 4\sigma \tag{2.1.1}$$

Here $\sigma = \sqrt{\overline{\eta^2}}$ is the standard deviation of the surface about its mean elevation. The observed growth of wave elevation amplitude is explained, in principle, by the existing linear theories of wind-forced wave growth (e.g. Miles 1957), as will be discussed in the subsequent sections in this chapter.

The other aspect of the observed wave growth - the increase of wave length is not explained by the linear theory. Neither is it easily quantified for broadband irregular waves. As waves develop under action of wind, their characteristic horizontal scale appears longer and their spectrum is shifted to lower frequencies. This frequency downshift, which by the linear dispersion relation is equivalent to wavelength growth and phase velocity acceleration, is traditionally quantified in terms of a "dominant" wave. This wave is typically associated with the peak of the measured power spectrum or, alternatively, is estimated by zero crossing methods (Sverdrup and Munk 1947). The concept of dominant wave is not unambiguously defined; its popular definition in terms of spectral maximum depends on artificial smoothing of realistic spectra and assumption of their narrowbandedness. Dominant wave is an approximate construct introduced by the necessity to describe the scale of broadband irregular ocean waves by single parameter. Nonetheless, the concept was proven to be very useful in many observational studies as well as in phase averaged spectral theoretical approaches.

The process of frequency downshift of growing wind waves is so ubiquitous in the ocean that it became a standard for quantifying the stage of wave system evolution. Nondimensionalized by gravity and strength of the wind, expressed by friction velocity u_*, the inverse of peak frequency is equal to nondimensional phase velocity of the peak.

$$\frac{c_p}{u_*} = \frac{g}{\omega_p u_*} \tag{2.1.2}$$

The ratio of peak phase velocity to wind strength is known as *wave age*. The concept expresses the fact that older waves propagate faster relative to the wind. In alternative form (2.1.3) wave age is scaled by wind speed at standard height, typically 10 m over the

mean level. The conversion between definitions is done with drag coefficient $C_D = O(10^{-3})$.

$$\frac{c_p}{U_{10}} = \sqrt{C_D}\frac{c_p}{u_*} \tag{2.1.3}$$

This parameterization of wind wave evolution in terms of relative propagation speed appears to capture the key observed physics. Young waves grow from short capillary ripples, that appear quickly on a smooth surface when turbulent wind starts blowing. Young waves are slow, relatively steep and have appearance of local roughness. As they grow under continuous wind forcing, waves get higher, longer and less steep. They propagate faster and accelerate until reaching speed a little higher than the wind, i.e. wave age $c_p/U_{10} \approx 1.14$ (Csanady 2001). At this stage waves are considered to be mature, the efficiency of wind forcing is reduced, waves reach equilibrium of "full development".

It appears that although the concept of wave age and the process of frequency downshift are central in observational wind wave studies, their theoretical explanation is an open and intriguing question. Not only that frequency downshift is not explained by the linear theory, its actual process is not smooth and gradual but appears to be surprisingly complex. Wave lengthening process is observed to be discrete and abrupt, and became known as "crest pairing" or "phase reversal" events (Lake and Yuen 1978, Melville 1983, Shugan and Voliak 1998). Its physical mechanism is a subject of current controversy, apparently due to inability to be properly explained in existing theoretical frameworks. It may be hypothesized that the explanation lies within phase resolving framework, and this thesis may be regarded as a demonstration of a possible quantitative approach. Further point to make is that frequency downshift was observed and studied for both free (Melville 1983, Trulsen and Dysthe 1997) and wind forced (Hara and Mei 1991) waves, the separate effect of wind on this process is not currently known. This fact undermines the validity of frequency based wave age parameter as a unique quantifier of wave evolution under wind. The details of frequency downshift mechanisms have to be better

understood, the roles of nonlinear interactions, wind forcing and dissipation need to be separated. This thesis is, therefore, a step in resolving this fundamental question.

2.1.3. Dimensional analysis and observed growth laws

Before we turn to a quantitative discussion of the observed energy growth and frequency downshift we resort to dimensional analysis. We identify six independent quantities of interest: variance of surface elevation record (or equivalently significant wave height), characteristic frequency (e.g. frequency of spectral peak), wind speed, gravity acceleration g, fetch and duration of the wind; and two fundamental dimensions – length and time. Buckingham π theorem indicates that four dimensionally independent nondimensional parameters can be combined. These four parameters are (Kitaigorodskii 1962, Young 1999): nondimensional energy, nondimensional frequency, nondimensional fetch and nondimensional duration

$$\varepsilon \equiv \frac{g^2\sigma^2}{U_{10}^4}, \quad \nu \equiv \frac{U_{10} f_p}{g}, \quad F \equiv \frac{gx}{U_{10}^2}, \quad \tau \equiv \frac{gt}{U_{10}} \tag{2.1.4}$$

Alternatively, if friction velocity is chosen to represent wind strength, a similar nondimensional group is:

$$E_* \equiv \frac{g^2\sigma^2}{u_*^4}, \quad \omega_* \equiv \frac{u_* \omega_p}{g}, \quad F_* \equiv \frac{gx}{u_*^2}, \quad \tau_* \equiv \frac{gt}{u_*} \tag{2.1.5}$$

Both scaling standards appear in the literature and, for convenience, will be used below. Conversion between the groups is done with drag coefficient, defined

$$C_D \equiv \left(\frac{u_*}{U_{10}}\right)^2 = O(10^{-3}) \tag{2.1.6}$$

The great progress in observational studies of wind waves was achieved by parameterizing the measured energy growth and frequency downshift in idealized fetch limited conditions

$$\varepsilon = f_1(F), \quad \nu = f_2(F) \tag{2.1.7}$$

f_1 and f_2 are empirically determined universal functions. Theoretically, in idealized duration limited conditions the evolution equations would be

$$\varepsilon = f_3(\tau), \quad \nu = f_4(\tau) \tag{2.1.8}$$

However, such conditions are rare in the real oceans and consequently the amount and quality of available duration limited evolution parameterizations is limited.

Many observational studies of fetch limited growth laws appear in the literature (see Young 1999, p. 101), most frequently cited is the JONSWAP experiment (Hasselmann et al. 1973). JONSWAP fetch limited energy growth and frequency downshift are given by

$$\varepsilon = 1.6\times10^{-7} F, \quad \nu = 3.5F^{-0.33} \tag{2.1.9}$$

Duration limited growth laws are hard to observe; typically conversion from fetch to duration is reported. A simple parameterization was proposed by CERC (1984)

$$\tau = 68.8F^{0.67} \tag{2.1.10}$$

It should be noted however, that the scatter of measurements is large and the above parameterization is useful mainly for order of magnitude estimates.

The inhomogeneity of wind wave evolution conditions in the real ocean limits the applicability of the idealized fetch and duration limited parameterizations. To overcome these limitations Donelan et al. (1985) chose to report their measurements using "local scaling" in terms of wave age. Their growth law appears in following form:

$$\varepsilon = 0.00274\left(\frac{U_{10}}{c_p}\right)^{-3.3} \tag{2.1.11}$$

The observed relation between fetch and inverse wave age is reported as

$$\frac{U_{10}}{c_p} = 11.6F^{-0.23} \tag{2.1.12}$$

Combination of (2.1.11) and (2.1.12) leads to Donelan et al. (1985) version of fetch limited growth laws, which are only generally consistent with JONSWAP parameterization (2.1.9).

$$\varepsilon = 8.4\times10^{-7} F^{0.76}, \quad \nu = 1.85F^{-0.23} \tag{2.1.13}$$

Duration limited growth estimates can be obtained from Donelan et al. (1985) data by combining (2.1.10) with (2.1.12) and then (2.1.11)

$$\varepsilon = 7\times10^{-9}\tau^{1.13}, \qquad \nu = 8\tau^{-0.34} \tag{2.1.14}$$

Duration–wave age relation for CERC parameterization with Donelan et al. (1985) data is

$$\frac{U_{10}}{c_p} = 50\tau^{-0.34} \tag{2.1.15}$$

This approximate result may be utilized to estimate the required evolution time for duration limited numerical simulations. Rewritten, for convenience, in terms of scaled simulation time (see Chapter 4) (2.1.15) becomes

$$\frac{t}{T_p} = \tau\nu = 1.4\times10^{4}\left(\sqrt{C_D}\frac{c_p}{u_*}\right)^{1.9} \tag{2.1.16}$$

The estimated evolution of wave age is plotted versus scaled duration on Figure 2.1. We conclude that the time scale relevant to wave age parameterized wind wave evolution is $O(10^3 T_p)$.

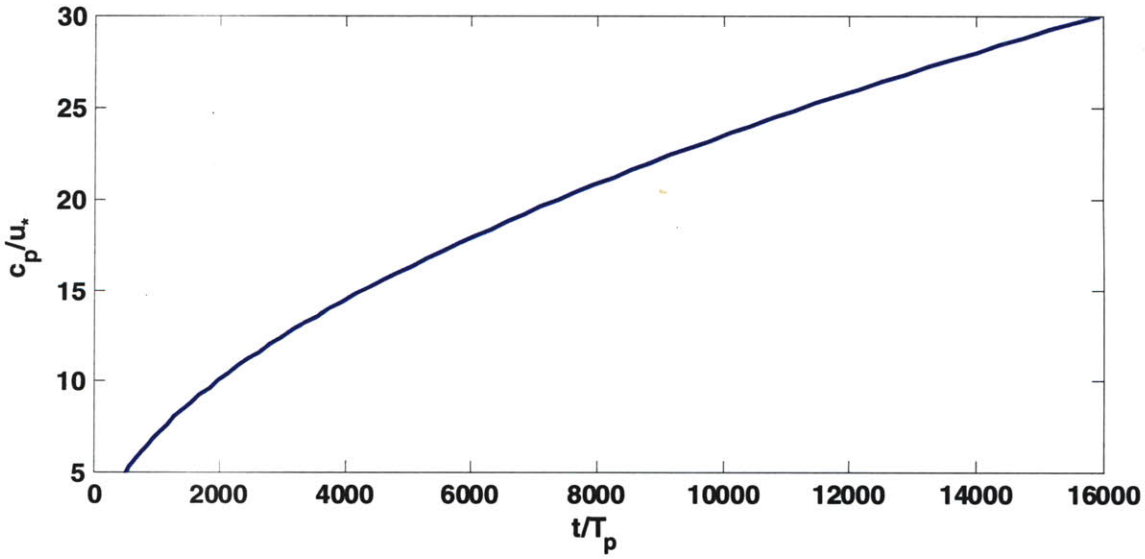

Figure 2.1 Wave age evolution vs. scaled simulation time based on CERC (1984) and Donelan et al. (1985) parameterizations.

2.1.4. Observed spectral parameterizations

In previous section we discussed empirical growth laws in terms of 2 integral parameters – wave energy and characteristic frequency. Here we consider empirical evolution of power spectra that resolve the details of energy distribution between the different frequencies of the growing wave field. Application of similarity theory and dimensional analysis (Kitaigorodskii 1973, p. 126) for wave spectra governed by gravity and wind suggests the nondimensional scaling $\frac{\phi(\omega)g^3}{u_*^5}$ and a similarity law for the asymptotic state of "fully developed" windsea

$$\frac{\phi(\omega)g^3}{u_*^5} = func.\left(\frac{u_*\omega}{g}\right). \qquad (2.1.17)$$

Observations of Pierson and Moskowitz (1964) confirm this analysis as nondimensionalized spectra collapse on a single universal curve (Kitaigorodskii 1973, p. 129).

For developing seas no single universal curve exists, but rather evolving nondimensional spectra have self-similar structure which can be parameterized by a single evolution parameter like the fetch. The form of similarity law becomes, under constant wind and in absence of swell,

$$\frac{\phi(\omega)g^3}{u_*^5} = func.\left(\frac{u_*\omega}{g}, \frac{gx}{u_*^2}\right). \qquad (2.1.18)$$

The primary properties of the universal evolving spectra are downshift and integral energy growth.

Earlier, Phillips (1958) used dimensional analysis to argue that since spectral saturation range* is governed only by gravity, the power spectrum should be nondimensionalised as $\frac{\phi(\omega)\omega^5}{g^2}$ and the universal shape of the spectral tail should have -5 power form. This

* In the original Phillips' 1958 paper the term "equilibrium range" was erroneously used to refer to "saturation range". This discrepancy was later clarified by Phillips in 1985 paper, were an improved description of "equilibrium range" was provided.

spectral form was considered a standard in the earlier years and experimental studies were forced to fit this power law. The widely cited JONSWAP parameterization (Hasselmann et al. 1973) is an example of such approach.

Toba's observations of 3/2 power law (see Section 2.1.5.) led him to propose on empirical grounds an alternative -4 power law for the spectral tail (Toba 1973). The consistency argument is based on integration of the spectral tail, that would suggest -3 power variation of the total energy with the lower bound of integration – i.e. the spectral peak. This form was justified dimensionally by modifying Phillips (1958) argument, assuming equilibrium range dependence on both gravity and wind stress, such that scaling $\frac{\phi(\omega)\omega^4}{u_* g}$ law becomes . Theoretically -4 power law is supported by works of Zakharov and Filonenko (1966), Kitaigorodskii (1983) and Phillips (1985). More modern observations confirmed the validity of Toba spectral form (e.g. Donelan et al. 1985) and it was even shown to better fit the original JONSWAP data (Battjes et al. 1987).

In current work the above three types of observed spectral parameterizations were applied and utilized for initial conditions. Pierson and Moskowitz (1964) spectrum at the asymptotic fully developed limit has the older -5 power tail. Converted to wavenumber nondimensional form it is given by

$$S_{PM}(k)k_p^3 = \frac{\alpha}{2}\left(\frac{k}{k_p}\right)^{-3} \exp\left[-\frac{5}{4}\left(\frac{k}{k_p}\right)^{-2}\right] \qquad (2.1.19)$$

Here k_p is the wavenumber of the spectral peak. The parameter α is known as Phillips' constant (Phillips 1958) and has the interpretation of the total spectral energy level of the wave field. For mature Pierson-Moskowitz (hereafter PM) windsea its value is fixed to $\alpha = 0.0081$.

The fetch limited parameterization for growing windsea of JONSWAP experiment (Hasselmann et al. 1973) is given by

$$S_J(k)k_p^3 = \frac{\alpha}{2}\left(\frac{k}{k_p}\right)^{-3} \exp\left[-\frac{5}{4}\left(\frac{k}{k_p}\right)^{-2}\right] \cdot \gamma_J^{\exp\left[-\frac{-1}{2\sigma^2}\left(\sqrt{\frac{k}{k_p}}-1\right)^2\right]} \tag{2.1.20}$$

$$\alpha = 0.033\nu^{0.67}$$

$$\gamma_J = 3.3$$

$$\sigma = \begin{cases} 0.09; & k > k_p \\ 0.07 & k \le k_p \end{cases}$$

The difference from PM spectrum is multiplication by a peak enhancement factor and parameterization of the spectral level by the evolving characteristic frequency.

A modification to JONSWAP parameterization to account for Toba spectral form was given by Donelan et al. (1985):

$$S_D(k)k_p^3 = \frac{\beta}{2}\left(\frac{k}{k_p}\right)^{-2.5} \exp\left[-\left(\frac{k}{k_p}\right)^{-2}\right] \cdot \gamma_D^{\exp\left[-\frac{-1}{2\sigma^2}\left(\sqrt{\frac{k}{k_p}}-1\right)^2\right]} \tag{2.1.21}$$

$$\beta = 0.0165\nu^{0.55}$$

$$\gamma_D = \begin{cases} 6.489 + 6\log_{10}\nu \; ; & \nu \ge 0.159 \\ 1.7 \qquad\qquad\quad ; & \nu < 0.159 \end{cases}$$

$$\sigma = 0.08 + 1.29\times 10^{-3}\nu^{-3}$$

This parameterization is based on wider range of characteristic frequencies and smaller experimental scatter. The parameters are chosen such that the spectrum broadens with wave age and approaches PM spectral form at the limit of full development. The choice of Toba form $k^{-2.5}$ allowed lower values of spectral level coefficient than those that were forced to conform to Phillips (1958) form k^{-3}.

The above parameterizations are compared on Figure 2.2. The nondimensional plot shows that younger waves are steeper with more pronounced narrow spectral peak. JONSWAP spectrum at full development follows exactly PM curve, except near the peak. This results in higher overall energy of JONSWAP form at PM limit. Donelan's spectrum has same higher energy but due to the broadening resembles better PM form. The different slopes of Toba and Phillips tail forms are evident in the high frequency

range. The dimensional plot highlights the frequency downshift and energy growth of the evolving spectra. The corresponding values of wave age and characteristic frequency are indicated on the plot. The conversion between the two is done with

$$\nu = \left(2\pi \sqrt{C_D} \frac{c_p}{u_*} \right)^{-1}. \tag{2.1.22}$$

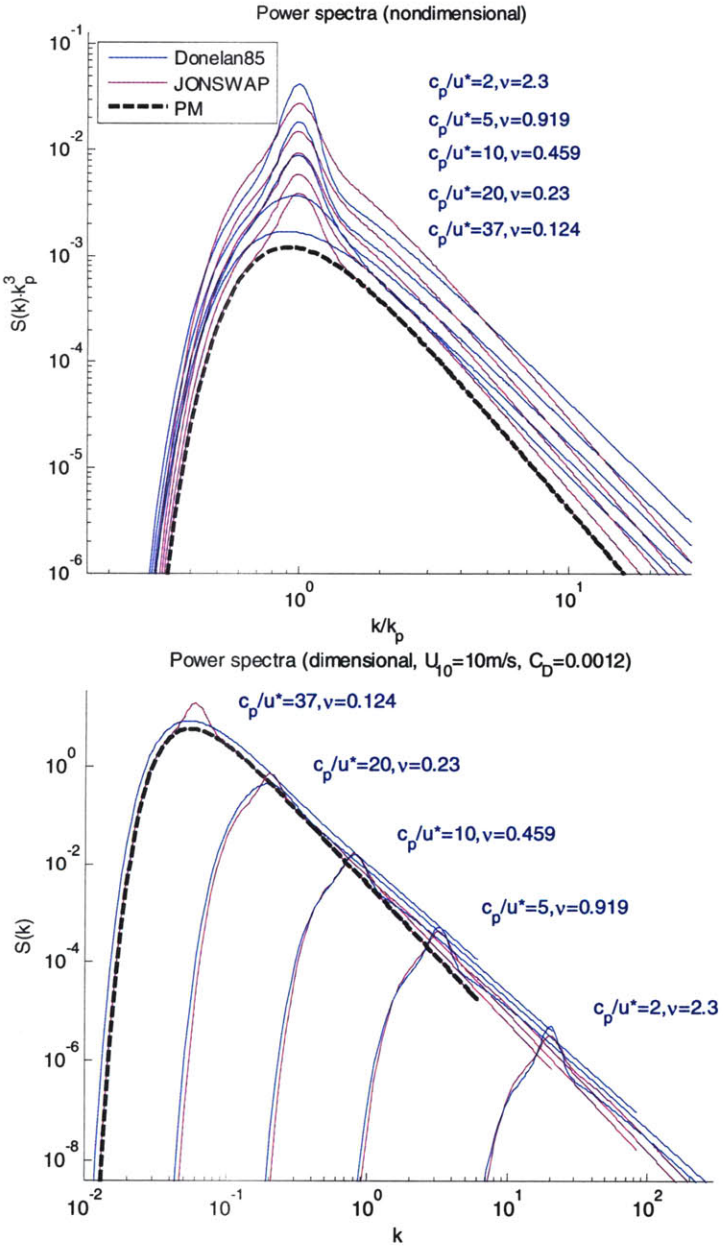

Figure 2.2 Nondimensional and dimensional plots of Pierson-Moskowitz, JONSWAP and Donelan et al. (1985) spectra. The values of drag coefficient and wind velocity are indicated in the bottom plot title.

2.1.5. Emergence of Similarity and Toba 3/2 law

Application of similarity theory by Kitaigorodskii (1962) revealed self-similar structure (details in previous section) of measured power spectra. When scaled by gravity and wind friction velocity, spectra of mature sea states collapse on a universal curve, whereas for developing seas the spectra are self-similar functions of an evolving representative parameter such as the spectral peak frequency. A simplified two parameter description of sea state can be obtained by integrating the power spectrum. The resulting estimate of total energy must remain a function of the characteristic frequency and cannot obtain arbitrary values. Thus, windsea energy and characteristic period are not independent, but are constrained together under wind forcing as expressed by the scaling with wind friction velocity. Toba (1972, 2003) interprets this local balance of wave field with wind as a "local equilibrium" of windsea, which is achieved by strongly nonlinear wind wave interaction processes. A special self-adjustment mechanism emerging from nonlinear "microphysical" (Toba 1998) dynamics appears to establish macroscopic similarity laws. This self-adjustment mechanism is clearly associated with continuities of surface velocity, turbulence structure and momentum transfer between the turbulent boundary layers above and below the wind-wave surface, but the details of it are not presently understood. In particular, no theoretical explanation of the observed scaling of windsea properties with wind friction velocity appears to exist (Toba 1998).

The integral similarity law for windsea energy and characteristic frequency was originally derived by Toba (1972) in terms of significant wave height and significant wave period (Sverdrup and Munk 1947) by eliminating fetch dependence in the empirical growth parameterizations. The primary advantage of the direct relation between windsea characteristics is its applicability to real ocean conditions, where inhomogeneities of wind field and complex fetch geometry rarely satisfy the idealized fetch limited conditions. Toba (1972) expressed this similarity relation in terms of significant wave height and period scaled by wind friction velocity

$$H_* = BT_*^{3/2} \tag{2.1.23}$$

where

$$H_* \equiv gH_s / u_*^2, \quad T_* \equiv gT_s / u_*, \quad B = 0.062 \tag{2.1.24}$$

B is an empirical constant showing perturbations of about $\pm 20\%$ due to wind fluctuation. This empirical similarity relation is known as *3/2-power law*. Toba found that this relation is a universal constraint in wide range of sea states when swells are weak.

Since the significant wave period is approximately the period of the spectral peak, which is related to wave age by the linear dispersion relation

$$\frac{gT_p}{2\pi u_*} = \frac{c_p}{u_*} \tag{2.1.25}$$

Toba's 3/2 law is conveniently expressed in terms of wave age

$$\frac{gH_s}{u_*^2} = 0.98\left(\frac{c_p}{u_*}\right)^{3/2}. \tag{2.1.26}$$

The characteristic wave steepness evolves as

$$\frac{H_s}{\lambda_p} = 0.156\left(\frac{c_p}{u_*}\right)^{-1/2} \tag{2.1.27}$$

Or equivalently, in terms of root mean square amplitude $a_{rms} = \sqrt{2}\sigma = H_s / 2\sqrt{2}$

$$a_{rms}k_p = 0.35\left(\frac{c_p}{u_*}\right)^{-1/2} \tag{2.1.28}$$

Younger wind waves are steeper than the mature ones.

The stochastic form of 3/2 law was proposed by Toba (1978) in terms of the total energy and spectral peak frequency as

$$E_* = 0.051\omega_*^{-3}. \tag{2.1.29}$$

This law is supported by many measurements, in particular by JONSWAP experiment (Hasselmann et al. 1973) as can be seen from (2.1.9). Toba (1978) combined these with $C_D = 1/1000$ to give

$$E_* = 0.053\omega_*^{-3.03} \tag{2.1.30}$$

The original Toba (1972) form (2.1.23) can be obtained with the typically used $C_D = 1/28^2$ such that $E_* = 0.061\omega_*^{-3.03}$. Alternatively, the expression provided by JONSWAP group itself is (Hasselmann et al. 1976) $\varepsilon = 5.3\times10^{-6}\nu^{-10/3}$. More modern measurements were reported in terms of wave age as (2.1.11) (Donelan et al. 1985) or (Donelan et al. 1992)

$$\varepsilon = 0.0023\left(\frac{U_{10}}{c_p}\right)^{-3.2} \tag{2.1.31}$$

It can be noted that the power law is rather consistent and compatible with (2.1.23), although the proportionality coefficient varies up to factor of two from case to case. Toba (1978) explained that the absolute values of these numerical factors are not expected to be universal and the emphasis has to be given to the "basic forms of the equations", i.e. the power laws. Therefore, this will be our interpretation of Toba similarity law.

The similarity argument of Toba (1972) and his hypothesis of nonlinear self adjustment mechanism and local balance of wind and wind waves apply strictly to pure windsea under steady wind and free of swell. Figure 2.3 displays compilation of experimental data (Kawai et al. 1977) for pure windsea conditions in good agreement with Toba 3/2 law. One point falls right and below Toba law line, which corresponds to lower height then expected for pure windsea of same period. This point was measured in open sea conditions, where background swell contaminated the local windsea data. The deviation from Toba law is explained by bias of the averaged characteristic properties of sea state due to superposition of windsea and swell. To confirm this point, in later experiment Ebuchi et al. (1992) observed many combined swell and windsea conditions, their data is presented in Figure 2.4. A consistent picture emerges: all the points fall to the right and

below of Toba law curve. It is seen that Toba law can be interpreted as an *upper bound* on evolution of realistic sea state, which is always a mix of windsea and swell. As swell adjusts to wind forcing it is expected to grow and approach Toba equilibrium line from below. Then, under steady wind, wave system is expected to continue growing along Toba power law line in quasi-equilibrium with wind forcing. This balanced growth corresponds to idealized duration and fetch limited evolution.

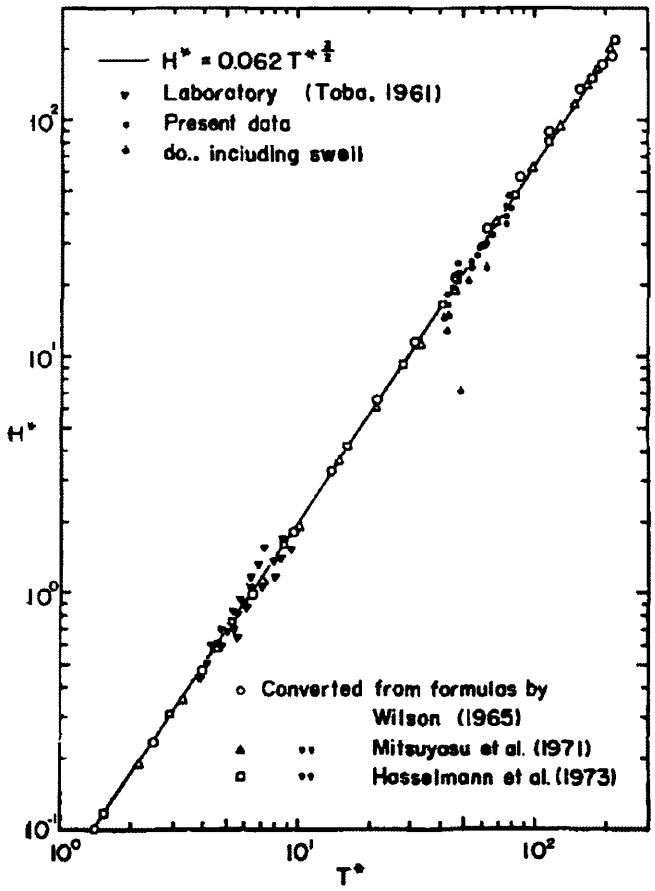

Figure 2.3 3/2 power law and composite data set of Kawai et al. (1977). (Cited from Toba 1997.)

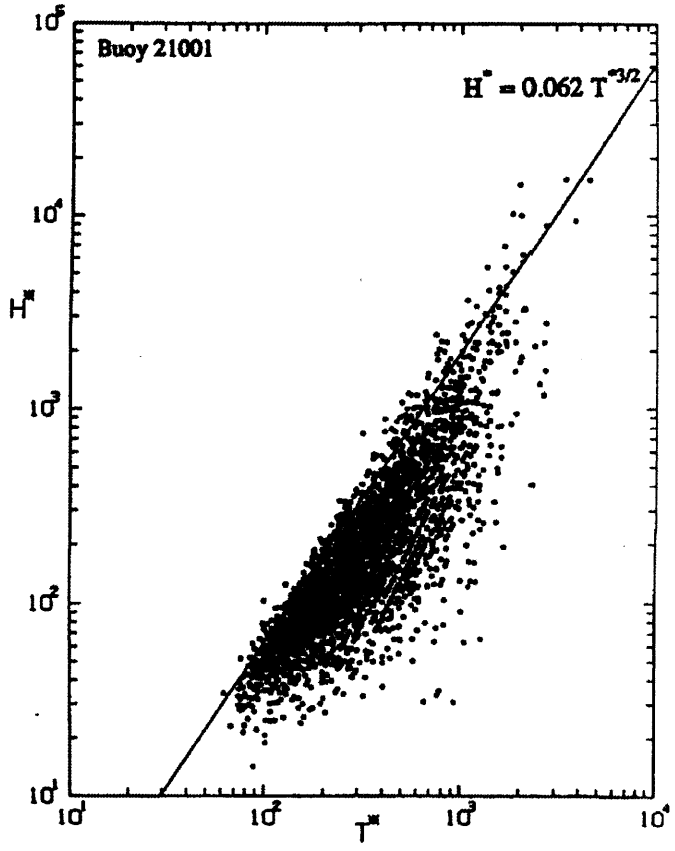

Figure 2.4 3/2 power law and mixed windsea and swell measurements of Ebuchi et al. (1992).

2.2. *Mechanism of wind forcing on waves*

2.2.1. Physics of wind wave interaction

Physics of wind wave interaction is very complex and the modern literature on the subject is very rich. Following a famous critical review (Ursell 1956), which invalidated earlier explanations by Kelvin-Helmholtz instability (Helmholtz 1868, Thomson 1871) and Jeffreys (1925, 1926) sheltering "theory", two complementary theories appeared in 1957: a resonance theory of Phillips and shear instability theory of Miles. Phillips mechanism explains wave generation by a resonance of water surface with preexisting turbulent pressure fluctuations advected by air motion. The generated wavelets propagate with the velocity of wind and growth is linear in time. Miles applied concepts of linear instability theory of inviscid shear flows (Lin 1955) to logarithmic atmospheric profile and showed that air flow may become unstable to perturbations induced by infinitesimal water wave at its lower boundary. These perturbations are coherent motions correlated with the wave and they generate pressure on the wave surface that is in phase with its slopes. Since this pressure is induced by the wave and is, due to linearity of the theory, proportional to its amplitude – wave growth is self amplified and exponential in time. A crucial aspect of Miles mechanism is the existence of a matched "critical layer" where the mean air flow velocity is equal to the phase velocity of the surface wave. The physics of Miles mechanism was further clarified by Stewart and Lighthill. Stewart (1961) clarified the energetics of momentum transfer from wind to waves by Miles' "highly organized motions" and explained the constraint this transport imposes on the wind flow. Lighthill (1962) provided the physical interpretation of Miles mathematical model and explained the mechanism of energy extraction from the mean air flow in terms of negative work of mean vortex force on air oscillating in vicinity of the resonant critical layer.

The two 1957 theories were soon combined (Miles 1959a,b, 1960; Brooke Benjamin 1959). The unified theory explained that initially small wavelets are excited on water surface by the resonant Phillips' mechanism, growth being linear and slow. Then, the powerful mechanism of Miles kicks in and exponentially accelerates wave growth by

positive feedback due to wave induced pressure forcing. This later stage of continuous growth is responsible for transfer of most of the energy to the waves and is, therefore, of the primary interest for applications.

Although these mechanisms established the conceptual framework for understanding wind wave generation, experimental data did not support them quantitatively. Phillips mechanism was disproved because the measured turbulent fluctuations were found much weaker than what his theory assumed. Miles theory was supported experimentally only to order of magnitude. Nonetheless, the linear instability mechanism was proved to be valid. Extended to account for effects of viscosity and capillarity (Valenzuela 1976, Kawai 1979, Van Gastel et al. 1985), shear instability mechanism was shown to explain the exponential growth of short regular waves generated on initially calm water surface and was confirmed experimentally. The mechanism of continuous growth, however, is still a subject of open scientific debate.

Various linear and nonlinear extensions to Miles theory were suggested (see review in Janssen 2004), but none have been established as sufficient explanation of the scattered experimental data. It was suggested (Toba 1978) that the measured growth of energy containing waves is dependent strongly on the nonlinearity of wave hydrodynamics. In experimental study Plant and Wright (1977) have shown that the measured growth is often dominated by nonlinear wave-wave interactions and is different from the initial growth due to direct wind input. Toba (1972, 1978) compiled experimental data from different sources and have shown that energy containing waves in state of active growth under wind forcing satisfy universal similarity law. Toba proposed to explain this macroscopic similarity by hypothesis of local balance of growing waves with the wind, which must be governed by a nonlinear mechanism. Toba's analysis predicts that the characteristic height and period of growing waves should satisfy a simple power law relation, which means that as waves grow in height they also grow in wave length. This is principally different from growth governed by linear instability, where waves grow only in height, the wave length remains constant. Experiments confirm this difference between linear and nonlinear stages of growth, which correspond to initial generation and

continuous growth processes. Figure 2.5 displays laboratory data showing gradual transition from initial growth, when wave length remains constant as wave height increases, to balanced continuous growth of both wave height and wave length. In this thesis we show numerical simulations that reproduce this transition from direct wind-induced growth, governed by linear find forcing mechanism, to balanced growth due to quasi-equilibrium of wind input, nonlinear wave-wave interactions and wave breaking dissipation.

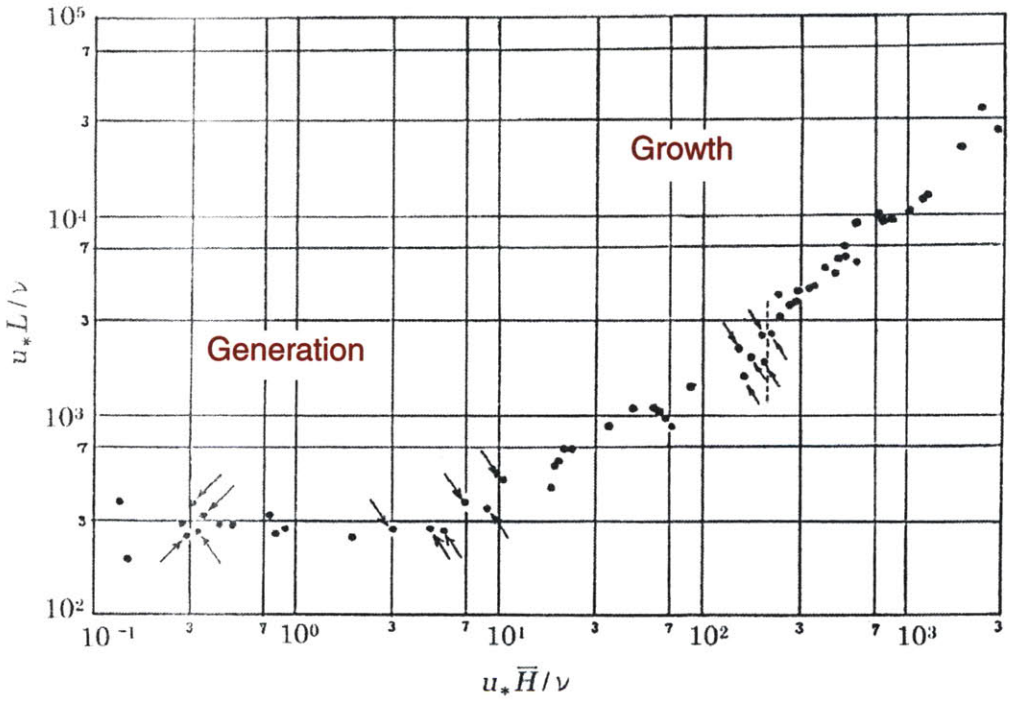

Figure 2.5 Nondimensional characteristic wave height vs. wave length scaled by viscosity and wind friction velocity. Kunishi (1963) wave tank data, reproduced from Toba (1998).

2.2.2. Primary wind forcing mechanism: form drag

In consequence of the complexity of the actual find forcing mechanism and its incomplete understanding, in this thesis we follow a simplified heuristic approach to model the principal energetics of the continuous growth phase. A concise and authoritative overview of the primary effect of wind forcing is given by Donelan (1999, see also Young 1999).

Quoting Donelan (1999) - "Inasmuch as surface water waves are nearly irrotational, the energy flux from wind to waves is brought about mainly by surface pressure fluctuations in phase with the wave slope". Stewart (1961) intuitively explained that water surface is believed to be aerodynamically "rough" with respect to the air motion above it, so that the mechanism of momentum transfer is *form drag* due to correlation between local pressures and roughness elements. Since in homogeneous fluid pressure forces can produce only irrotational motion and by principle of action and reaction – irrotational wave motion can only support normal stresses on the interface, the only mechanism of momentum transfer can be form drag.

Mechanisms by which tangential stresses could contribute to momentum transfer were suggested by Stewart (1967) and Longuet-Higgins (1969a) based on the idea of differential thickening of the shear boundary layer on the water side. However, these effects are considered to be one-to-two orders of magnitude smaller (Donelan 1999). Recently, the interest in the effects of tangential stresses was revived (Peirson and Garcia 2008) in context of nonlinear waves of finite height, but these new findings are beyond the scope of this thesis.

Form drag enters the equations of wave motion through the dynamic boundary condition

$$\varphi_t + g\eta + \tfrac{1}{2}\nabla\varphi\cdot\nabla\varphi = -\frac{P_{wind}}{\rho_w}\Big|_{z=\eta} \qquad (2.2.1)$$

The momentum transferred to the wave is given by integration of the horizontal components of the forces exerted by the normal stress

$$\tau_D = \int_S P_{wind} \hat{n}_h ds \,. \tag{2.2.2}$$

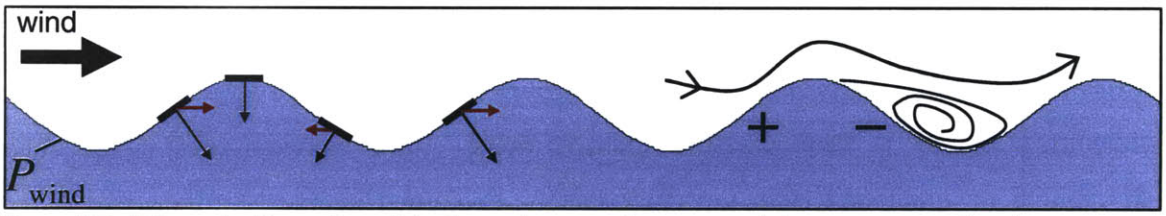

Figure 2.6 Schematic illustration of the forces by normal stresses and the asymmetry of surface pressure distribution.

In two dimensions the mean momentum flux is expressed by

$$\tau_D = \overline{P\eta_x} \tag{2.2.3}$$

Energy flux is the work done by the pressure on moving particles on the surface. Application of the nonlinear kinematic boundary condition

$$w = \eta_t + u\eta_x \tag{2.2.4}$$

allows to express the mean energy flux in the simple form

$$\dot{E}_D = -\overline{Pw} + \overline{P\eta_x u} = -\overline{P\eta_t} \tag{2.2.5}$$

Here the quadratic quantities are averaged over the whole horizontal domain

$$\overline{[\ ]} \equiv \frac{1}{A}\int_A [\ ]\, dA \tag{2.2.6}$$

The geometry of the forcing is detailed in Figure 2.7, where S is the actual surface area and A is its projection on the horizontal plane.

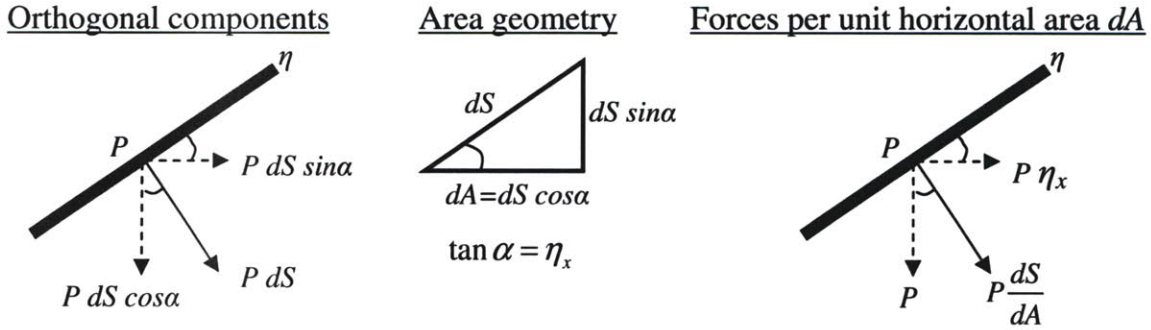

Figure 2.7 Geometry of the forces exerted by normal stress on inclined surface. Surface pressure P, surface elevation η, the angle of surface incline α, the area of the surface segment dS, the projected surface area dA.

Since mean momentum flux is a correlation of pressure with surface slope (2.2.3) only slope coherent pressure component contributes to momentum transfer. Slope coherent pressure is surface pressure distribution in phase with the slope. It is asymmetric with respect to the elevation profile, higher pressure on wind side and lower on lee side. The decomposition of surface pressure distribution to slope coherent component and component in quadrature with the slope can be explained in linear framework. When superposition principle applies, the signals of pressure and elevation can be decomposed to separate sinusoidal modes. Modes with different wavenumbers are uncorrelated (formally on an infinite or periodic domain) and the quadratic forms reduce to sums of products of signals of same wavenumber. In the reduced monochromatic framework only pressure components in phase with the slope contribute to momentum transfer. In other words, only pressure in quadrature with the elevation constitutes form drag. If the wave propagates without change of its form or if phase velocity can be defined for each mode, then

$$\left.\frac{d}{dt}\right|_c = \frac{\partial}{\partial t} + c\frac{\partial}{\partial x} = 0 \tag{2.2.7}$$

holds and energy flux due to form drag can be expressed by

$$\dot{E}_D = -\overline{P\eta_t} = \overline{P\eta_x}c. \tag{2.2.8}$$

This expression stresses again the importance of pressure-slope correlation and is consistent with the relation between leading order estimates of wave momentum M and energy E for single sinusoidal wave (Stewart 1961, Longuet-Higgins 1969b)

$$E = Mc \tag{2.2.9}$$

If a slope-coherent pressure component is expressed by

$$p = \alpha_* \eta_x \tag{2.2.10}$$

then energy flux from wind into the associated linear wave is $\dot{E}_D = \alpha_* \overline{\eta_x^2} c$. For linear energy given by $E = \rho_w g \overline{\eta^2}$, the fractional energy transfer rate is

$$\frac{1}{E}\frac{\partial E}{\partial t} = \frac{\alpha_*}{\rho_w \sqrt{g}} k^{3/2} \tag{2.2.11}$$

or in a nondimensional form

$$\frac{1}{\omega E}\frac{\partial E}{\partial t}=\frac{\alpha_*}{\rho_w}\frac{k}{g}. \tag{2.2.12}$$

Here, the dispersion relation for linear free wave $c=\sqrt{g/k}$ was assumed. If the coefficient α_* is independent of time and the linear wave absorbs all the supplied energy, then the growth is exponential and independent of time. Note, that shorter waves grow faster in both dimensional and nondimensional forms.

In the above heuristic derivation growth of linear monochromatic wave was calculated based on assumptions formally valid only for free linear waves. The consistency of this derivation for forced nonlinear waves is not obvious a priori and has to be verified for linear and nonlinear forced waves. In the Appendix the heuristic derivation above is verified analytically for linear forced waves, the errors are shown to be small. In a nonlinear broadband framework the validity of the above assumptions and approximations needs to be substantiated either analytically or with a numerical model. In particular, the applicability of superposition principle, the dispersion relation and phase velocity concepts require further discussion.

2.2.3. Wind forcing parameterization

Wind force on waves is assumed to be scaled by the turbulent shear stress in the air boundary layer flow $\tau = \rho_a u_*^2$. The normalized pressure on water surface is defined by

$$p_w \equiv \frac{P_{wind}}{\rho_a u_*^2} \tag{2.2.13}$$

This choice of forcing scale is consistent with scaling wind-wave parameters by friction velocity (Janssen et al. 1987). If empirically based parameterization approach of Banner and Song (2002) is adopted and only slope coherent surface pressure distribution is considered, it is given by

$$p_w(x,t) = \alpha \eta_x(x,t) \tag{2.2.14}$$

Here α is an empirical nondimensional constant to be specified from observations. Further, following Banner and Song, we can define *surface pressure forcing level* as

$$\alpha_* \equiv \alpha \rho_a u_*^2, \quad P_{wind} = \alpha_* \eta_x \tag{2.2.15}$$

The coefficient α_* has units of pressure or shear stress and is assumed a function of different wave age conditions. In the above form the parameterization of wave induced pressure is similar to the sheltering theory of Jeffreys (1925, 1926)

$$P_s = S \rho_a (U - c)^2 \eta_x . \tag{2.2.16}$$

Where S is the empirical "sheltering coefficient", $(U\text{-}c)$ is relative wind speed, i.e. minus phase velocity. If friction velocity in our formulation is replaced by the relative wind speed, then coefficient α may be regarded as a modified sheltering coefficient.

Miles (1957) linear theory expresses the slope coherent wave induced wind pressure by

$$P_s = \beta \rho_a \left(\frac{u_*}{\kappa} \right)^2 \eta_x , \tag{2.2.17}$$

Here $\kappa \sim 0.4$ is von Karman constant and the nondimensional Miles' growth coefficient β is evaluated numerically for different wavenumbers by solution of a shear instability

problem in the air (Conte and Miles 1959). Our empirical coefficient is related to Miles' by

$$\alpha = \frac{\beta}{\kappa^2}. \tag{2.2.18}$$

Empirically, the value of α can be estimated either by direct measurements of the wave induced surface pressure or from the observed growth rates (Plant 1982). Following Banner and Song (2002) we implement the latter approach and estimate the magnitude of pressure forcing by relating the expression for the effective wind input growth rate to the growth rates observed for ocean wind waves.

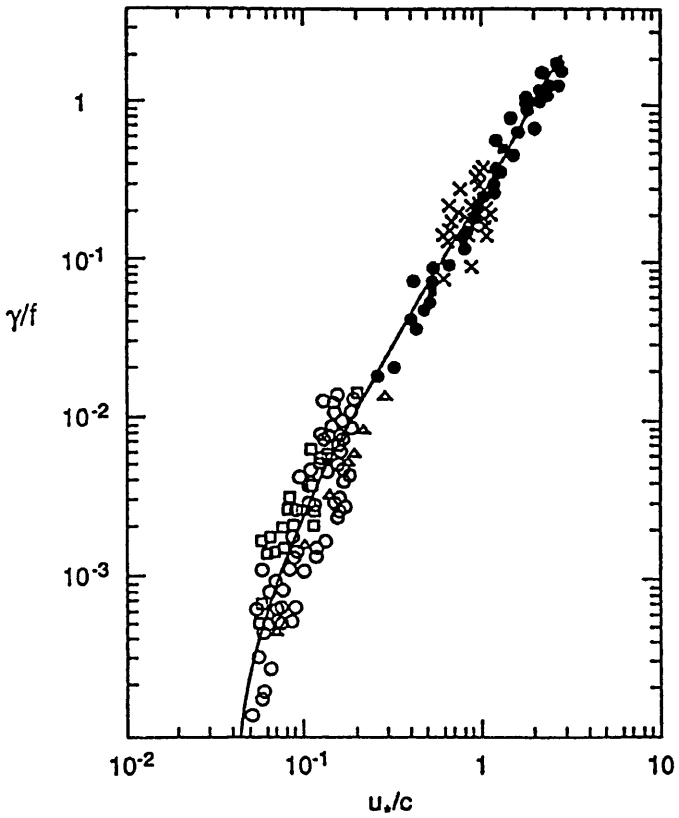

Figure 2.8 Observed nondimensional wind wave growth rates against the inverse wave age. Open circles and squares are field data, other symbols represent laboratory data. Solid line is the numerical solution based on Miles theory. Note, the vertical axis is scaled by factor 2π compared to (2.2.19). Cited from Komen et al. (1994).

As discussed in the previous section, in linearized framework of slowly growing free waves forced by (2.2.14) the nondimensional spectral wind growth rate is given by

$$\frac{\dot{E}}{\omega E} = \alpha \frac{\rho_a}{\rho_w} \left(\frac{u_*}{c} \right)^2 \tag{2.2.19}$$

Values experimentally observed in the oceans are presented in Figure 2.8 for wave ages $5 < c/u_* < 20$. Taking

$$\rho_a / \rho_w = 0.001225 \tag{2.2.20}$$

Banner and Song deduce that $\alpha \sim 32.5$ for $c/u_* \sim 5$. The above data was originally compiled by Plant (1982), who obtained the empirical estimate

$$\frac{\dot{E}}{E} = (0.04 \pm 0.02) \left(\frac{u_*}{c} \right)^2 \omega \tag{2.2.21}$$

for waves propagation along wind direction. With (2.2.20) it is equivalent to

$$\frac{\dot{E}}{\omega E} \frac{\rho_w}{\rho_a} = (32.7 \pm 16) \left(\frac{u_*}{c} \right)^2 \tag{2.2.22}$$

For typical Miles theory value for younger ocean waves β=3.3, or equivalently α=21. This is on the lower side of Plant's estimate but is well within the scatter bounds. The predictions of Miles theory for the full range of wave age is graphically compared to the observations on Figure 2.9 and Figure 2.10. Miles growth rates are given as calculated for 4 different values of Miles' wind-profile parameter, or equivalently Charnock constants (Komen et al. 1994). The values on Figure 2.9 are obtained directly from Figure 2.8, while on Figure 2.10 they are converted using (2.2.19). It can be seen that although the best fit is provided by Janssen's evaluation of Miles theory (Komen et al. 1994), the simplified estimate based on constant forcing level (α=32.5) fits the experimental data reasonably well within the measured scatter. The original calculations of Conte and Miles (1959) show weaker growth rates but are also acceptable within the scatter. This large scatter, that is somewhat inhibited by the logarithmic scale of presentation, is better seen on the transformed data plot on Figure 2.10. The scatter spans one order of magnitude and is one of the known reasons for the critique on the insufficient quality of data and the poor level of understanding of wind waves (Donelan et al. 2006).

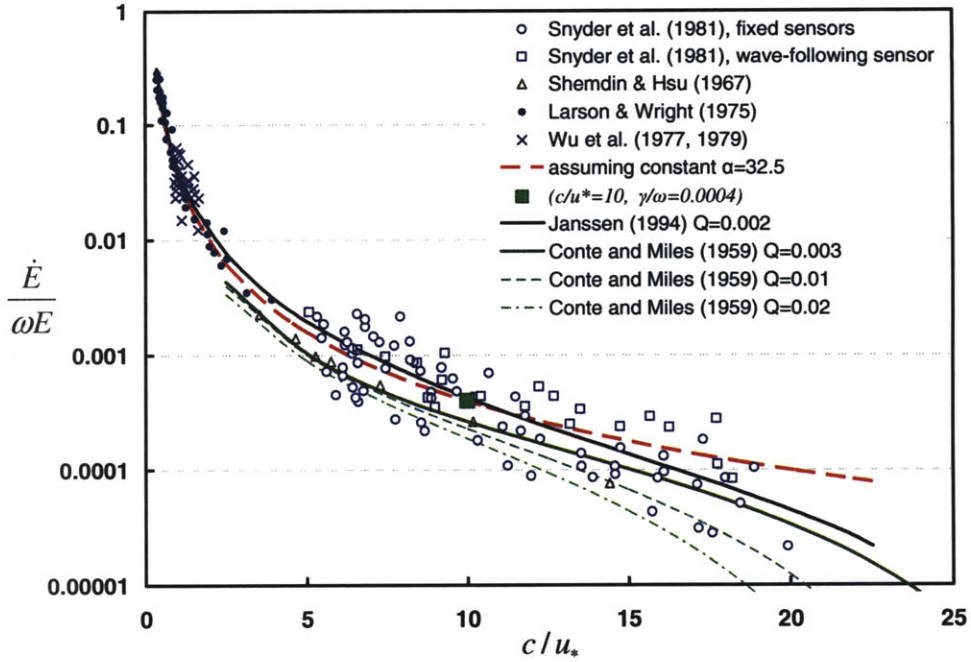

Figure 2.9 Nondimensional growth rates against wave age. Plant (1982) data compared to Miles theory predictions and constant α estimate.

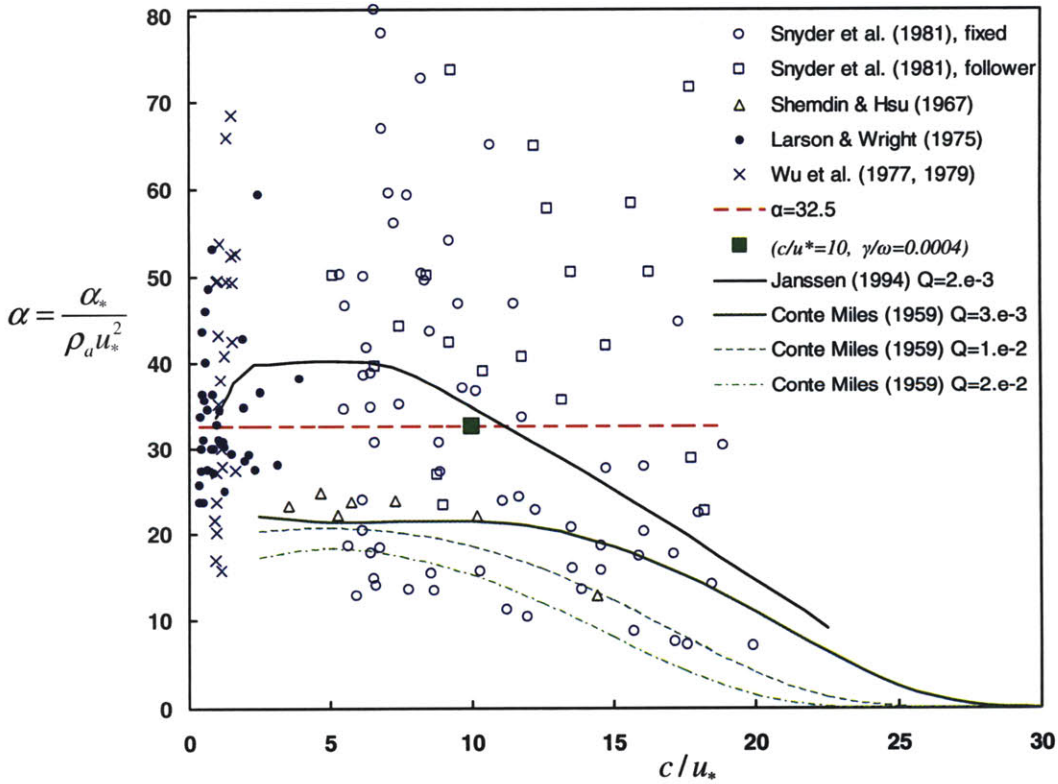

Figure 2.10 Forcing coefficient α against wave age. Plant (1982) data compared to Miles theory predictions and constant α line.

In this thesis the forcing of the wind is estimated empirically from the above data. The pressure is specified in terms of the surface pressure forcing level α_*. The nondimensional form is obtained by use of the expression for the growth rate of single linear wave

$$\frac{\dot{E}}{\omega E} = \frac{\alpha_* k}{\rho_w g} \tag{2.2.23}$$

The effective growth rate is read from Figure 2.11, which shows same data as Figure 2.9, only with linear vertical axis scale, given here for convenience of graphical reference. As leading order approximation α_* can be assumed constant for all wave ages in range relevant for growing energy containing ocean waves, $5 < c/u_* < 20$. The corresponding growth rates are different for different wave ages, but all can be represented by $\alpha = 32.5$. For example, for wave age $c/u_* = 10$ the nondimensional growth rate and forcing level are $\alpha_* k/\rho_w g = 0.0004$.

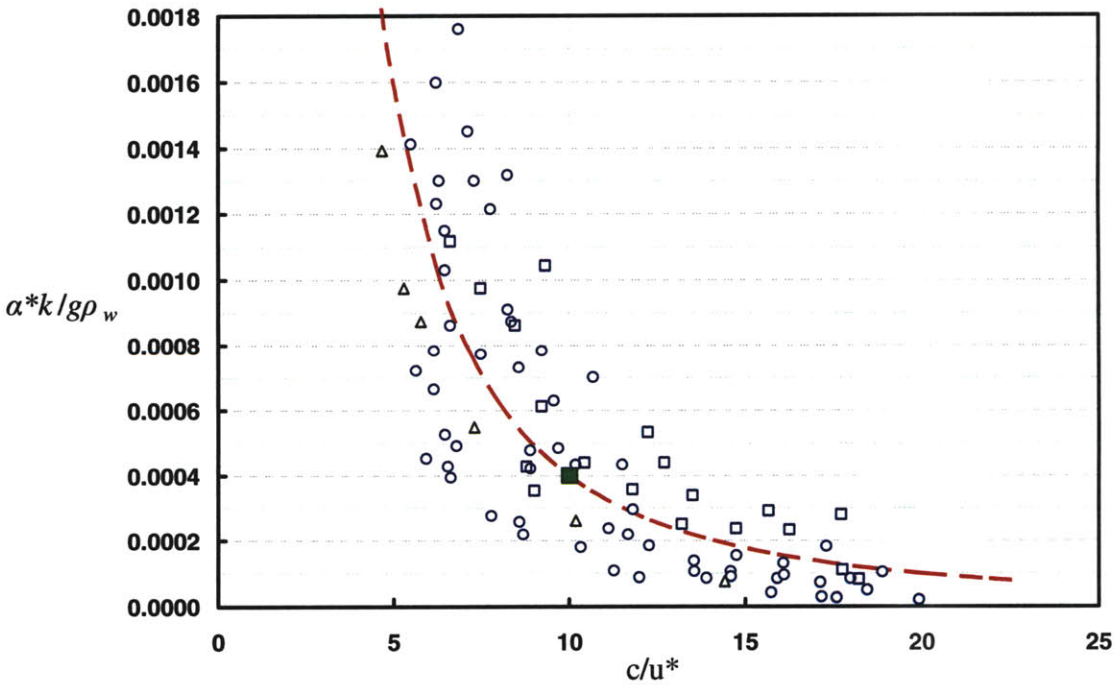

Figure 2.11 Nondimensional forcing level against wave age. Plant (1982) data compared to constant α=32.5 estimate.

Chapter 3. Direct simulation model

3.1. *Theory and mathematical formulation*

3.1.1. Overview

The nonlinear wavefield is simulated with a numerical model based on the Higher Order Spectral method, hereafter HOS. The method is based on the mode coupling idea (Dommermuth and Yue 1987) generalized to resolve the nonlinear interactions to an arbitrary high order M in wave steepness. The treatment of the nonlinear boundary conditions of water surface is pseudo-spectral – spatial derivatives are evaluated in spectral (wavenumber) domain while nonlinear products are calculated in physical space at a discrete set of points. Large number ($N=O(1000)$) of modes is transformed between physical and wavenumber domains with FFT routine, which grants the model its superior computational properties. Namely, for space periodic boundary conditions the number of operations required at every time step is reduced to $O(MN\log N)$ from typical $O(N^3)$ required by alternative methods. The algorithmic structure of the method makes it highly scalable, the nonlinear order is straightforwardly extended and serial computational time can be significantly reduced by multi-processor parallelization.

Superiority of the HOS method is not limited to computational advantages. It has been proved analytically (Onorato et al. 2007) that, at least to the third order, the method exactly coincides with a discretized solution of the integro-differential Zakharov equation (Zakharov 1968). This fact strategically links the HOS method to the Hamiltonian description of surface waves and imposes its conservative properties and fundamental symmetries (Krasitskii 1994). In view of this equivalence, HOS method can be regarded and utilized not only as an efficient numerical solver and practical simulation tool, but also as a fundamental computational method for theoretical study of surface wave problem.

The HOS method relies critically on validity of Taylor series expansion of velocity potential about the mean waterline. For moderately steep regular waves the validity of the method was established by Dommermuth and Yue (1987) by demonstration of exponential convergence with respect to N and M. For broadband irregular wavefields the question of method's validity is a nontrivial one and is the subject of current active research, as discussed at the end of this chapter.

3.1.2. Nonlinearity

The major advantage of HOS scheme over alternatives like mode-coupling and Zakharov equations is the convenience of extension to arbitrary orders of nonlinearity (Dommermuth and Yue 1987). Although full nonlinearity of surface waves has been investigated by various methods (e.g. Schwartz 1974, Longuet-Higgins and Cokelet 1976), their theoretical limitations and prohibitive computational requirements have prevented applications to the problem of real ocean waves. Practical progress was achieved with only lowest orders of nonlinearity considered. The nonlinear interactions underlying the nonlinear transfer in Hasselmann's kinetic equation, that are taken into account in third generation wave forecasting models, are four-wave resonant interactions (Komen et al. 1994, Dyachenko and Lvov 1995). In phase resolving framework these quartet interactions are described by terms of cubic order in steepness (Benney and Newell 1967). The nonlinear evolution of spectral modes that is governed by these interactions is effective on time scale $O(T\varepsilon^{-2})$. The statistical properties evolve on time scale $O(T\varepsilon^{-4})$ if random phase is assumed (Janssen 2003). Modulational instability in 2D domain is well described by quartet interactions (Phillips 1967). Next order nonlinearity leads to quintet interactions that effect evolution on longer time scales and are important mainly for 3D instability (Stiassnie and Shemer 1984) and formation of directional spectrum (Kalmykov 1998). Since in this study we limit the discussion to 2D configuration, it is consistent to consider only leading order nonlinearity. Consequently, in simulations shown below the discussion is limited to third nonlinear order. Note, that the analytically proved equivalence of third order HOS scheme to the cubic Zakharov

equation (Onorato et al. 2007) implies additional level of theoretical validity for such simulations in the sense of their comparison to Hamiltonian framework based studies of nonlinear wind waves (Kalmykov 1996).

3.1.3. Assumptions

Consider material surface separating an infinitely deep, homogeneous, incompressible and inviscid water body from air above it. We assume that this surface is single-valued, i.e. its height can always be described by a single valued function $z=\eta(x,t)$. By this assumption we exclude occasional multilayer configurations, like overturning waves and plunging breakers. Further, we assume water motion to be irrotational, since in absence of initial vorticity no force in inviscid Navier-Stokes equations can generate vorticity in simply connected domain. We do not consider the effects of surface tension by focusing the discussion on larger spatial scales, i.e. we neglect effects of capillarity on energy containing waves. In this work we consider only the case of long crested waves propagating in one direction limiting the derivation to one horizontal dimension or 2D, in other words. The horizontal coordinate perpendicular to the crests is x, the vertical coordinate z is positive upward and its origin is set at the undisturbed water level. In order to apply the regular FFT algorithms a regular equally spaced grid is assumed in the spectral domain, which implies spatial periodicity in the horizontal direction. It must be noted that three major simplifying assumptions made here – infinite depth, neglect of surface tension and two-dimensionality, are not limitations of the HOS method (e.g. Wu et al. 2006) and are imposed in this study with the aim of focusing on the wind-wave interaction problem and keep the physical configuration similar to that on which Miles theory is based (e.g. Miles 1957).

3.1.4. HOS equations

The irrotational and incompressible water motion satisfies the Laplace equation for velocity potential $\varphi(x,z,t)$

$$\Delta\varphi=0 \qquad |_{z\le\eta} \tag{3.1.1}$$

and is termed - potential flow. The nonlinear kinematic and dynamic boundary conditions on a single-valued free surface are expressed by

$$\varphi_z = \eta_t + \varphi_x \eta_x \qquad |_{z=\eta} \tag{3.1.2}$$

$$\varphi_t + g\eta + \tfrac{1}{2}\nabla\varphi \cdot \nabla\varphi = -\frac{P_a}{\rho_w} \qquad |_{z=\eta} \tag{3.1.3}$$

Zero vertical motion is postulated at the lower boundary

$$\varphi_z = 0 \qquad |_{z=-\infty} \tag{3.1.4}$$

HOS equations are defined in terms of the two canonical conjugate variables from Zakharov Hamiltonian theory (1968): surface elevation $\eta(x,t)$ and surface velocity potential

$$\psi(x,t) \equiv \varphi(x,\eta(x,t),t) \tag{3.1.5}$$

Using partial differentiation chain rule we introduce the relations

$$\frac{\partial\psi}{\partial t} = \frac{\partial\varphi}{\partial t} + \frac{\partial\varphi}{\partial z}\frac{\partial\eta}{\partial t} \tag{3.1.6}$$

$$\frac{\partial\psi}{\partial x} = \frac{\partial\varphi}{\partial x} + \frac{\partial\varphi}{\partial z}\frac{\partial\eta}{\partial x}. \tag{3.1.7}$$

Substitution of (3.1.6) and (3.1.7) into the kinematic and dynamic boundary conditions (3.1.2) and (3.1.3) transfers them to Zakharov form

$$\eta_t = \varphi_z(1+\eta_x\eta_x) - \eta_x\psi_x \qquad |_{z=\eta} \tag{3.1.8}$$

$$\psi_t = -g\eta - \tfrac{1}{2}\psi_x\psi_x + \tfrac{1}{2}(1+\eta_x\eta_x)\varphi_z\varphi_z - \frac{P_a}{\rho_w} \qquad |_{z=\eta} \tag{3.1.9}$$

For conciseness, subscripts have been used interchangingly with the standard notation to denote partial differentiation.

3.1.5. HOS method

Given that steepness of surface wave is always bounded ($\varepsilon < 1$) and usually is a small number, the 2D velocity potential is expanded in perturbation series with steepness as ordering parameter

$$\varphi(x,z,t)=\sum_{m=1}^{M}\varphi^{(m)}(x,z,t) \tag{3.1.10}$$

$\varphi^{(m)}(x,z,t)$ is assumed to be a quantity of order $O(\varepsilon^m)$, M is the order of approximation of nonlinearity. Note that the surface elevation is not explicitly expanded in orders of steepness in HOS method. The key idea of the method is combination the perturbation expansion with Taylor expansion over reference vertical level:

$$\psi(x,t)=\varphi(x,\eta,t)=\sum_{m=1}^{M}\sum_{k=0}^{M-m}\frac{\eta^k}{k!}\frac{\partial^k}{\partial z^k}\varphi^{(m)}(x,0,t) \tag{3.1.11}$$

The double summation is conveniently presented in matrix form which exhibits a diagonal structure of increasing orders of steepness:

$$\begin{aligned}\varphi(x,\eta,t)=&\varphi^{(1)}(x,0,t)+\eta\frac{\partial}{\partial z}\varphi^{(1)}(x,0,t)+\frac{1}{2}\eta^2\frac{\partial^2}{\partial z^2}\varphi^{(1)}(x,0,t)+\frac{1}{3!}\eta^3\frac{\partial^3}{\partial z^3}\varphi^{(1)}(x,0,t)+\ldots\\&+\varphi^{(2)}(x,0,t)+\eta\frac{\partial}{\partial z}\varphi^{(2)}(x,0,t)+\frac{1}{2}\eta^2\frac{\partial^2}{\partial z^2}\varphi^{(2)}(x,0,t)+\ldots\\&+\varphi^{(3)}(x,0,t)+\eta\frac{\partial}{\partial z}\varphi^{(3)}(x,0,t)+\ldots\\&+\varphi^{(4)}(x,0,t)+\ldots\end{aligned} \tag{3.1.12}$$

For any given distribution of surface potential $\varphi(x,\eta,t)=\psi(x,t)$ the volume potential $\varphi(x,z,t)$ is reconstructed by collection of terms of same order. The values of potentials $\varphi^{(m)}$ are obtained through a sequence of boundary conditions on $z=0$:

$$\begin{aligned}&\varphi^{(1)}(x,0,t)=\psi(x,t)\\&\varphi^{(2)}(x,0,t)=-\eta\frac{\partial}{\partial z}\varphi^{(1)}(x,0,t)\\&\varphi^{(3)}(x,0,t)=-\eta\frac{\partial}{\partial z}\varphi^{(2)}(x,0,t)-\frac{1}{2}\eta^2\frac{\partial^2}{\partial z^2}\varphi^{(1)}(x,0,t)\\&\cdots\\&\varphi^{(m)}(x,0,t)=-\sum_{k=1}^{m-1}\frac{\eta^k}{k!}\frac{\partial^k}{\partial z^k}\varphi^{(m-k)}(x,0,t),\quad m=2,3,\ldots,M\end{aligned} \tag{3.1.13}$$

Thus, the solution is achieved by transforming the original problem for $\varphi(x,z,t)$ on the complex boundary $z=\eta(x,t)$ to a sequence of M problems for $\varphi^{(m)}(x,z,t)$ on the

boundary $z=0$. Each $\varphi^{(m)}(x,z,t)$ is expanded in finite number N of spectral modes, in deep water given by

$$\varphi^{(m)}(x,z,t)=\sum_{n=1}^{N}\hat{\varphi}_n^{(m)}(t)e^{k_n z}e^{ik_n x} \tag{3.1.14}$$

The modal amplitudes $\hat{\varphi}_n^{(m)}(t)$ are determined by (3.1.13) in pseudo-spectral manner for any given $\psi(x,t)$ and $\eta(x,t)$. Note, that direct substitution of spectral expansions in (3.1.13) does not reduce to simple relations between the modal amplitudes (except for the leading order), summations are not commutative. The nonlinear products lead to hierarchy of convolutions of amplitudes if (3.1.13) is expressed explicitly in the spectral domain, which is the source the Zakharov structure in HOS equations as shown to the third order by Onorato et al. (2007).

Eventually, the vertical velocity at the surface is found as function of $\psi(x,t)$ and $\eta(x,t)$ from (3.1.11) in form

$$\varphi_z(x,\eta,t)=\sum_{m=1}^{M}\sum_{k=0}^{M-m}\frac{\eta^k}{k!}\sum_{n=1}^{N}\varphi_n^{(m)}(t)\frac{\partial^{k+1}}{\partial z^{k+1}}e^{k_n z}e^{ik_n x} \tag{3.1.15}$$

The vertical velocity is substituted into the governing equations (3.1.8), (3.1.9) which are integrated in time by a standard finite difference scheme.

3.2. *Numerical method*

Here we describe mainly the extensions of the original method developed by Dommermuth and Yue (1987). The reader is referred to the original for the description of the basic implementation, treatment of truncation, round-off, aliasing and time integration errors, numerical convergence tests and integral accuracy checks. Some of these issues are further discussed below in the context of application to broadband irregular wavefield simulations.

3.2.1. Nonlinear order

Dommermuth and Yue (1987) selected the order of perturbation M to satisfy the desired level of accuracy δ for required steepness ε such that $\delta \approx \varepsilon^M$. Then the minimum number of modes N was chosen to satisfy convergence requirements. By reversing the convergence argument, for fixed number of modes N the order of nonlinearity M should be small enough to achieve convergence. Consequently, we experimented with values M=*3-6* and set M=*3* for final simulations, which is also in accordance with the discussion in the previous section.

3.2.2. Model discretization

We define physical, spectral and time resolution in terms of a characteristic (or principal) monochromatic wave:

$$R_{ph} = \frac{\lambda_p}{\Delta x} \tag{3.2.1}$$

$$R_{sp} = \frac{k_p}{\Delta k} \tag{3.2.2}$$

$$R_{time} = \frac{T_p}{\Delta t} \tag{3.2.3}$$

Where Δx, Δk, Δt are the discrete grid sizes of horizontal coordinate, wavenumber and time. The spatial domain is assumed to be periodic, its length D defines the smallest resolved wavenumber

$$\Delta k \equiv k_0 = \frac{2\pi}{D}. \tag{3.2.4}$$

The spatial domain is resolved by finite number of discrete points, denoted NN, which define the shortest resolved distance

$$\Delta x = \frac{D}{NN}. \tag{3.2.5}$$

The shortest wavelength captured by discrete Fourier analysis is Nyquist wavelength $\lambda_{NQ} = 2\Delta x$, the corresponding wavenumber is $k_{NQ} = \pi / \Delta x = k_0 NN / 2$. The aliasing filter (Dommermuth and Yue 1987), however, removes half of the spectral components. The largest remaining wavenumber is

$$k_N = Nk_0, \quad N \equiv NN/4 \tag{3.2.6}$$

The shortest resolved wavelength is, therefore,

$$\lambda_N = \frac{2\pi}{k_N} = 4\Delta x \tag{3.2.7}$$

We define the wavenumber of the principal wave

$$k_p = n_p k_0 \tag{3.2.8}$$

The principal wavelength is correspondingly

$$\lambda_p = \frac{2\pi}{k_p} = \frac{D}{n_p} \tag{3.2.9}$$

The number n_p defines the number of the principal waves in the domain and corresponds exactly to the definition of spectral resolution. The physical resolution is given by the ratio $R_{ph} = 4N / n_p$. Note, that the total number of points in the physical domain is the product of the resolutions: $NN = R_{ph} R_{sp}$. It is seen that 2 independent nondimensional numbers are required to uniquely define the discretization in physical and wavenumber domains. The configuration of the discretized domains is illustrated in Figure 3.1.

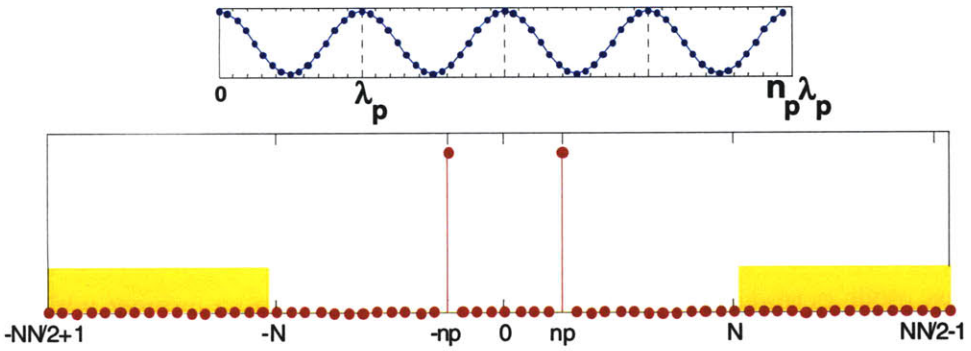

Figure 3.1 Spatial and spectral domains configuration. The aliased area is marked by yellow ribbon. The rightmost tick on the wavenumber axis (NN/2-1) is not the Nyquist wavenumber (NN/2).

3.2.3. Model scaling

The length scale is introduced such that $\Delta k^{\#} = 1$, i.e. the scaled nondimensional wavenumbers are whole numbers $k_n^{\#} = n = 0, \pm 1, \pm 2, ..., \pm N$. The length scale is $\mathbf{L} = 1/k_0$, the scaled domain size is 2π,

$$x = x^{\#}\mathbf{L} = x^{\#}\frac{D}{2\pi}, \qquad k = k^{\#}k_0 = nk_0 \tag{3.2.10}$$

Steepness is conveniently expressed in dimensional and scaled variables

$$ka = nk_0 a = na^{\#} \tag{3.2.11}$$

Time is scaled such that the acceleration due to gravity is 1 in the nondimensional variables:

$$g^{\#} = 1, \quad g = g^{\#}\frac{\mathbf{L}}{\mathbf{T}^2}, \quad \mathbf{T} = \sqrt{\frac{\mathbf{L}}{g}} = \sqrt{\frac{1}{k_0 g}} \tag{3.2.12}$$

The linear angular frequency is given by the linear deep water dispersion relation

$$\omega = \frac{2\pi}{T} = \sqrt{gk} \tag{3.2.13}$$

The linear period of the longest wave is

$$T_0 = \frac{2\pi}{\sqrt{gk_0}}, \qquad T_0^{\#} = 2\pi \tag{3.2.14}$$

In our implementation of the code, it is discretized by integer r timesteps

$$\frac{T_0}{\Delta t} = \frac{T_0^{\#}}{\Delta t^{\#}} = \frac{2\pi}{\Delta t^{\#}} \equiv r \tag{3.2.15}$$

Each timestep, $\Delta t^{\#} = 2\pi / r$ long, is split to 4 substeps by fourth order Runge-Kutta integration scheme. Time resolution is, therefore, expressed by

$$R_{time} = \frac{T_p}{\Delta t} = \frac{2\pi / \sqrt{gk_p}}{\Delta t} = \frac{T_0}{\Delta t} \frac{1}{\sqrt{n_p}} = \frac{r}{\sqrt{n_p}} \tag{3.2.16}$$

The shortest mode period is resolved by $\frac{T_N}{\Delta t} = \frac{T_0}{\Delta t} \frac{1}{\sqrt{N}}$ timesteps, a number which in our simulations is fixed to 32 for smoothness of time integration. Alternative ways to determine time discretization and the related Courant conditions are discussed below.

The Nyquist frequency associated with time resolution is

$$\omega_{NQ} = \frac{\pi}{\Delta t} \tag{3.2.17}$$

It should be used in evaluation of Courant conditions. Dommermuth and Yue (1987) set the linear Courant condition to

$$\Delta t^2 \leq 8 / N \tag{3.2.18}$$

As seen in Figure 3.2 this time resolution is not sufficient to capture the oscillations of the bound harmonics that propagate with the phase velocity of the principal component. Therefore, we propose to define a *nonlinear Courant condition* to resolve the bound harmonics of the principal and adjust the Nyquist frequency accordingly:

$$\omega_{NQ} = c_p k_N = \frac{k_N}{\sqrt{k_p}}, \qquad \frac{T_N}{\Delta t} = 2\sqrt{\frac{N}{n_p}} \tag{3.2.19}$$

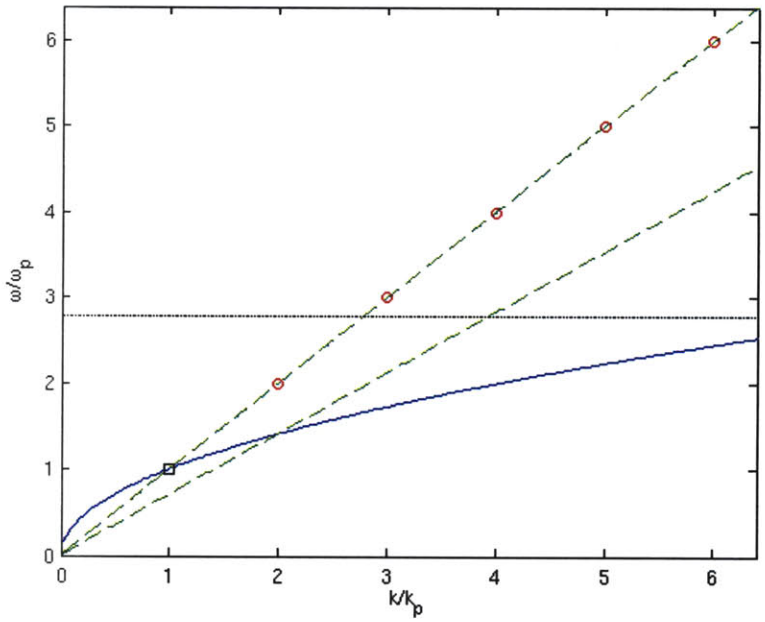

Figure 3.2 Dispersion plane: solid blue line – linear dispersion relation, dashed green – dispersion relations for bound components, grey solid - Dommermuth and Yue (1987) linear Courant condition. Space harmonics of the principal mode marked by red circles.

Pressure is the only variable in the model which depends on the scale of mass. It is scaled such that the density of water is 1 in scaled variables.

$$p = p^{\#}\boldsymbol{P} = p^{\#}\frac{\rho_w g}{k_0} \tag{3.2.20}$$

This specifies the scaling of wind forcing trough the wave induced pressure.

3.2.4. Convergence

Convergence tests with respect nonlinear order (M) and physical resolution (N) are presented in Dommermuth and Yue (1987) for spectral resolution n_p=1. Exact Stokes wave solution (Schwartz 1974) was used as a standard benchmark. In Chapter 4 we report convergence experiments with respect to increasing spectral resolution. Complete set of convergence tests for broadband configurations including random phase effects is under development and is not reported here, since no standard benchmark seems to exit for the general case.

3.2.5. Initial conditions

Initial values of elevation and surface potential can be specified for arbitrary wave field conditions, constrained by model assumptions and discretization. An attention is required to ensure dynamic consistency of the specified elevation and surface potential. In this thesis the initial values of elevation and surface potential are specified in the spectral domain based on linear theory. The nonlinear consistency is achieved by a "warm start" of the simulations - the model is assumed to evolve to a dynamically consistent state after few linear periods of the principal spectral component. For further discussion and an alternative approach the reader is referred to Dommermuth (2000).

Regular periodic waves are specified by superposition of Airy waves, given in model nondimensional form by

$$\eta^{\#} = A_n^{\#} \cos(nx^{\#} + \theta), \qquad \varphi_n^{\#} = \frac{A_n^{\#}}{\sqrt{n}} \sin(nx^{\#} + \theta). \tag{3.2.21}$$

Broadband irregular wave field is initialized by superposition of the linear components with uniformly random phase.

$$\eta = \sum_k A_k \cos(kx - \omega_k t + \phi_k), \qquad \phi_k = U[0, 2\pi] \tag{3.2.22}$$

The amplitude of each mode is obtained by discretization of the observed power spectra (see Section 2.1.4) in wavenumber domain

$$\tfrac{1}{2} A_k^2 = S(k)dk\,. \tag{3.2.23}$$

Example of elevation field reconstructed from Donelan et al. (1985) spectrum is shown below in Figure 3.3.

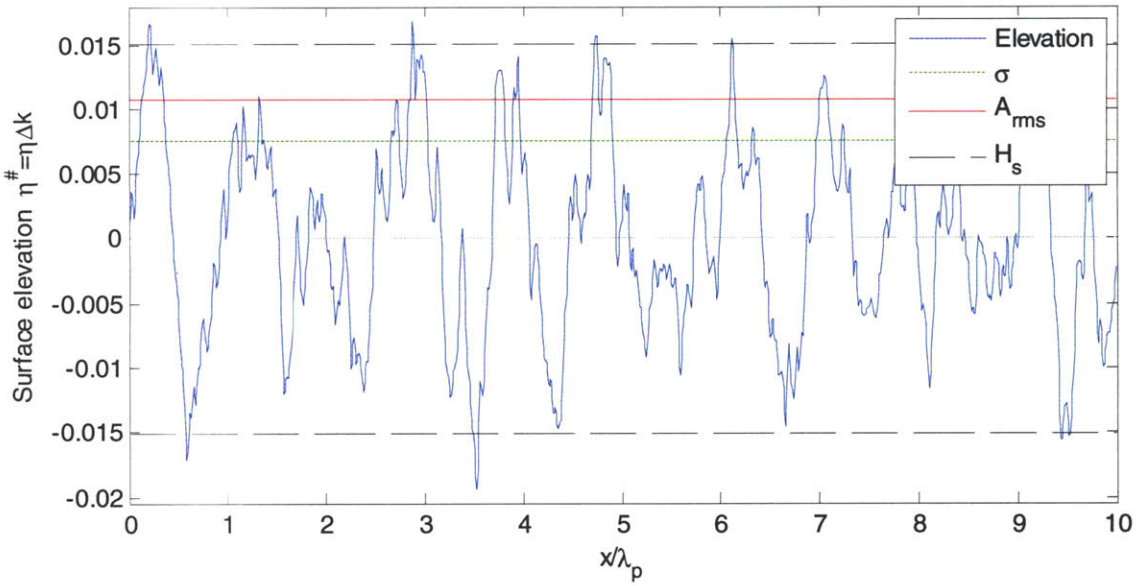

Figure 3.3 Surface elevation, standard deviation, RMS equivalent amplitude and significant wave height for Donelan et al. (1985) random sea state with wave age 10. Spectral resolution n_p=10.

3.2.6. Filtering and breaking dissipation

Dommermuth and Yue (1987) considered accumulation of numerical round-off errors and showed that it is manifested by instability of highest wavenumber modes which grow as $O(N^M)$. They suggested smoothing to stabilize the HOS simulations and applied different low-pass filters. It was found that such filters also allow simulations to continue beyond the moment of wave breaking, when a singularity in physics and equations invalidates the expansions on which HOS method is based. It was proposed that application of a low–pass filter can effectively simulate the energy loss due to breaking and be used as an efficacious numerics-based breaking dissipation model in absence of any conclusive theoretical alternative (Melville 1996).

Our wave breaking model is based on the observation that steep wavefields on verge of breaking posses higher spectral components that are necessary to express the finer spatial variation of the sharp crests. A low-pass filter models the dissipative process of wave breaking by removing these high spectral components when they appear. Different functional forms of filters were tried in course of the research; best results (in simulation duration sense) were obtained with

$$A_k^{filtered} = A_k \exp\left(-\left(\frac{k}{\beta_{scale} k_p}\right)^{\beta_{power}}\right) \tag{3.2.24}$$

applied at every time step (including Runge-Kutta substeps) to all the computed variables. Here β_{scale} is the nondimensional scale of breaking, interpreted as scaling of the cutoff wavenumber. β_{power} describes the sharpness of the filtering curve and may be associated with the intensity of breaking. Figure 3.4 illustrates the application of the filter in the spectral domain.

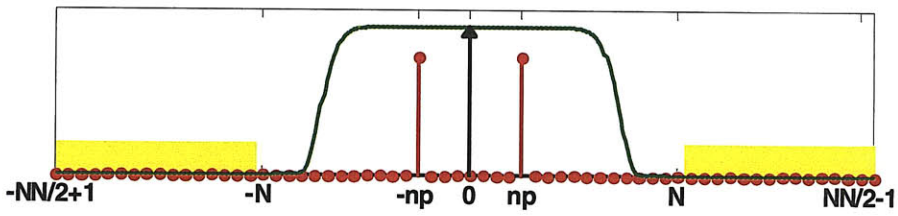

Figure 3.4 Wavenumber domain configuration of aliasing and wave breaking filters. See Figure 3.1.

Unfortunately, detailed examination of filtering process revealed fundamental difficulties. It was found that the energy removal is accompanied with volume inconsistencies. Spurious mass losses occurred at the intermittent wave breaking events and accumulated to 5-10% of the total displaced volume, when the simulations inevitably crashed. Figure 3.5 illustrates this process, see also Section 4.3.4. To allow progress despite this difficulty, it was circumvented by removal of the mean terms at every time step of the simulations. This numerical procedure forced artificial satisfaction of mass conservation principle. The physical consistency of the results obtained in this ad-hoc manner is still subject of investigation.

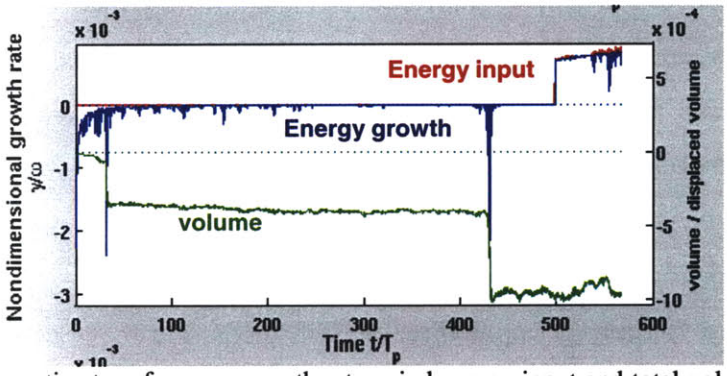

Figure 3.5 Nonlinear estimates of energy growth rate, wind energy input and total volume. Wind forcing is on at $t=500T_p$.

Another manifestation of the non-conservative effect associated with the spurious mass loss was intense oscillation of the nonlinear kinetic energy that followed wave breaking events. The kinetic energy deviated strongly from equipartition with potential energy and its growing irregular oscillations seemed to accompany simulation crashes. It may be speculated that the intense oscillations of the volume and the kinetic energy are related to wave breaking induced oscillations of mean surface and mean flow through a radiation stress mechanism; the oscillation of the kinetic energy is related to the vertical accelerations of the simulated system through Longuet-Higgins and Stewart (1960, p. 579) formula: $KE = KE_0\left(1+0.5g^*/g\right)$, where g* is the induced acceleration. To summarize, wave breaking appears to be inherently linked to violation of mass and energy conservation principles. Modeling of this non-conservative process requires further investigation.

3.2.7. Open questions

HOS method is an established and capable means for simulation and analysis of nonlinear waves. Its application for large scale simulation of realistic ocean wind waves requires, however, resolving the fundamental incompatibility of its energy conserving formulation and the ad-hoc non-conservative implementation. The key problem appears when wind energy input is added to a model that is stabilized by energy removal. The delicate balance of filtered out instabilities is disturbed, growth that was considered only a numerical artifact is now blended with a valid response to supplied forcing. Insufficient theoretical grounds of the subject contribute to the confusion, theory of non-conservative nonlinear waves appears to be lacking. As this thesis reports, the model can be restabilized by trial and error adjustment of computational parameters and numerically successful simulations can be produced. The mathematical validity of such simulations, however, has to be carefully examined and physical properties of the obtained solutions have to be understood. A proper analysis of the nonlinear response of wind forced wave system is required for correct application of HOS method to the realistic problem and in the process will necessarily advance the method itself.

Development of the theory behind the model is not finished. There are no rigorous bounds on computational parameters or theory for its convergence. There are no definite guidelines how to prevent simulation crash. The model was found to be unstable and by inspection this was attributed to spuriously growing round-off errors. More careful analysis may be required to trace the exact nature of these instabilities. Currently, the only way to stabilize the simulations is by removal of energy from the unstable modes. For each particular simulation configuration a set of computational parameters has to be found and details of the filtering adjusted.

Beyond the question of wind forcing, the general concept of phase resolved modeling for real ocean waves is not fully understood. Fundamental questions exist with regard to ergodicity, randomness and deterministic predictability of irregular broadband non-stationary wavefields (Huang et al. 1999, Liu 2000, Liu et al. 2002) and validity of their

representation in discrete spectral models (Bretherton 1964, Rasmussen and Stiassnie 1999, Tanaka and Yokoyama 2004, Lvov et al. 2006). Another question crucial for the HOS method is the effects broadbandedness, scale separation and long-short wave interaction (Brueckner and West 1988, Zhang et al. 1993). Effects of slow viscous dissipation also have to be included in a consistent theory supported way (Wu et al. 2006).

Chapter 4. Simulations and Numerical Results

4.1. *Wind forcing scheme*

The effect of wind forcing is modeled by wave induced slope coherent pressure

$$\frac{P_{wind}}{\rho_w} = \frac{\alpha_*}{\rho_w}\eta_x \tag{4.1.1}$$

The constant α_* is assumed a function of wave age in particular simulation. The forcing term is calculated in the spectral domain as

$$\frac{\hat{P}_{wind}}{\rho_w} = ik\frac{\alpha_*}{\rho_w}\hat{\eta}_k \tag{4.1.2}$$

and substituted into model's dynamic boundary condition equation (implemented numerically in the spectral domain with pseudo-spectral transformation for the nonlinear terms):

$$\psi_t = -g\eta - \tfrac{1}{2}\psi_x\psi_x + \tfrac{1}{2}(1+\eta_x\eta_x)\varphi_z\varphi_z - \frac{P_{wind}}{\rho_w} \qquad |_{z=\eta} \tag{4.1.3}$$

The constant α_* has dimensions of pressure, in model scaling it is

$$\alpha_*^{\#} = \frac{\alpha_* k_0}{\rho_w g} = \frac{\alpha_* k}{\rho_w g}\frac{1}{n} \tag{4.1.4}$$

By linear theory it is related to the nondimensional growth rate

$$\alpha_*^{\#} = \frac{\dot{E}}{\omega E}\frac{1}{n} \tag{4.1.5}$$

For $n=1$ (4.1.5) reduces to the scaled form of "surface pressure forcing level" (Banner and Song 2002). We generalize it for varying spectral resolutions and scale by the principal component. Explicitly, the applied forcing term in model units is

$$\left(\frac{\hat{P}_{wind}}{\rho_w}\right)_n^{\#} = ik_n^{\#}\alpha_*^{\#}\hat{\eta}_n^{\#} = ik_n^{\#}\frac{\alpha_* k_p}{\rho_w g}\frac{1}{n_p}\hat{\eta}_n^{\#} \tag{4.1.6}$$

Since we assume constant α_* for all modes, it is simply expressed in terms of the growth rate of the principal component

$$\frac{\alpha_* k_p}{\rho_w g} = \frac{\dot{E}_p}{\omega_p E_p} \tag{4.1.7}$$

Alternatively, if $\alpha_*(k) = \rho_a u_*^2 \alpha(k/k_p)$ is a known spectral function, same scaling is applied and forcing can be expressed in terms of wave age of the primary mode

$$\alpha_*^{\#}(n) = \alpha(n/n_p)\frac{\rho_a}{\rho_w}\left(\frac{c_p}{u_*}\right)^{-2}\frac{1}{n_p} = \frac{\alpha(n/n_p)}{\alpha(1)}\frac{\alpha_* k_p}{\rho_w g}\frac{1}{n_p} \tag{4.1.8}$$

In the following simulations the first alternative is applied.

4.2. *Validation of modeling*

Within the validity of the linear theory the amplitude is expected to grow exponentially

$$\frac{\partial A_k}{\partial t} = A_k \frac{\alpha_*}{2\rho_w \sqrt{g}} k^{3/2} \tag{4.2.1}$$

Energy input rate is estimated directly

$$\dot{\bar{E}}_{wind} = -\overline{P_{wind}\eta_t} \tag{4.2.2}$$

The full nonlinear energy balance is given by

$$-\overline{P_{wind}\eta_t} = \frac{\rho_w}{2}\frac{d}{dt}\left[\overline{\psi\eta_t} + g\overline{\eta^2}\right] \tag{4.2.3}$$

The first term on the right hand side is the average kinetic energy, the second – the average potential energy. Twice potential energy is the usual linear estimate of the total energy. In the following figures a simple forward Euler scheme time derivative of total energy is compared to the theoretical nonlinear energy input by the modeled wind-pressure distribution. The quadratic products are calculated in the physical domain, the vertical motion of the surface is taken directly from the nonlinear kinematic boundary condition equation

$$\eta_t = \varphi_z(1+\eta_x\eta_x) - \eta_x\psi_x \qquad |_{z=\eta} \tag{4.2.4}$$

4.2.1. Linear monochromatic growth

First, the consistency of modeling is verified for a single periodic linear wave. Figure 4.1 displays simulated surface elevation and amplitude spectrum after 25 periods. The simulated nondimensional growth rate is compared to the one expected for exponential growth in response to the applied forcing according to (4.2.1). The simulated exponential growth rate is constant as expected from linear theory, the relative error is $O(10^{-5})$.

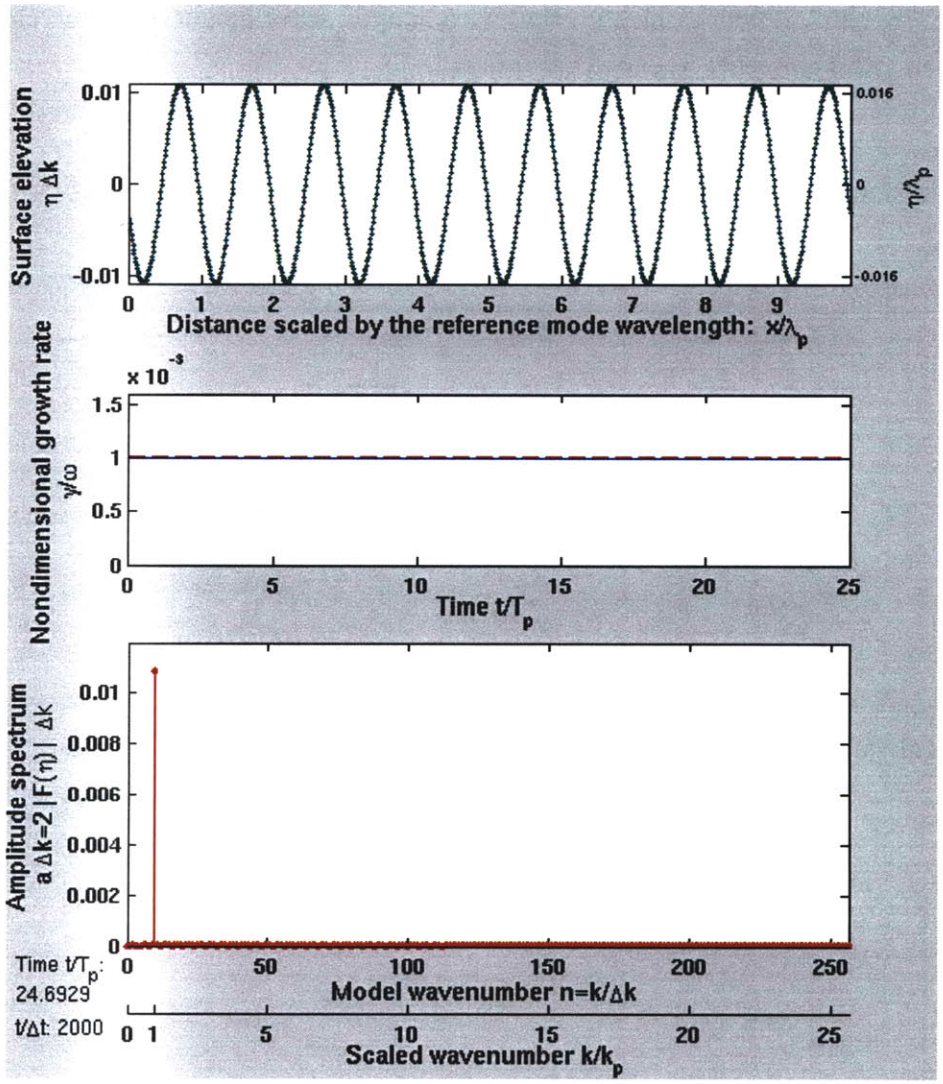

Figure 4.1 Top panel - surface elevation as function of horizontal coordinate; bottom panel – discrete amplitude spectrum as function of nondimensional wavenumber in model scaling and the wavenumber scaled by the characteristic wavenumber of interest k_p; middle panel - nondimensional growth rate $\dot{E} / E\omega$ as function of time, red dashed line – the theoretical expectation or the forcing level, blue line – simulated value.

The computational parameters: nonlinear order, space, spectral and time resolutions are

$$M=1,\quad R_{ph}=\frac{\lambda_p}{\Delta x}=102.4,\quad R_{sp}=\frac{k_p}{\Delta k}=10,\quad R_{time}=\frac{T_p}{\Delta t}=80.95 \tag{4.2.5}$$

The physical parameters: steepness, forcing level and implied wave age in this simulation are given by

$$a_p k_p=0.1,\quad \frac{\alpha_* k_p}{g\rho_w}=0.001,\quad \frac{c_p}{u_*}=6.3 \tag{4.2.6}$$

The corresponding dimensional simulated wave length, wave height, friction velocity and wind speed (10m above the surface) are, for example:

$$\lambda_p=9\ m,\quad H=0.3\ m,\quad u_*=0.6\ m/s,\quad U_{10}=17\ m/s \tag{4.2.7}$$

The conversions are calculated with following relations, given here for convenience of reference,

$$a_p k_p=\frac{H}{\lambda_p}\pi \tag{4.2.8}$$

$$\frac{c_p}{u_*}=\frac{g}{u_*\omega_p},\qquad u_*=\sqrt{\frac{g\lambda_p}{2\pi}}\Big/\frac{c_p}{u_*} \tag{4.2.9}$$

$$\frac{u_*^2}{U_{10}^2}=C_D,\qquad U_{10}=u_*/\sqrt{C_D} \tag{4.2.10}$$

$$\frac{\alpha_* k_p}{g\rho_w}=\frac{\dot{E}_p}{\omega_p E_p}=\frac{\rho_a}{\rho_w}\alpha\left(\frac{c_p}{u_*}\right)^{-2},\qquad \frac{c_p}{u_*}=\sqrt{\alpha\frac{\rho_a}{\rho_w}\Big/\frac{\alpha_* k_p}{g\rho_w}} \tag{4.2.11}$$

with typical values $1/\sqrt{C_D}=28$, $\rho_a/\rho_w=0.001225$, $\alpha=32.5$.

4.2.2. Nonlinear monochromatic growth

Nonlinear simulation is compared to the linear result from the previous section. All simulation parameters are kept the same except for the nonlinear order set to $M = 6$. Inspection of amplitude spectrum evolution reveals that harmonics of the principal component appear and enter recurrent oscillation pattern with period $O(5/3T_p)$. The nonlinear growth rate (4.2.2), nondimensionalized as $\dot{E}/E\omega_p$, oscillates between the linear implied growth rate to up to ~4% higher. This nonlinear modulation of wave growth is clearly the effect of the nonlinear harmonics that induce additional slope coherent pressure and enhanced energy and momentum flux from the wind. The comparison of the growth of the amplitudes of the principal harmonics between the linear and nonlinear simulations highlights the modulated growth of the nonlinear wave, which appears bounded from above by the linear amplitude. Comparison of the elevation profiles displays higher amplitude and faster phase velocity of the nonlinear wave.

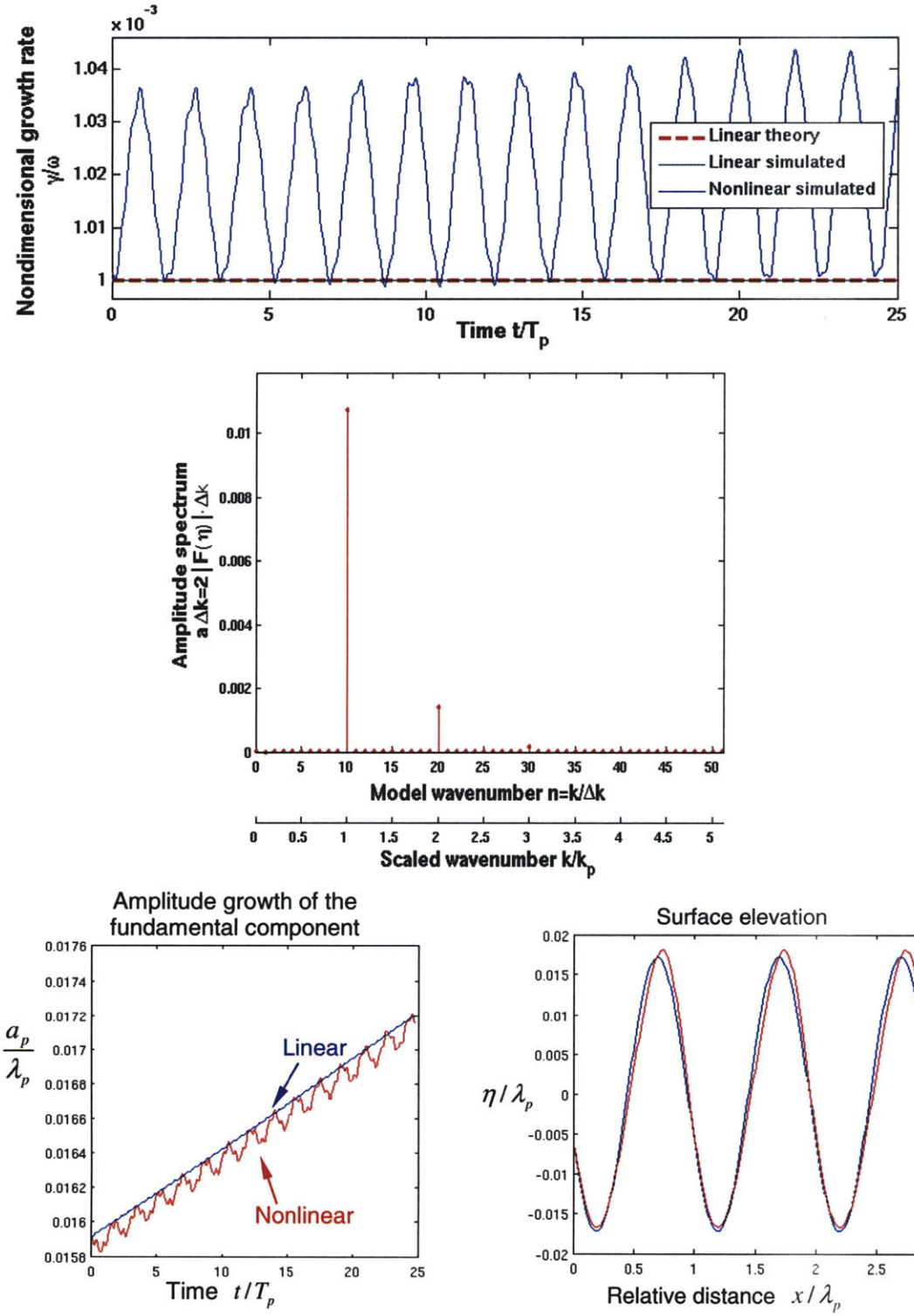

Figure 4.2 Comparison of the linear and nonlinear simulations. Upper panel – nondimensional growth rates $\dot{E}/E\omega$ (see the legend), middle panel – amplitude spectrum. Lower left panel – amplitudes of the principal component, lower right – surface elevations (blue line – linear elevation profile, red - nonlinear).

4.2.3. Linear broadband growth

Observed wind waves are irregular and have broadband spectra. Before proceeding to the nonlinear simulations of irregular waves, we examine a linear simulation of irregular wave field forced by wind. The linear growth of broadband spectrum is verified and is shown in Figure 4.3 below. Shorter waves are clearly growing faster by faster absorption of supplied wind energy in accordance with the linear theory (4.2.1). The overall growth rate is modified by the growing shorter components and gradually increases by an order of magnitude. Although this is clearly an unphysical situation, because real waves do not grow independently and nonlinearly interact, the understanding of this broadband effect may be valuable on smaller time scales. When nonlinear interactions are weak, shorter waves are expected to overgrow the longer waves before substantial nonlinear transport occurs in the spectrum.

The initial conditions in the examined simulation are Pierson-Moskowitz (1964) spectrum with steepness $a_{rms}k_p = 0.0569$. The forcing level is

$$\frac{\alpha_* k_p}{g\rho_w} = 0.0004 \tag{4.2.12}$$

simulating wave with wave age $\frac{c_p}{u_*} = 10$. The computational parameters are

$$M = 1, \quad R_{ph} = \frac{\lambda_p}{\Delta x} = 102.4, \quad R_{sp} = \frac{k_p}{\Delta k} = 10, \quad R_{time} = \frac{T_p}{\Delta t} = 80.95. \tag{4.2.13}$$

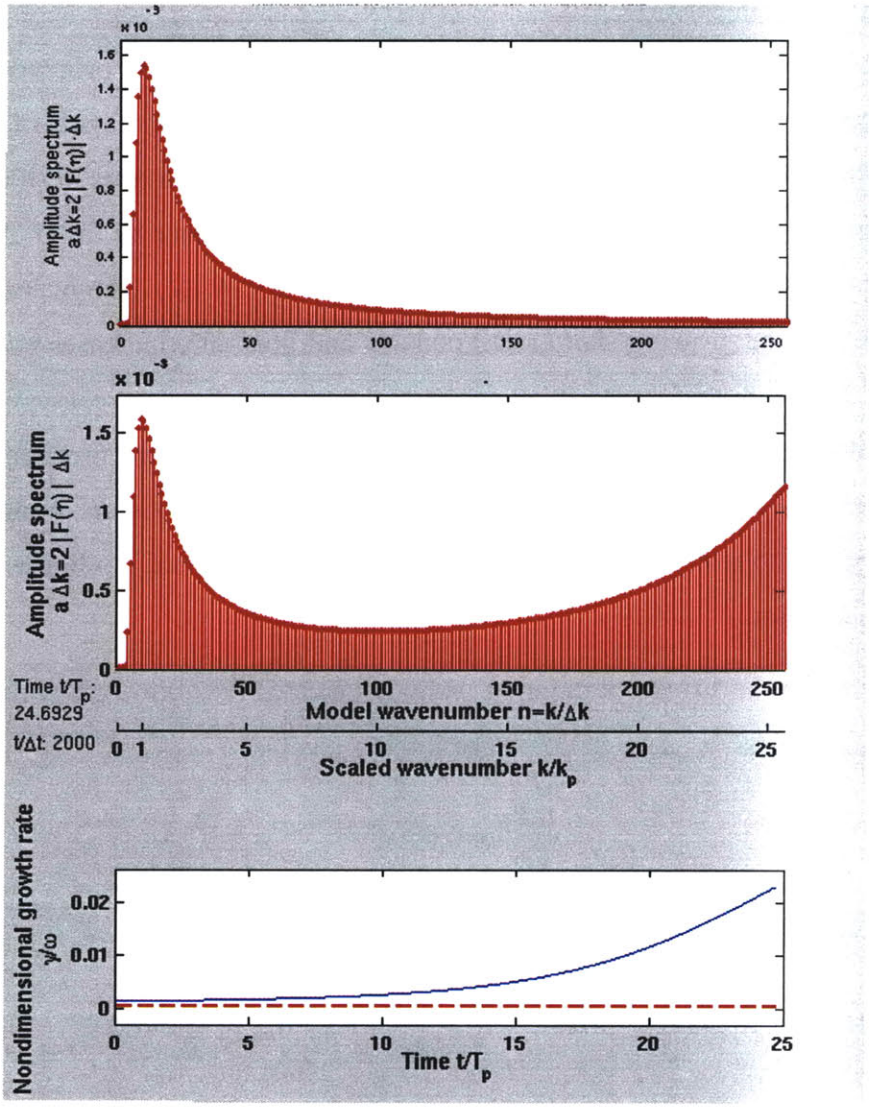

Figure 4.3 Linear simulation of broadband Pierson-Moskowitz wave field under steady wind. Upper panel – initial amplitude spectrum, middle panel – amplitude spectrum after 25 principal periods, bottom panel – integral nonlinear growth rate (blue) compared to the linear forcing level (red dashed).

4.2.4. Nonlinear broadband growth

When nonlinear interactions are allowed the picture of the growth is dramatically different. Spectral modes interact nonlinearly and growth of the shorter components is significantly reduced. The components at the spectral tail never grow to be of comparable magnitude with the principal components, as was the case in linear simulations. The combined integral growth rate oscillates erratically and simulations crash after short time $O(10T_p)$. Figure 4.4 illustrates the striking difference of a nonlinear simulation from the linear growth shown in Figure 4.3. The parameters of the simulation are kept the same, only the nonlinear order is set to M=5. We can notice the rough appearance of the elevation profile as well as of the amplitude spectrum. Oscillations of the total nonlinear growth rate are order of magnitude stronger than the forcing level and are negative during significant portion of simulation time. The simulation breaks in few time steps after t=5T_p, shown in the figure. It is hypothesized that it is wave breaking which appears to prevent the simulations to continue and therefore must be accounted for. It was found that a low-pass spectral filer successfully stabilizes the simulations and allows longer runs. The following sections describe development of these simulations. They demonstrate calibration of wave breaking filter and other simulation parameters for generation of longer wind coupled runs.

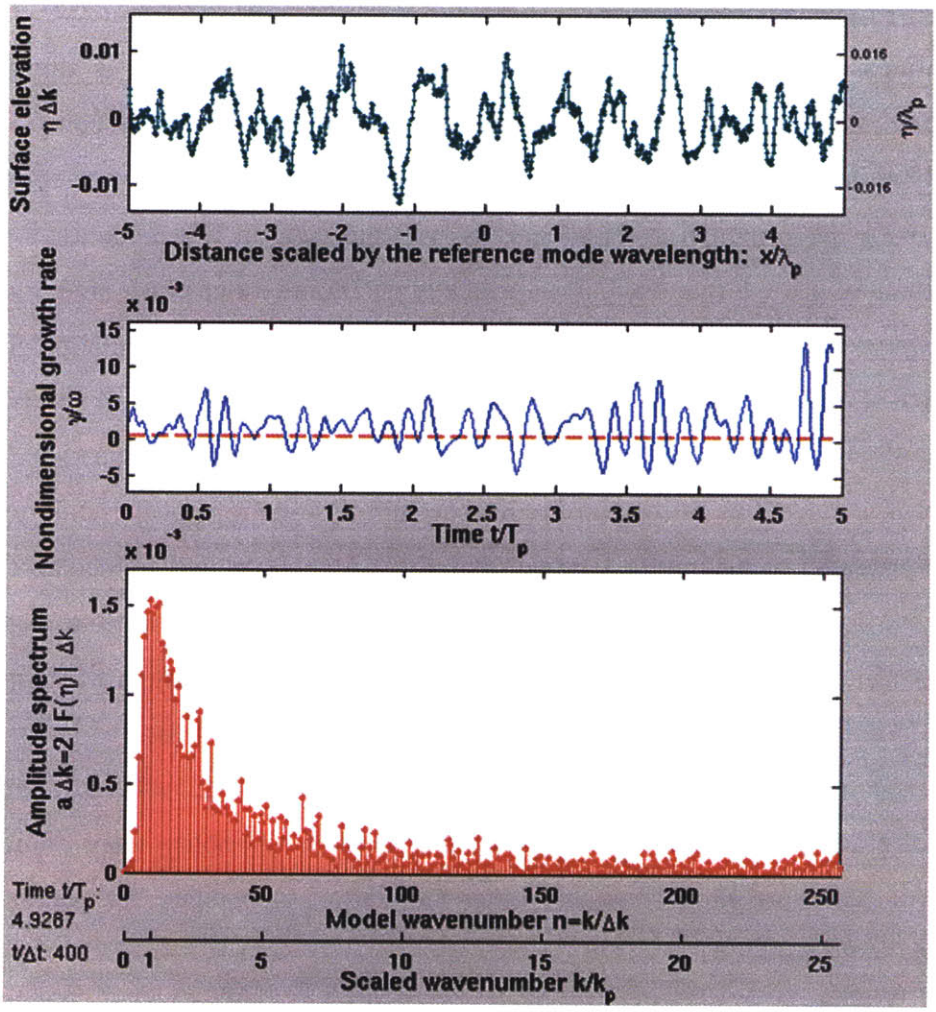

Figure 4.4 Nonlinear broadband Pierson-Moskowitz wave field. Top panel - surface elevation, bottom panel - amplitude spectrum, middle panel - nondimensional growth rate: nonlinear integral (blue), linear forcing level (red dashed).

4.3. *Simulation development*

4.3.1. Calibration of wave breaking filter

The key challenge in producing meaningful and lasting simulations with HOS method is to account for the non-conservative effect of wave breaking. The method originally was developed for simulation of swell conditions, i.e. free regular waves uncoupled with the wind. To account for the occasional breaking of free regular waves Dommermuth and Yue (1987) suggested to apply a simple low-pass filter, effectively assuming that high frequency components are unessential to description of energy containing wind waves. Continuous removal of shorter components was shown to conserve energy throughout the simulation except during isolated incidents of wave breaking, when the abrupt loss of energy is the expected effect. As will be seen throughout this Chapter, such simplified model of wave breaking performs reasonably well also for broadband simulations of irregular free waves. The breaking is mild and occurs in isolated bursts. However, when wind forcing is added waves start breaking intensely and continuously. A significant fraction of external energy supplied by the wind is not absorbed by the wave field but is lost to wave breaking. This non-conservative dynamical regime is principally different form the setting in which the original low-pass breaking filter was justified and calibrated. Delaying the theoretical discussion of the applicability of Dommermuth and Yue (1987) method to simulation of non-conservative irregular wind wave systems, in this Chapter we focus on development of the numerical simulations to run under wind forcing, starting with calibration of the breaking filter in this Section.

In Section 4.2.4. it was shown that nonlinear simulations of irregular broadband wave field under wind forcing result in erratic oscillations of the growth rate which are difficult to compare with the theoretical expectations. Application of low-pass wave breaking filter described in Section 3.2.6. significantly reduces these irregular fluctuations and smoothes the rough appearance of the simulated elevation profile. The performance, however, noticeably depends on the chosen values of filter parameters as well as the level

of simulation discretization. Many simulations with different choice of parameters were examined in process of model calibration, few principal simulations are demonstrated and discussed below.

An *adaptive* low-pass filter was considered as a modification of the original rigid wave breaking filter to account for the evolving spectrum. The idea is to continuously monitor the properties of the evolving wave field and adjust the breaking model to better represent the underlying physical process. In the example shown in Figure 4.5, the adaptive filter calculates a power weighted average wavenumber every time step, which is substituted for the peak wavenumber in (3.2.24). The resulting filter adjusts its band-pass scale to the bandwidth of the evolving spectrum and generates smoother dissipation then the rigid filter. In Figure 4.5 and Figure 4.6 two otherwise identical simulations are compared after 100 characteristic periods, in Figure 4.5 the adaptive filter is applied while Figure 4.6 presents simulation filtered with a rigid filter. Wind forcing is applied after 10 T_p, the nonlinear wind energy input is shown by the red line in the middle panels. The striking difference between the simulations is seen comparing the growth rate response (blue line) of the broadband wave fields. The adaptive filter produces smoother growth, as the energy supplied by the wind is absorbed by the wave field. With the rigid filter the growth rate is more intermittent, the more violent wave breaking causing an order of magnitude stronger volume inconsistencies $O(10^{-3})$ vs. $O(10^{-4})$ for the adaptive filter. Comparison of elevation fields shows that adaptive filtering generates smoother profile, but retains qualitative similarity of the phase resolved features.

Effect of large breaking scale and higher spectral resolution (n_p=20) is illustrated in Figure 4.7 and Figure 4.8. Relatively strong discrete wave breaking event at T_p=32 is correlated with clear volume loss (green line). On longer time scale volume inconsistency reaches ~5% of the total displaced volume, then simulations fails. The amplitude of fluctuations of the integral growth rate (blue line) grows one order of magnitude over the integral wind input rate (red line), masking the direct comparison between the two. Qualitatively inspecting the spectrum we conclude that no downshift is observed and no subharmonic components develop even after several hundreds T_p.

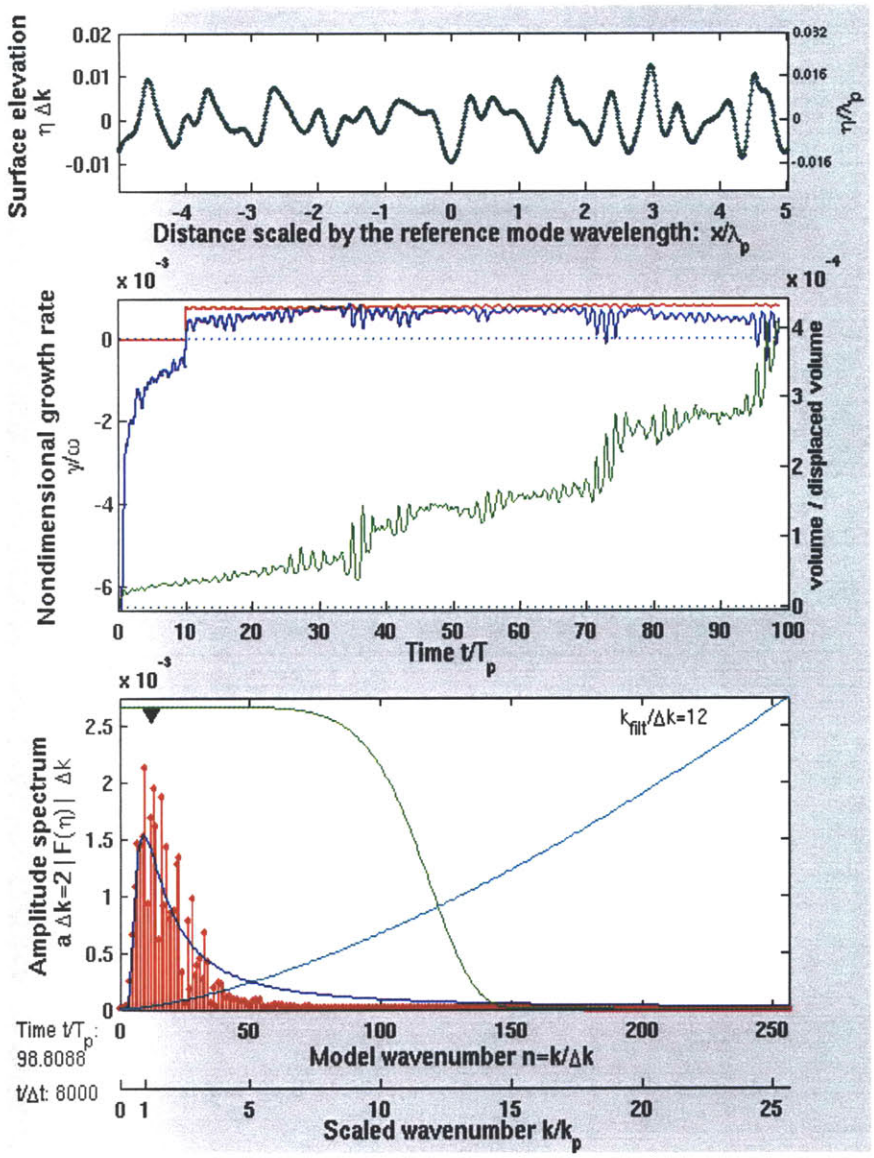

Figure 4.5 Adaptive filter. Top panel - surface elevation; bottom panel - amplitude spectrum (red stem), initial amplitude spectrum (blue), breaking filter (green, shown arbitrarily scaled), wind input rate (cyan, shown arbitrarily scaled); middle panel - nondimensional nonlinear integral growth rate (blue), nonlinear integral wind input (red), volume deviation (green). Spectral resolution n_p=10, Wind starts at 10 T_p. Initial spectrum Pierson-Moskovitz. Low-pass filter parameters [β_{scale} , β_{power}]=[10,8].

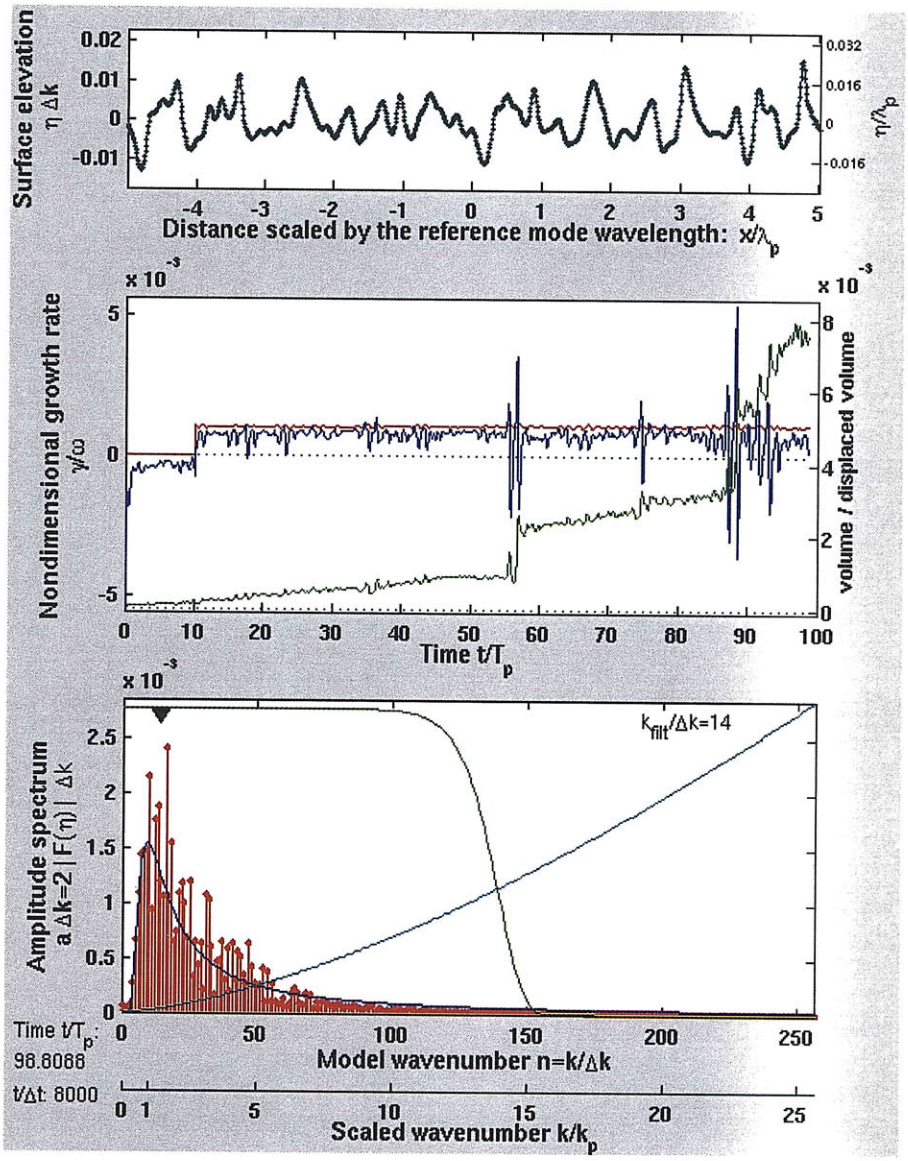

Figure 4.6 Same as in Figure 4.5 only for rigid filter.

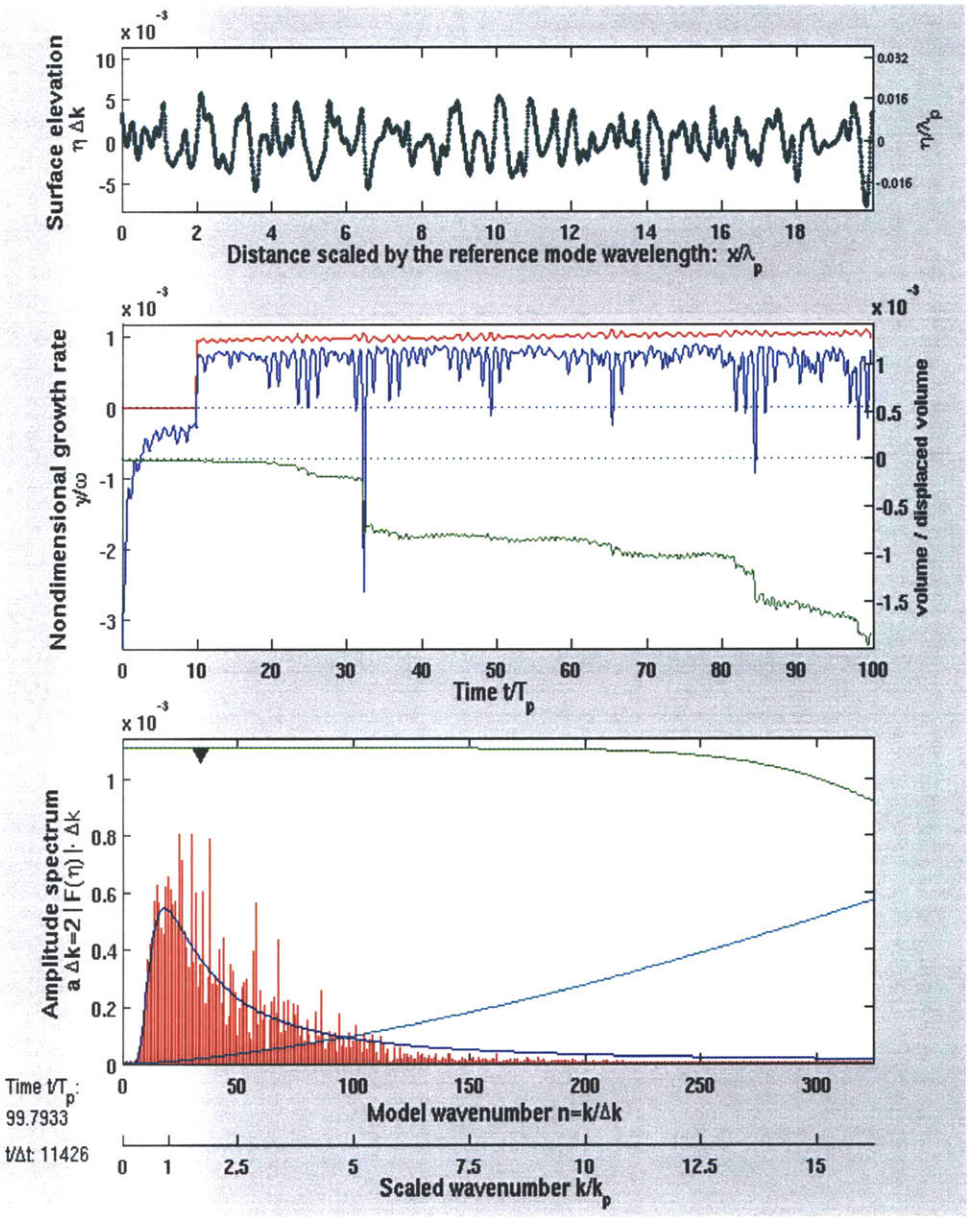

Figure 4.7 Same variables displayed as in Figure 4.5. The spectral resolution n_p=20. Initial spectrum Pierson-Moskovitz. Low-pass filter parameters [β_{scale} , β_{power}]=[20,8]. Shown at T_p=100.

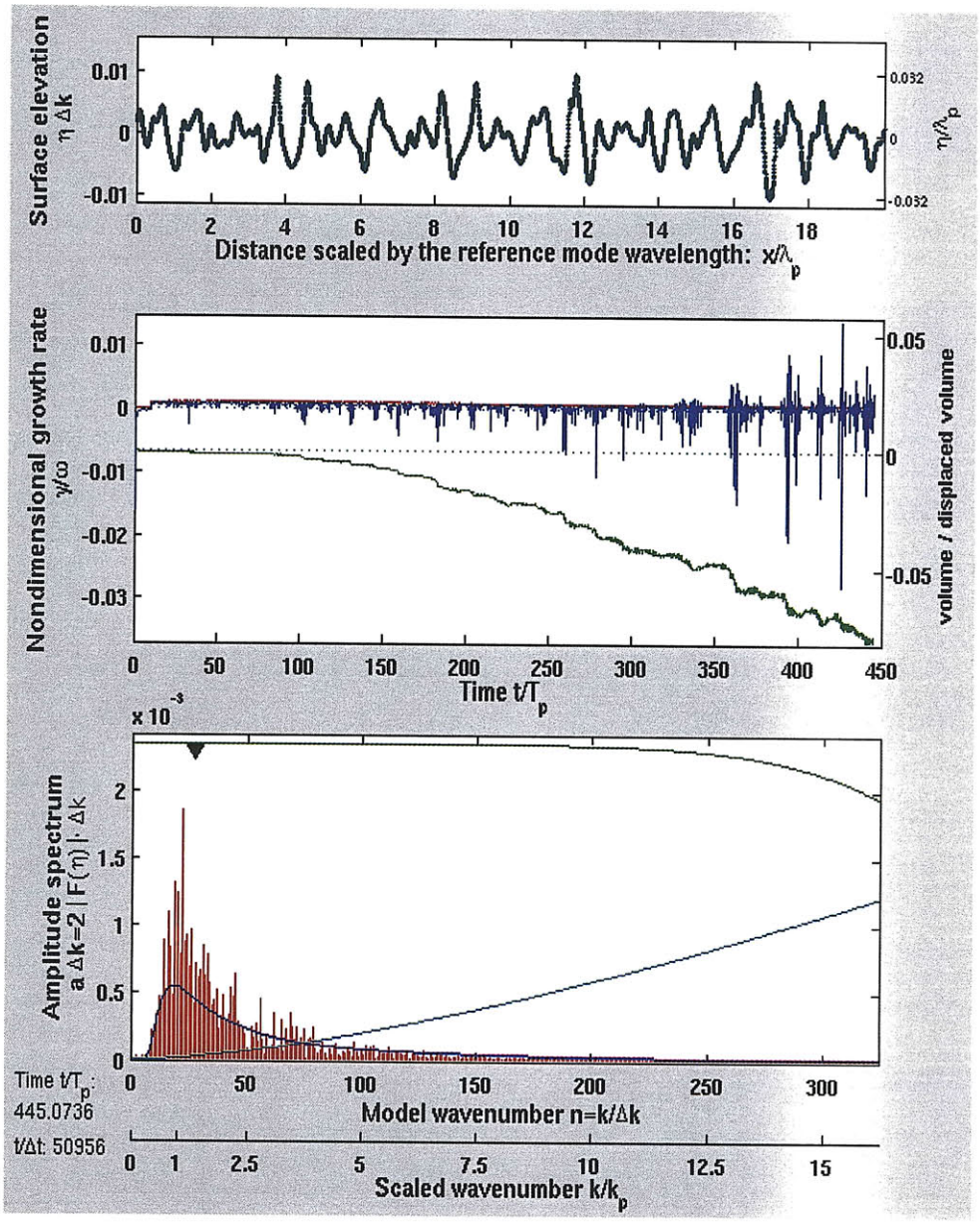

Figure 4.8 Same as in Figure 4.7, shown at T_p=450.

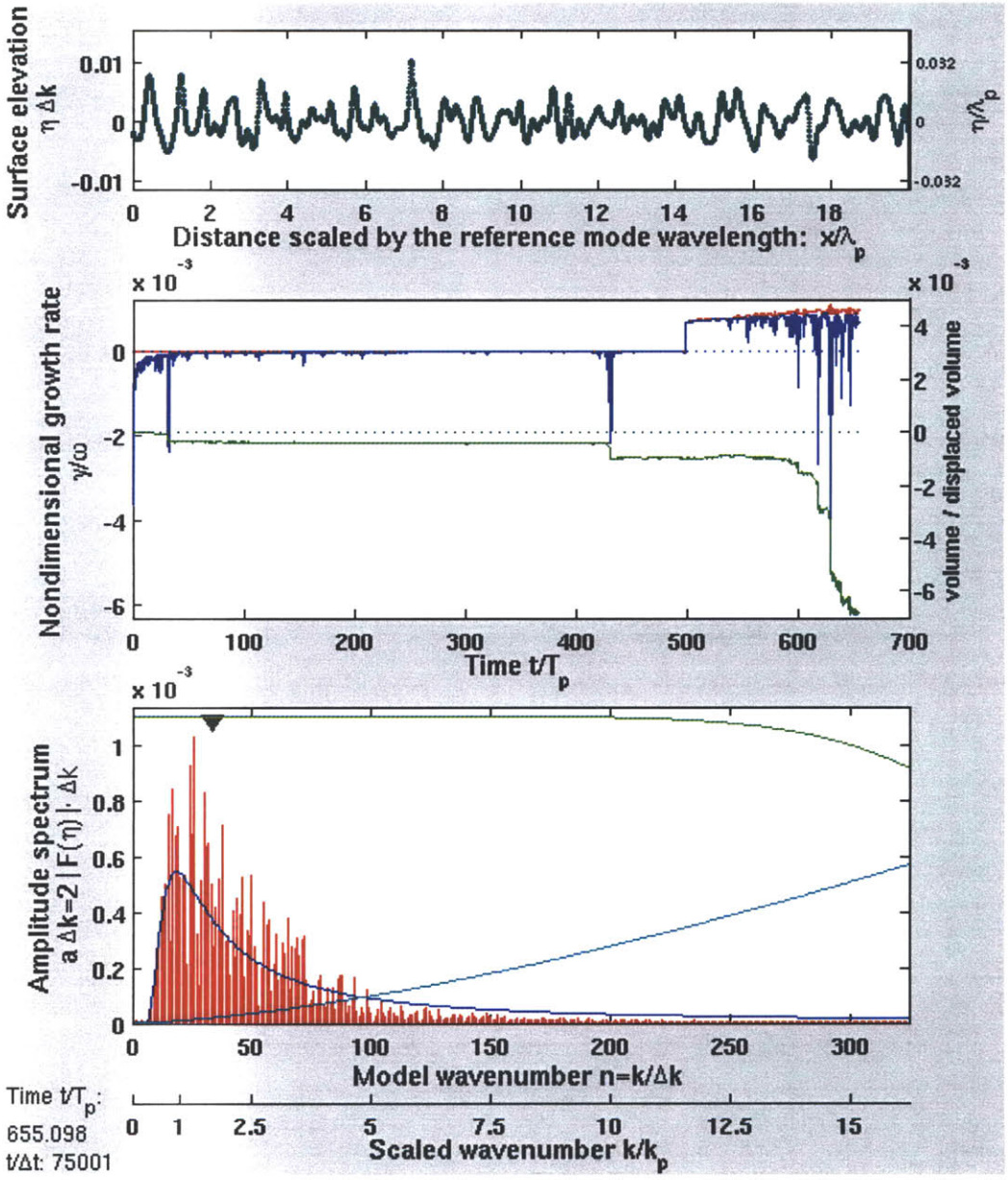

Figure 4.9 Same as Figure 4.7, wind starts at T_p=500. Shown at T_p=655. Spectral resolution n_p=20, low-pass filter parameters [β_{scale} , β_{power}]=[20,8].

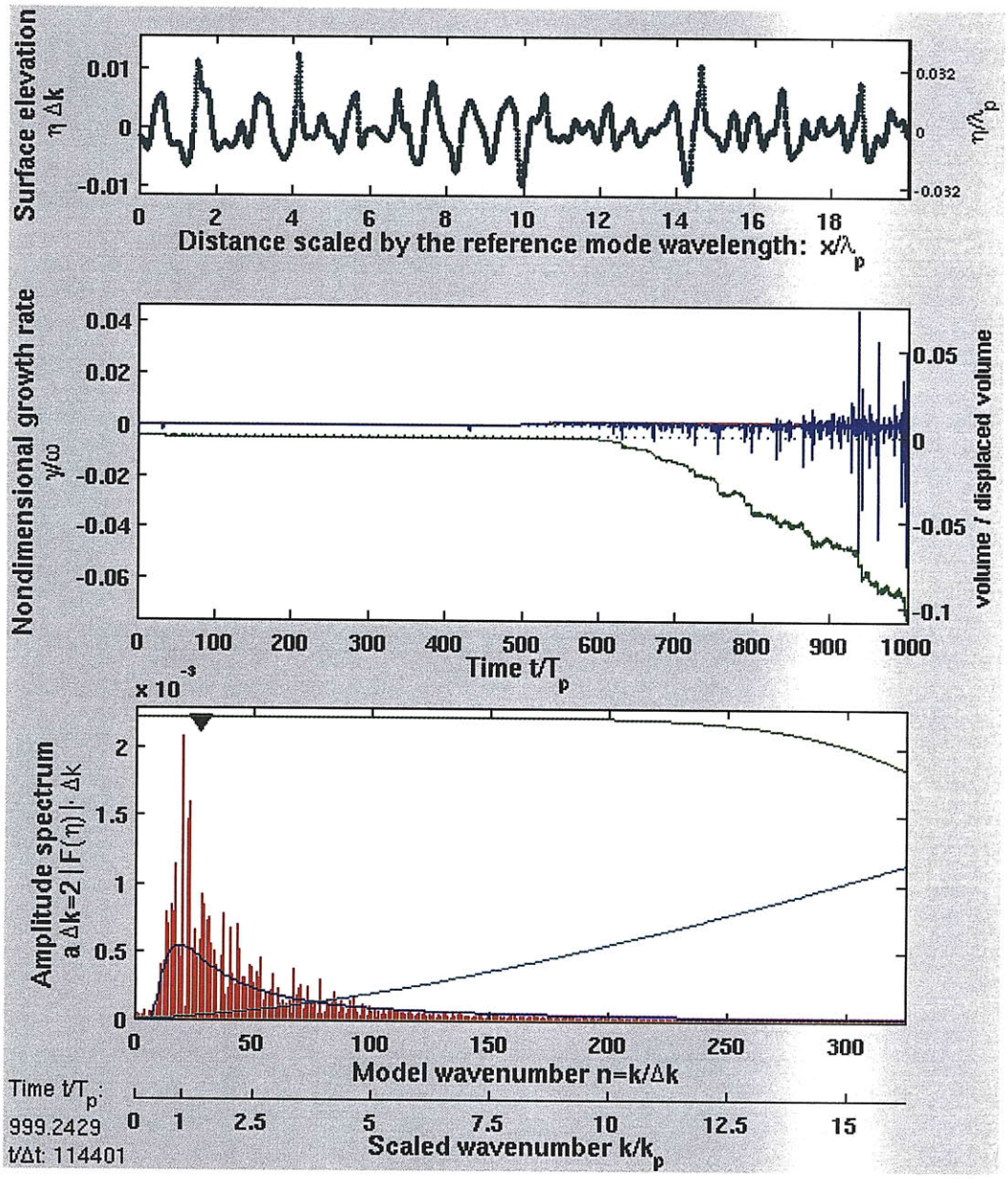

Figure 4.10 Same as Figure 4.9. Shown at T_p=1000.

To allow simulations the time to properly adjust to the initial conditions, wind forcing was applied only after 500 T_p of wind free propagation. In simulation shown in Figure 4.9 and Figure 4.10 the computational parameters were calibrated to allow long evolution $O(10^3 T_p)$. The spectral resolution was set to n_p=20, total number of simulated modes was 4096, with N=1024 physically significant modes, time resolution was 115 and nonlinear order set to M=7. Wave breaking filter was applied with $[\beta_{scale}, \beta_{power}]$=[20,8]. The fine resolution allowed detailed inspection of the transition from wind free propagation to wind forced wave growth. It is seen that during 500 periods of wind free propagation energy growth rate is close to zero and negative fluctuations are localized, allowing quantitative framing of wave breaking events. Volume inconsistency is perfectly correlated with discrete wave breaking events.

Volume inconsistency highlights the transition between two qualitatively different states of the wave field. When wind forcing is abruptly turned on, the growth rate initially follows it very closely. The waves absorb all the energy supplied by the wind. Gradually, wave breaking appears, seen in the negative bursts and deviation of the growth rate curve from the wind input curve. Volume loss is correlated with wave breaking and helps indicate the transition from isolated breaking events to the intermittent state of continuous growing and breaking. Eventually, the fluctuations of the growth rate grow 2 orders of magnitude stronger than wind input, which complicates the direct comparison but indicates the turbulent intermittent state of irregular growth. Volume conservation deteriorates monotonically, reaching ~10% of the total displaced volume after $1000T_p$.

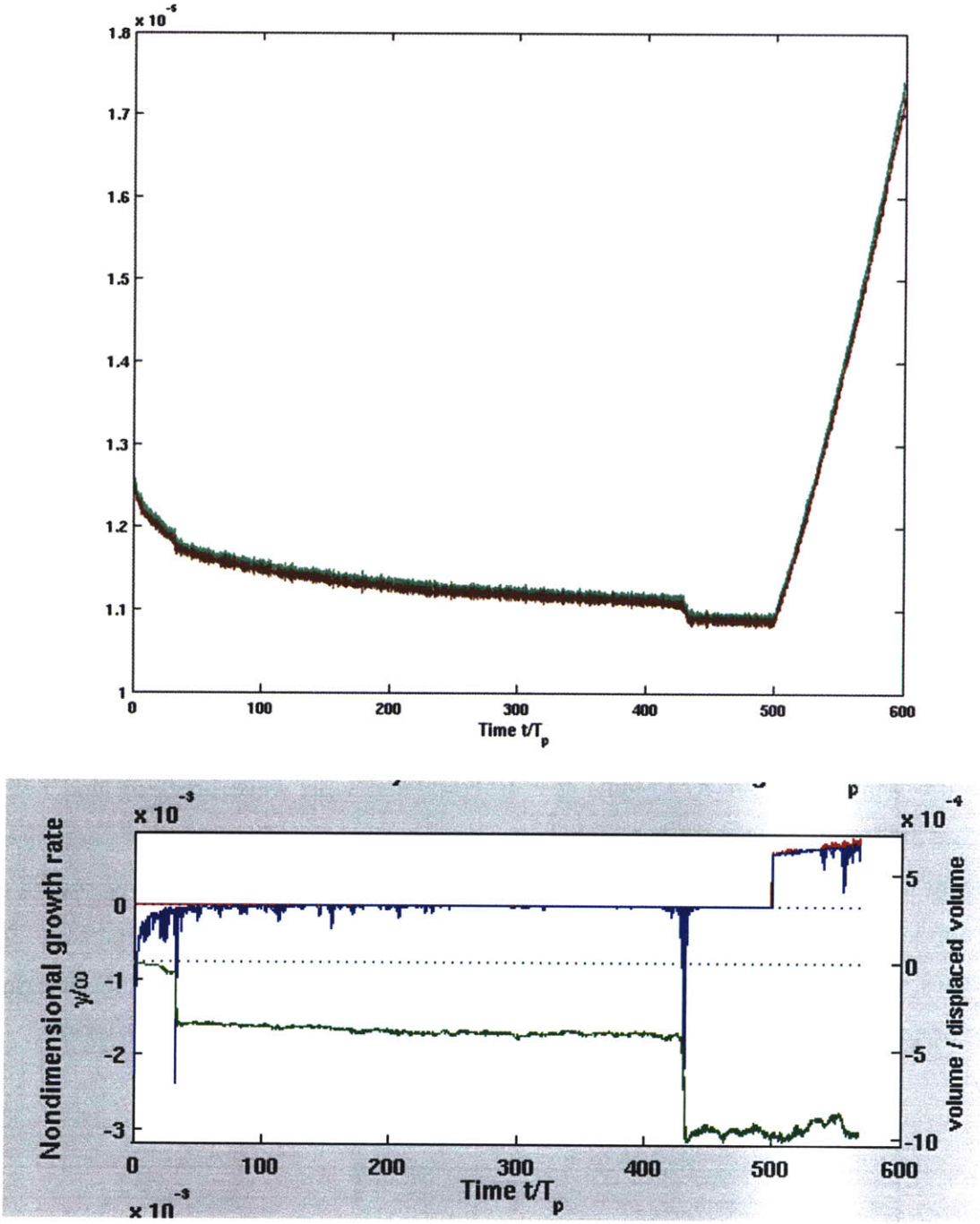

Figure 4.11 Upper plot - Kinetic (green) and potential (brown) energy in model units. Bottom plot - Nondimensional growth rate of growth (blue) and wind input (red), and relative volume (green). Both plots are shown with same timeline for ease of visual correlation of energy loss and growth with wind energy supply.

Additional illustration of wave breaking and wind forced growth appears in Figure 4.11 there kinetic and potential energies are plotted to display the correlation of energy drop with growth rate bursts and volume drops around times 40 and 430 T_p and the fast smooth growth of energies during the initial growth under wind, when wave breaking is still mild. This figure illustrates the energetic balance expressed by equation (4.2.3), where the red curve corresponds to the left hand side and the blue curve to the right. The zoomed view in Figure 4.12 allows a detailed inspection of the wave breaking process. It is seen that the wind free burst at time 430 T_p is not immediate and spans O(5 T_p) which takes hundreds of time steps to simulate. The good alignment of growth rate with wind input during the first 50 T_p of wind forced growth validates our modeling approach for the case of nonlinear growth of irregular wave field. This direct comparison of nonlinear wind input with nonlinear growth highlights the transition from initial smooth growth to a qualitatively different stage of evolution after intermittent wave breaking appears.

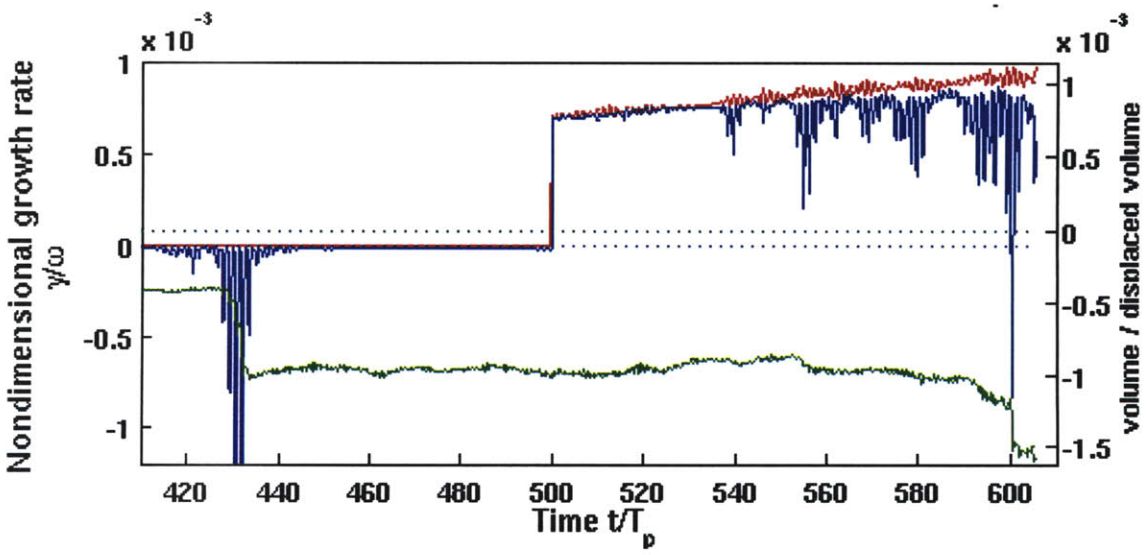

Figure 4.12 Same as bottom panel of Figure 4.11 zoomed in time. Highlights the details of the transition from wind free localized breaking, to smooth growth and to intermittent breaking response to wind forcing.

4.3.2. Energetics of filters

An attempt to examine the numerical details of the inconsistency between the nonlinear wind input and the nonlinear response of the wave field is presented below. In previous section it was implicitly assumed that the inconsistency in wave response to the supplied energy is fully due to the coinciding loss to wave breaking, which is simulated by a low-pass filter. Additional explanations of inconsistency might be, in principle, numerical inconsistency and loss to the aliasing filter. Direct calculation of energy loss in wave breaking filter (yellow line) is compared in Figure 4.13 to the integral nonlinear growth rate (blue). The net expected growth (brown), which is the breaking loss added to the nonlinear wind input (red), appears closer to the simulated growth but still does not coincide for the lower spectral resolution on Figure 4.13. In the higher resolution simulation, see Figure 4.14, the consistency is better, indicating convergence with increasing spectral and physical resolution. In the long run, however, (Figure 4.15) wave breaking intensifies and the negative growth rate bursts still appear stronger than rates of energy removal by the wave breaking filter. This indicates that the inconsistencies are still unresolved.

The forcing level in both displayed simulations was

$$\frac{\alpha_* k_p}{g\rho_w} = 0.0004 \tag{4.3.1}$$

For lower resolution simulation shown in Figure 4.13 computational parameters are

$$M = 5, \quad R_{ph} = \frac{\lambda_p}{\Delta x} = 102.4, \quad R_{sp} = \frac{k_p}{\Delta k} = 10, \quad R_{time} = \frac{T_p}{\Delta t} = 80.95 \tag{4.3.2}$$

The initial conditions are Pierson-Moskowitz spectrum. Wave breaking filter is fixed with parameters $[\beta_{scale}, \beta_{power}]$=[14,16].

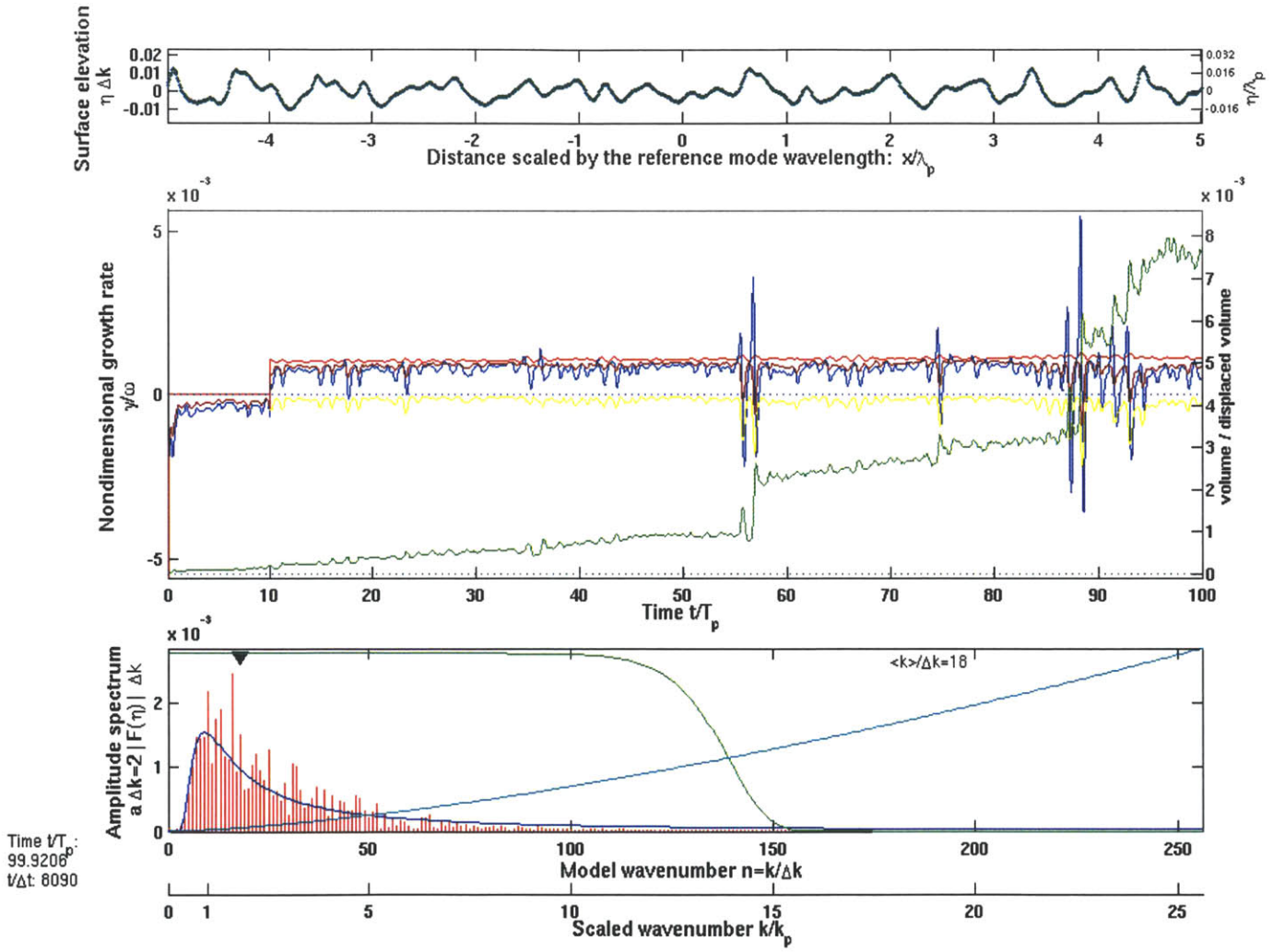

ure 4.13 Same simulation as in Figure 4.6. Additional curves for energy loss in wave breaking filter (yellow) and the net expected growth (brown) ed to the middle panel.

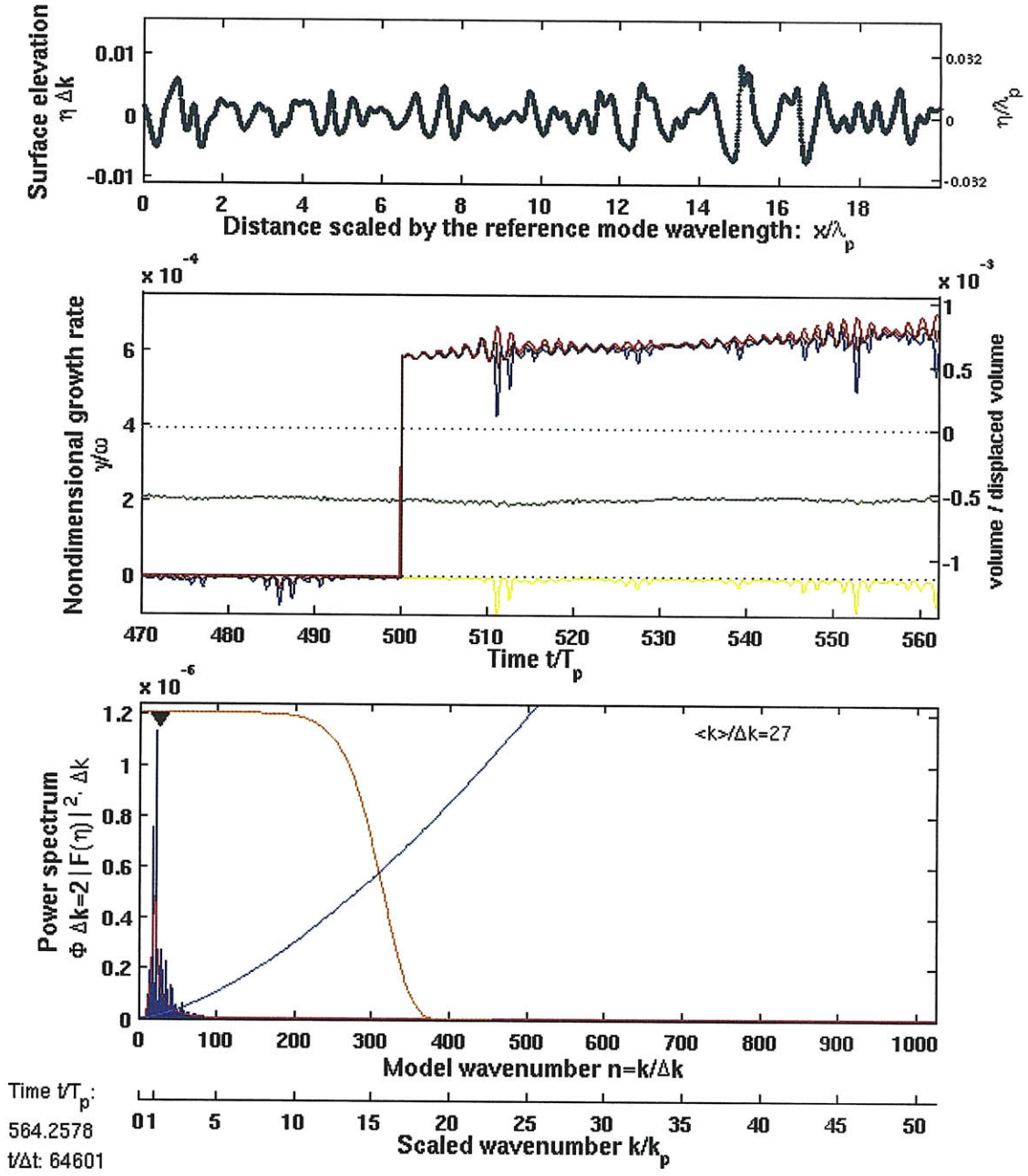

Figure 4.14 Same analysis as displayed in Figure 4.13 for higher resolution simulation as described in the text.

For high resolution simulation, shown in Figure 4.14 and Figure 4.15 the computational parameters are

$$M = 7, \quad R_{ph} = \frac{\lambda_p}{\Delta x} = 204.8, \quad R_{sp} = \frac{k_p}{\Delta k} = 20, \quad R_{time} = \frac{T_p}{\Delta t} = 114.5 \qquad (4.3.3)$$

Initial conditions are JONSWAP spectrum for wave age 10. Adaptive low-pass wave breaking filter was applied with parameters $[\beta_{scale}, \beta_{power}]=[12,10]$.

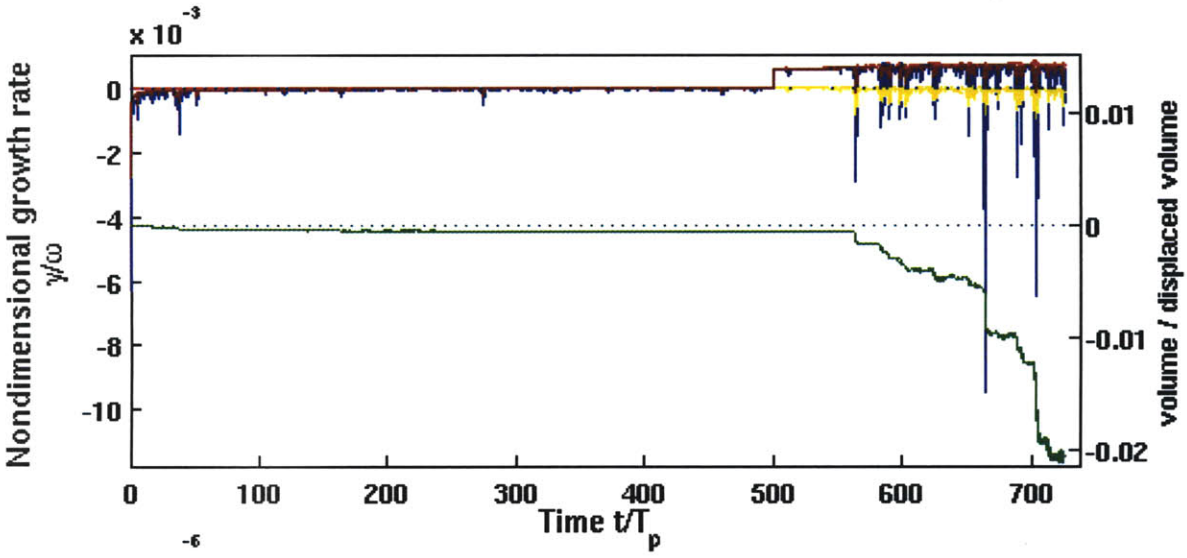

Figure 4.15 Same simulation as in Figure 4.14. The middle panel is displayed for longer time.

4.3.3. Estimation of frequency downshift

Multitude of spectral components included in HOS phase resolving simulation contain large amount of information, analysis and presentation of which is a nontrivial task. Time plots of amplitude evolution of the spectral components is a typical means of analysis in theoretical studies of nonlinear waves (Yuen and Lake 1982) as well as in qualitative discussions of simulated wind wave evolution (Hara and Mei 1991). Typical amplitude evolution plot for HOS simulation, top plot in Figure 4.16, contains too much information to be useful directly. Qualitative conclusions can be drawn, however, regarding the transition from wind-free propagation to wind-forced growth. A qualitative change in dynamics is evident after wind forcing is applied (at 500 T_p) – the evolution is clearly more hectic, the nonlinear energy exchange between modes is faster, single components dominate the spectrum for shorter periods than for free nonlinear waves. Reducing the amount of information by averaging allows drawing more quantitative conclusions. Different estimates of spectral moments and averages are presented in bottom plot of Figure 4.16. From theoretical perspective it is not straightforward to decide which is the most suitable for a simplified description that will capture most of the physics. The peak mode index – the direct equivalent of the peak frequency traditionally examined in observational studies, seems to jump sporadically prohibiting the usual interpretation. Some higher moments have magnitudes close to it (clearly biased to max mode due to the high power averaging), but their detailed dynamics are not easy to interpret at this stage, although they may become valuable for deeper theoretical examination. Amplitude weighted average and second moment in amplitude convey additional information because both capture the temporary increase in higher frequency components during the strong breaking event around 430 T_p. The power weighted average wavenumber (black line) has the smallest scatter and allows convenient interpretation as the wave number of the dominants waves. Therefore we choose it for representation of the characteristic wavenumber, instead of the peak wavenumber, for estimation of simulated frequency downshift.

Examination of all the presented spectral statistics in Figure 4.16 adds to understanding of the simulated transition from wind free evolution to wind forced growth. During the first 500 T_p of free propagation the simulation adjusts to the unbalanced initial conditions (a known unresolved issue with HOS method). Significant downshift is observed in all the averaged statistics during the first 100 T_p. The maximum discrete wavenumber (the mode), however, starts from the low initial value (in model scaling - 20) and jumps sporadically during the first 200 T_p of adjustment between wavenumbers 20 and 40 before settling at 25. The transient period (100-200 T_p) and the established swell state (200-500 T_p) are also evident in the amplitude evolution plot, where the 25^{th} wavenumber dominating the swell system is seen to rise from the turbulent chaos of nonlinearly interacting spectral components. The strong wave breaking event around 430 T_p is captured by some spectral moments, but is completely unnoticed by the maximal mode and the higher power spectral averages. When the wind is applied at 500 T_p, all the spectral statistics display upshift of the spectrum during first 200 T_p of adjustment to the wind. Since many simulations crushed during this unbalanced stage – i.e. this opposite trend of upshift which contradicts the observed and expected downshift, it was a major question of validity of HOS to be applied to simulation of realistic wind waves. The success of extending the simulations beyond this transient period was crucial to allow the expected downshift to be obtained. This simulated downshift will be shown in the following sections to be in reasonable accordance with observations. Additional insight about the established wind forced dynamics can be obtained from the large scatter of the high frequency sensitive moments. This scatter is comparable to the large breaking event at 430 T_p and suggest domination of wave breaking during wind forced growth as opposed to the localized breaking during wind free evolution.

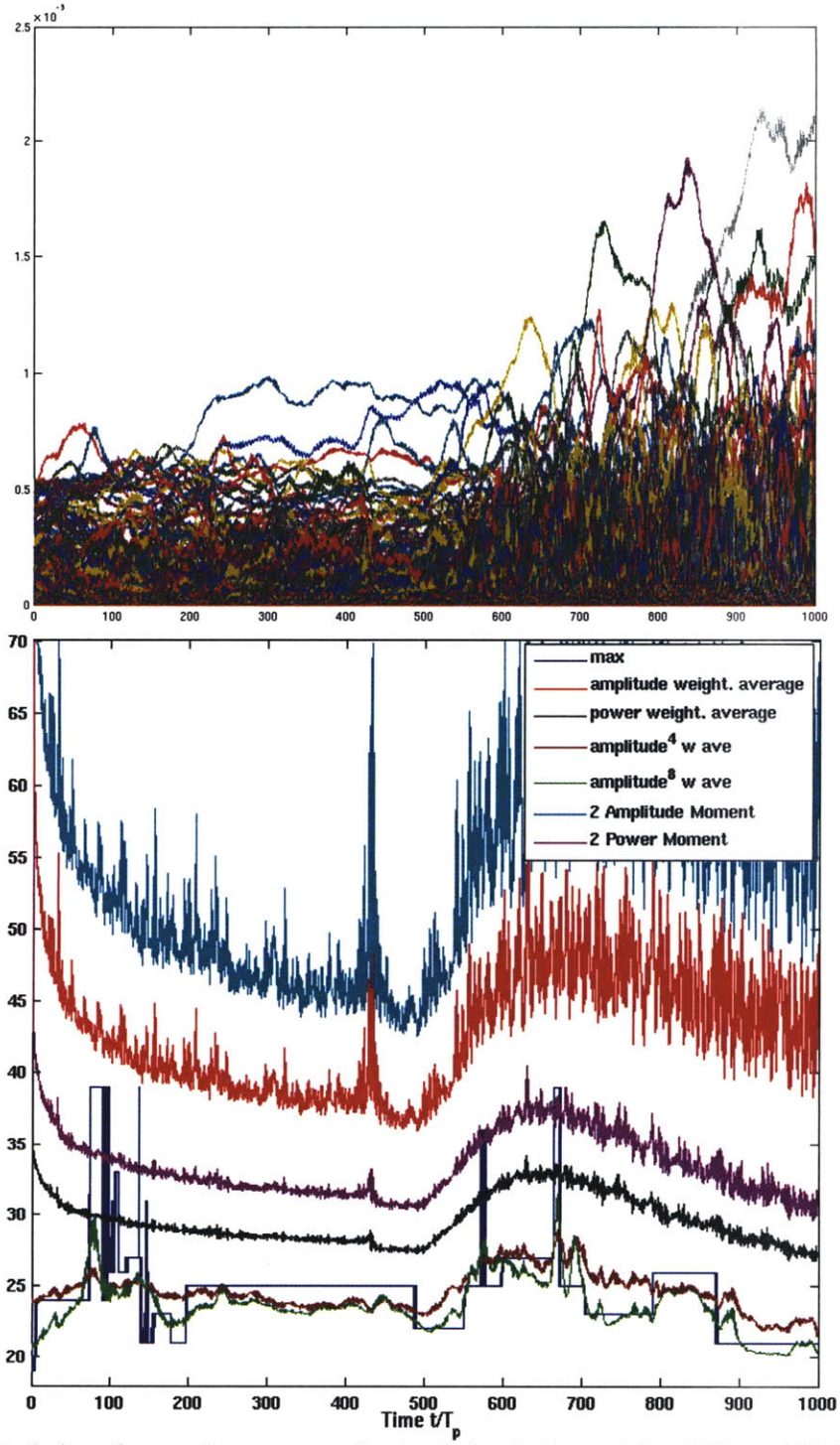

Figure 4.16 Evolution of spectral components for simulation in Figure 4.9 and Figure 4.11. Upper panel – time series of amplitudes. Lower panel - time series of spectral averages and moments: spectral mode (max wavenumber) – blue, amplitude weighted mean – red, power weighted mean – black, amplitude power 4 weighted mean – brown, amplitude power 8 weighted mean – green, second moment in amplitude – cyan, second moment in power - magenta.

4.3.4. Volume loss and elimination of mean term

The major challenge of wind wave modeling with HOS method is generation of long enough simulations to verify observed evolution on time scale of 10^3-10^4 T_p, see Section 2.1.3. This appeared to be a nontrivial task since the original method was calibrated for simulation of wind free waves, for which wave breaking is mild and the accumulating round-off errors were successfully removed by a simple low-pass filter. Wind forced simulations appeared to be more susceptible to numerical failure because energy supplied by the wind interfered with the fragile balance between nonlinear interactions and energy removal from high frequency spectral components. Physically, the dynamics of windsea are inherently non-conservative; the balance of simulated nonlinear interactions, energy input and loss should be consistent with physics of the system and should not be spoiled by application of artificial numerical dissipation. As it was reported in previous sections, long wind forced simulations and intense wave breaking resulted in large volume inconsistencies. Simulation failure appeared to always be associated with volume loss order of 5-10% of the total displaced volume. Detailed examination of wave energetics revealed that while the linear estimate of wave energy maintained limited fluctuations, the nonlinear estimate developed wild fluctuation order of magnitude stronger than the linear energy, see Figure 4.17 and Figure 4.18. Further, it was noticed that the fluctuations appeared only due to the kinetic energy, which is obvious, since the linear energy estimate is just twice the potential energy. Detailed examination of wave breaking events showed that volume loss and energy instability are correlated, which lead to the hypothesis that the simulated kinetic energy fluctuation may be explained by Longuet-Higgins and Stewart (1960) formula for wave energy in vertically oscillating frame of reference. As an alternative to the detailed investigation of the nature of energy fluctuations and volume loss, in this Thesis we choose to simply eliminate these effects numerically by continuous removal of the mean terms.

Figure 4.17 and Figure 4.18 below illustrate the effect of this numerical procedure. It is shown that fluctuations of kinetic energy are removed with negligible effect on energy

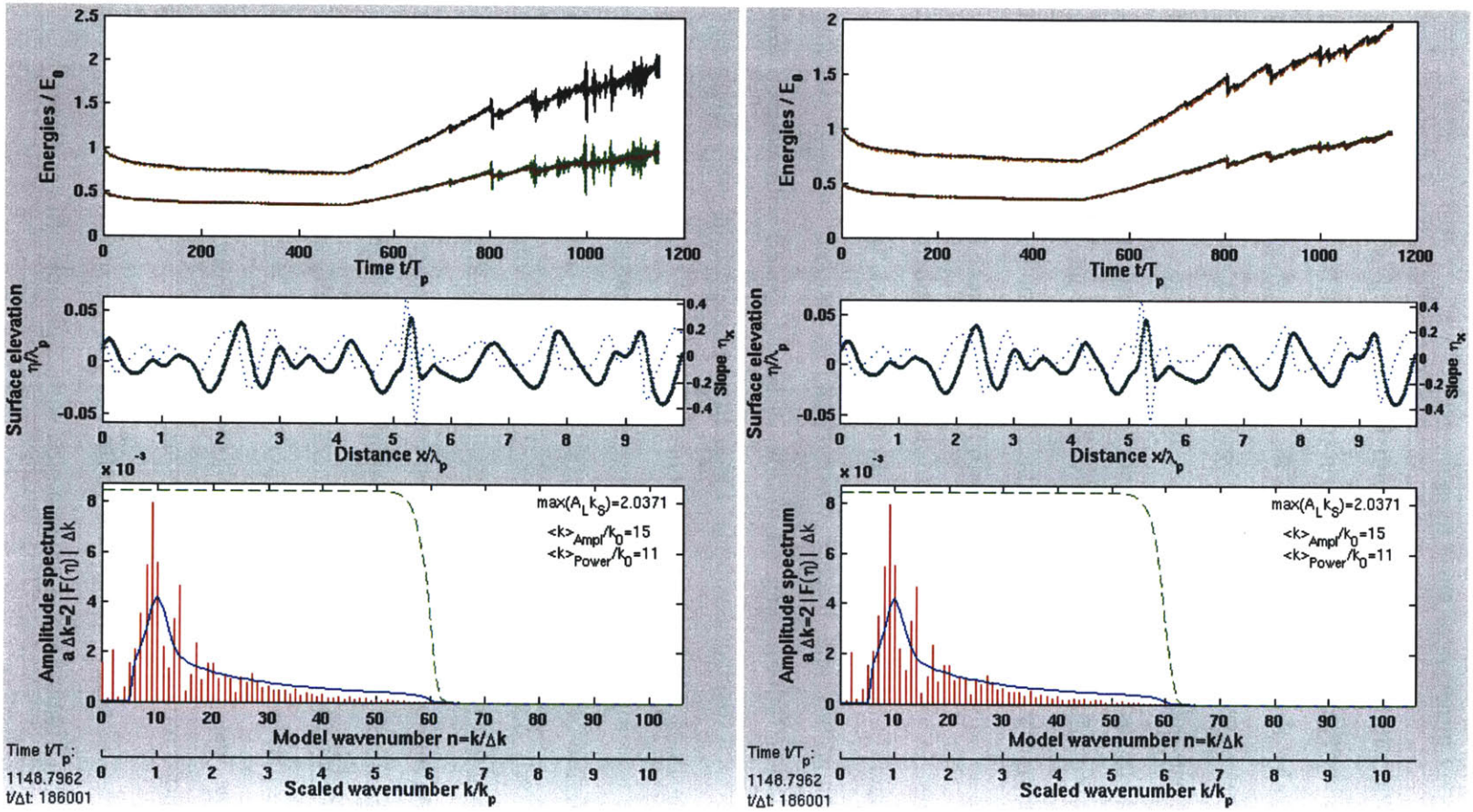

Figure 4.17 Left panel – no mean term removed, right panel – mean term removed. Top panel – energies: kinetic (green), potential (brown), total nonlinear (black) and total linear (brown dashed). Middle panel - surface elevation (green), local slope (blue dashed). Bottom panel - amplitude spectrum (red stem), initial amplitude spectrum (blue), breaking filter (green), diagnostic parameters in right corner: maximal cross scale steepness, amplitude weighted mean wavenumber, power weighted mean wavenumber. Time $1150T_p$.

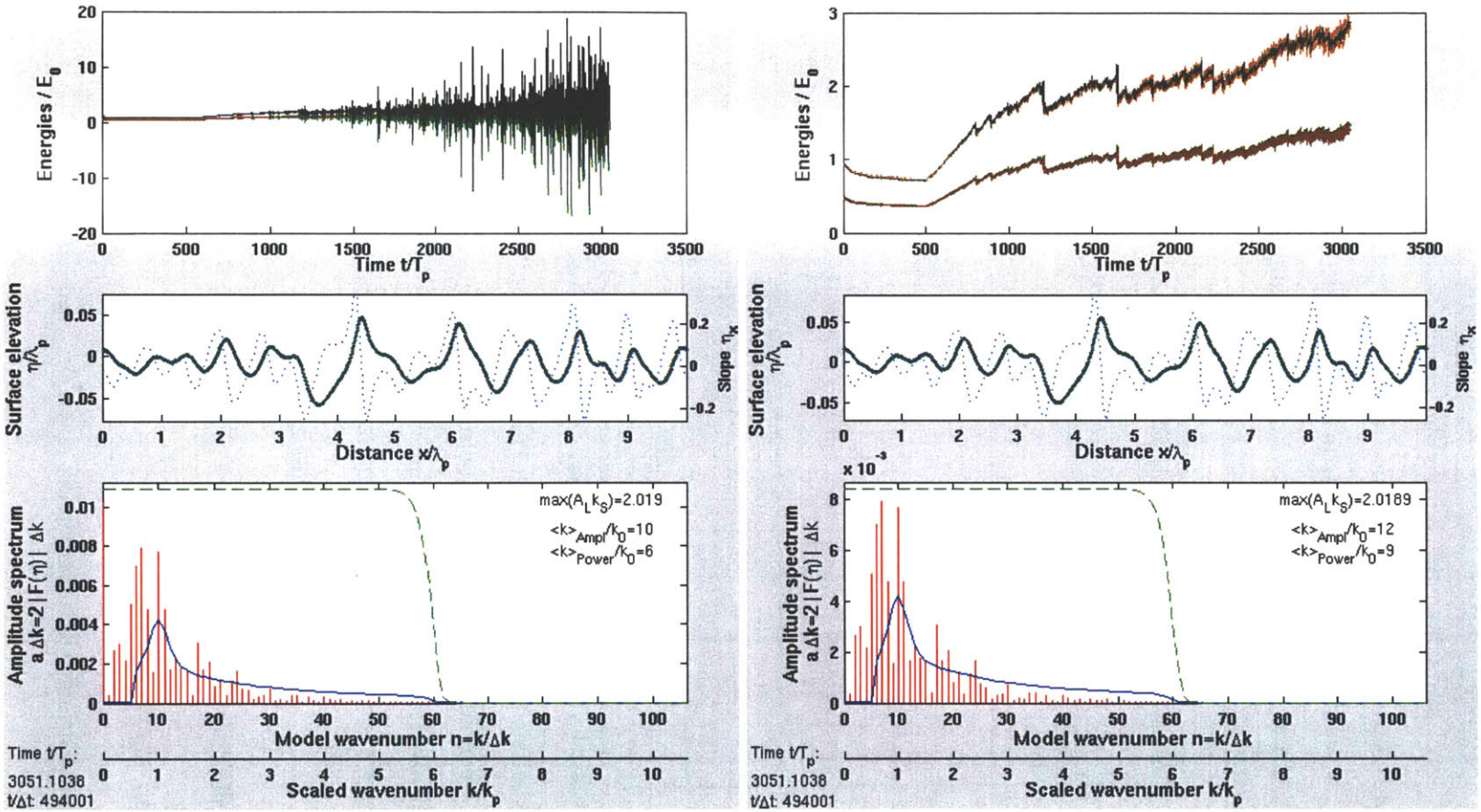

Figure 4.18 Same as Figure 4.17. Time 3050 T_p.

containing spectral components, $O(10^{-4})$ after 3000 T_p. Spurious volume losses are maintained at 10^{-14} level throughout the simulation, not explicitly shown in the figures. Although the above figures showed no difference in other simulated properties except for the kinetic energy, a highly detailed comparison of amplitude evolution (Figure 4.19) shows that removal of the mean component does modify the simulation. The difference, however, is completely negligible in the examined time scales.

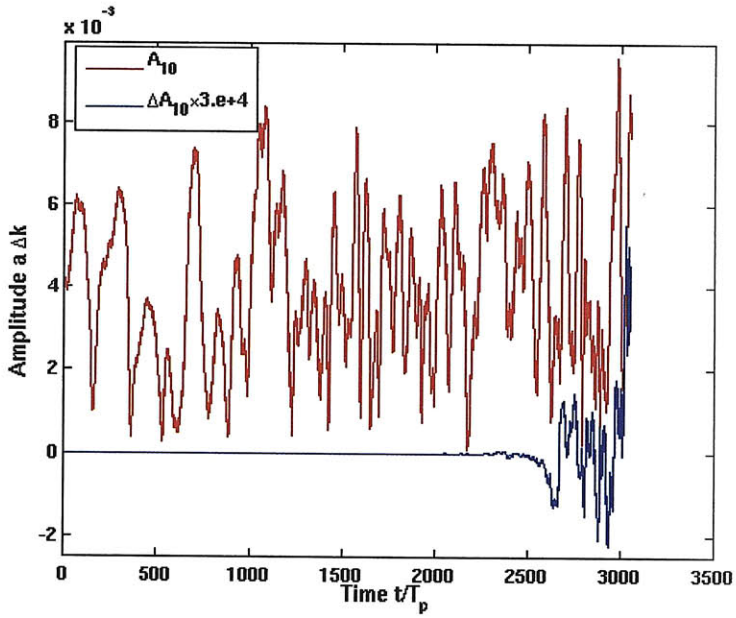

Figure 4.19 Amplitude of the peak harmonic without mean term filtering (red), difference between filterd and non-filtered peak harmonics multiplied by 3.e+4 (blue). Difference is observable after 2500 T_p.

The presented simulations were initialized with Donelan et al. (1985) spectrum for wave age 10 with low wavenumber components below $k_p/2$ removed. This was done to minimize the initial low frequency spectral content in attempt to isolate the mean term from long wave part of the spectrum. The forcing level was fixed to

$$\frac{\alpha_* k_p}{g\rho_w} = 0.0004 \tag{4.3.4}$$

The computational parameters chosen

$$M = 3, \quad R_{ph} = \frac{\lambda_p}{\Delta x} = 102.4, \quad R_{sp} = \frac{k_p}{\Delta k} = 10, \quad R_{time} = \frac{T_p}{\Delta t} = 161.9 \tag{4.3.5}$$

Wave breaking filter was rigid with parameters $[\beta_{scale}, \beta_{power}]$=[6,40].

4.3.5. Comparing phase resolving simulations of free and wind forced irregular waves

To demonstrate the developed phase resolving simulation method for irregular ocean wind waves in stage of strong coupling with the wind, we compare wind forced and wind free simulations starting from identical initial conditions describing young windsea of wave age 10 based on Donelan et al. (1985) parameterization. The objective is to elucidate the importance of wind forcing in phase resolving simulations of realistic wind waves in intermediate scale domains O(10km). The question rises because the observed growth rates are small $O(10^{-4})$, such that a typical wave of length 125m and period 9sec will grow only by O(5%) in amplitude as it propagates with group velocity O(7m/s) through domain of interest. How different phase resolved profile would be if simulated with and without wind forcing?

Figure 4.20 shows the output of both simulations after 10 T_p, before wind forcing was applied, so that both panels are identical. The bottom plot displays the discrete amplitude spectrum (red stems) vs. the initial amplitude spectrum (blue line), which was generated by discretization of Donelan et al. (1985) power spectrum in wavenumber domain and chopping the lowest $n_p/2$ sub-harmonics in addition to the high frequency modes removed by the low-pass filter (shown by green dashed line). Some diagnostic parameters are displayed in the right corner: the maximal cross scale term - $A_{long}k_{short}$, the amplitude weighted mean wavenumber and power weighted wavenumber. The middle panel shows the phase resolved elevation profile and its slope, calculated by forward Euler finite difference scheme. The top panel displays the total nonlinear wave energy (black) and the linear estimate – twice potential energy (brown dashed). The kinetic (green) and potential (brown) energies are plotted with artificial shift of 0.4 for graphical convenience. The near equipartition of energy is evident, the kinetic and potential energies deviate only O(1%) from each other. Their fluctuations are nearly in anti phase, leading to smooth evolution of the total nonlinear energy. The difference between the linear and nonlinear energy estimates is clearly displayed, consistent with the small deviation from equipartition.

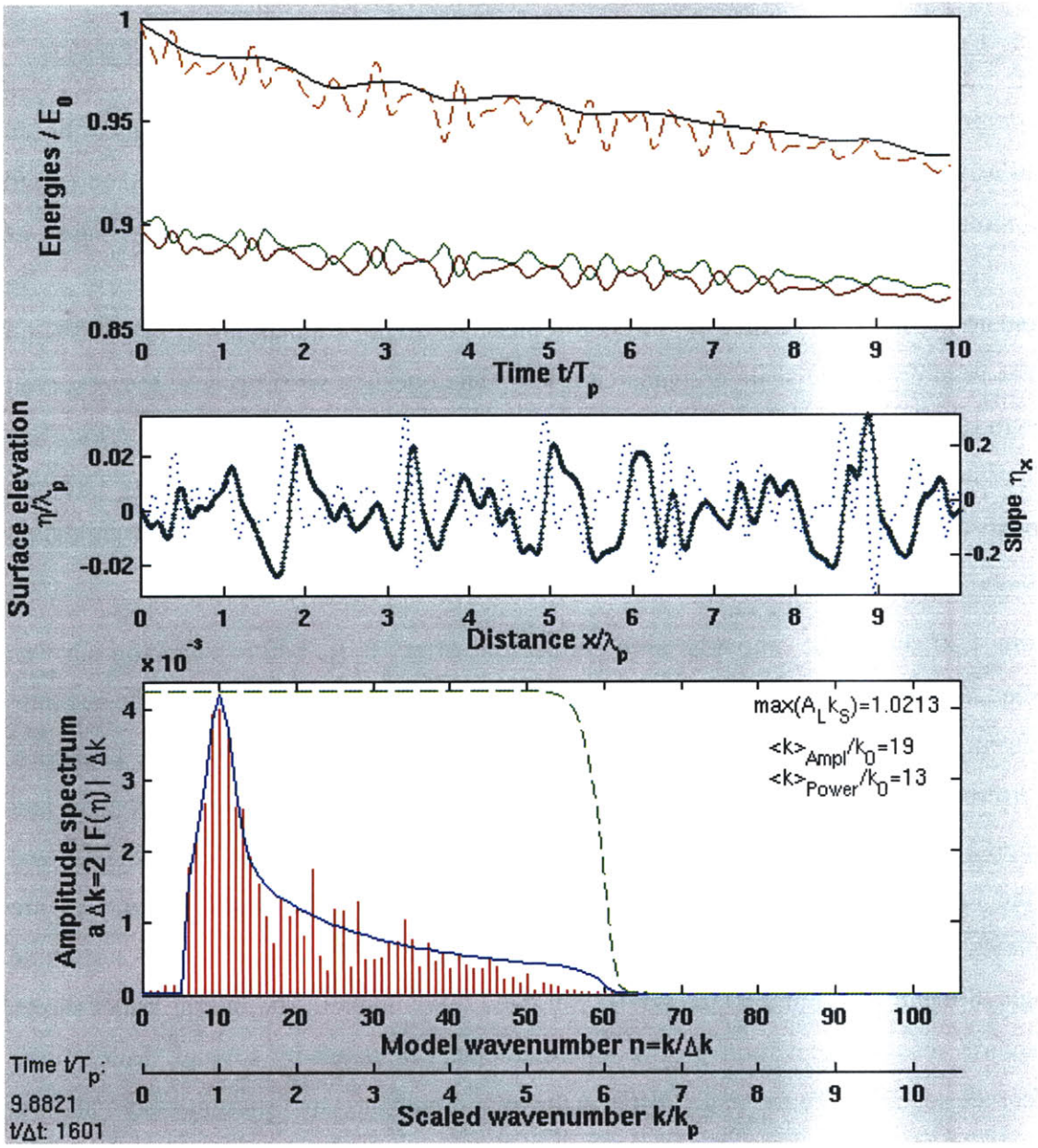

Figure 4.20 Same panels as in Figure 4.17. Time 10 T_p. Initial conditions and computational parameters as in Section 4.3.4.

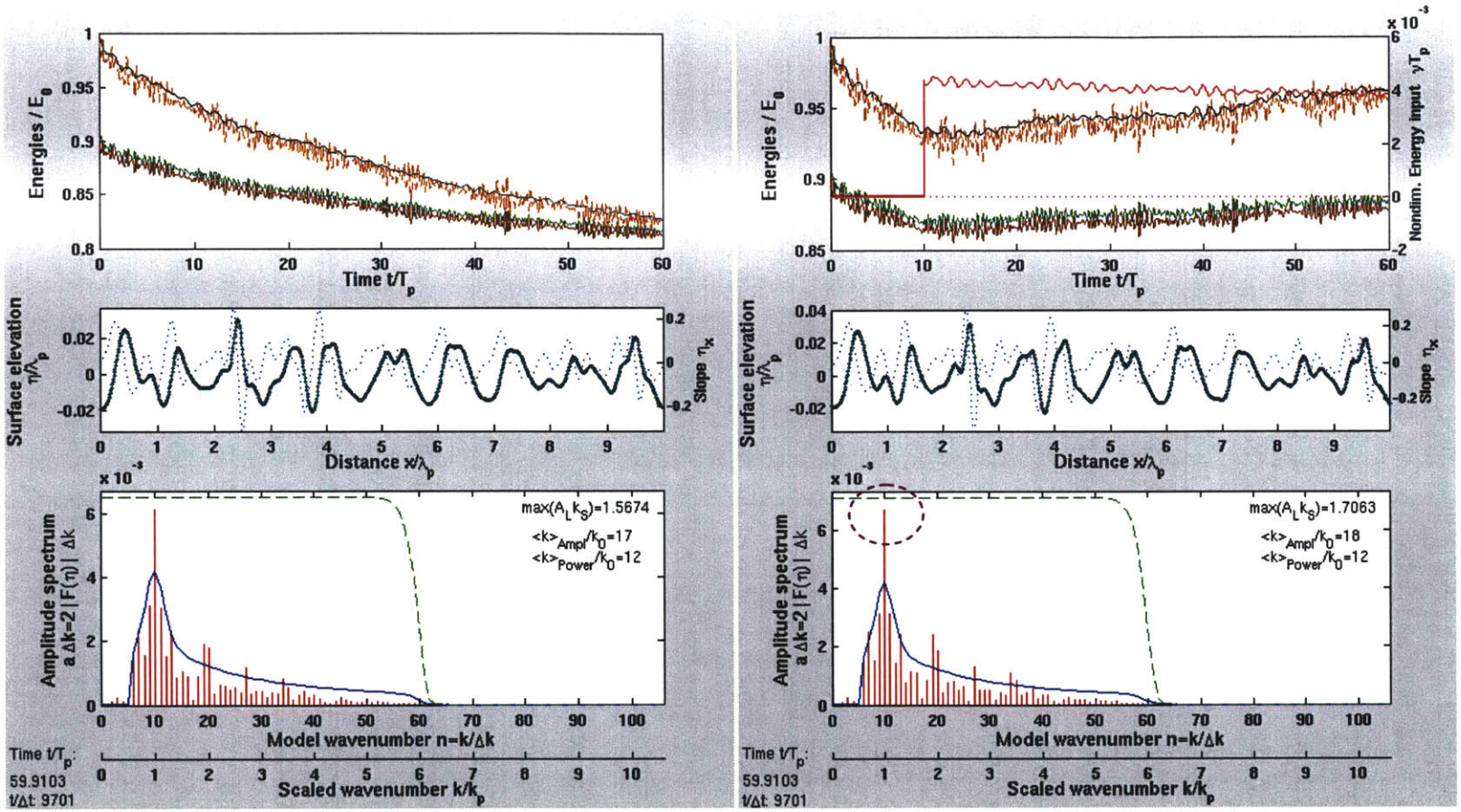

Figure 4.21 Left panel displays same information as Figure 4.20. Right panel shows in addition the nonlinear wind input (red line in top plot). Left panel – simulation without wind forcing, right panel – wind forcing is applied after 10 T_p. Both panels displayed at time 60 T_p.

Wind forcing is applied after 10 characteristic periods. 50 Tp later, Figure 4.21, the first differences between wind free and wind forced simulations can be discussed. The original peak component grows faster under wind forcing, although most of its growth is clearly due to the nonlinear interactions as captured by both simulations. The nonlinear energy grows smoothly while wind free energy continues to drop under dissipating action of wave breaking filter. Phase resolved surface profile shows no difference between two simulations.

As seen in Figure 4.22, O(150Tp) after wind was applied the system evolved to state of recurrent modulation. This is evident by the vanishing amplitude of the spectral peak, while its sidebands grew above their initial values. This modulation is noticeable in both simulations although some difference is clear – under wind forcing the upper sidebands grow faster, which is consistent with the linear theory predicting faster response to wind forcing of the shorter waves. Energy growth continued but seems to have reached a plateau characterized by some undulatory bursts. The profile of surface elevation has clearly different features on the right side of the domain, although demonstrating overall qualitative similarity. This is roughly the scale of the difference predicted by our analysis for 100 m long wave propagating through 10 km domain.

After 500 characteristic periods, Figure 4.23, the simulations evolved to different states. The spectrum and elevation profiles are different. The energy of wind forced wave system is twice of that of wind free wave. This is evident even in the local slopes of the surface, which are O(0.2) for growing wave and O(0.1) for free wave. Energy history of the growing wave shows few intermittent breaking events, the strongest one at 360 Tp lasts for O(10 Tp). It can be noticed, that this breaking event of the growing wave corresponds to significant wave breaking of the free wave at 340 Tp. Another simultaneous breaking event occurs at 150 Tp in both simulations. This consistency suggests that even that phase resolved details of these simulations are quite different after long enough evolution, some internal dynamical properties may remain similar for some longer time even is not visible by the direct phase resolving observation.

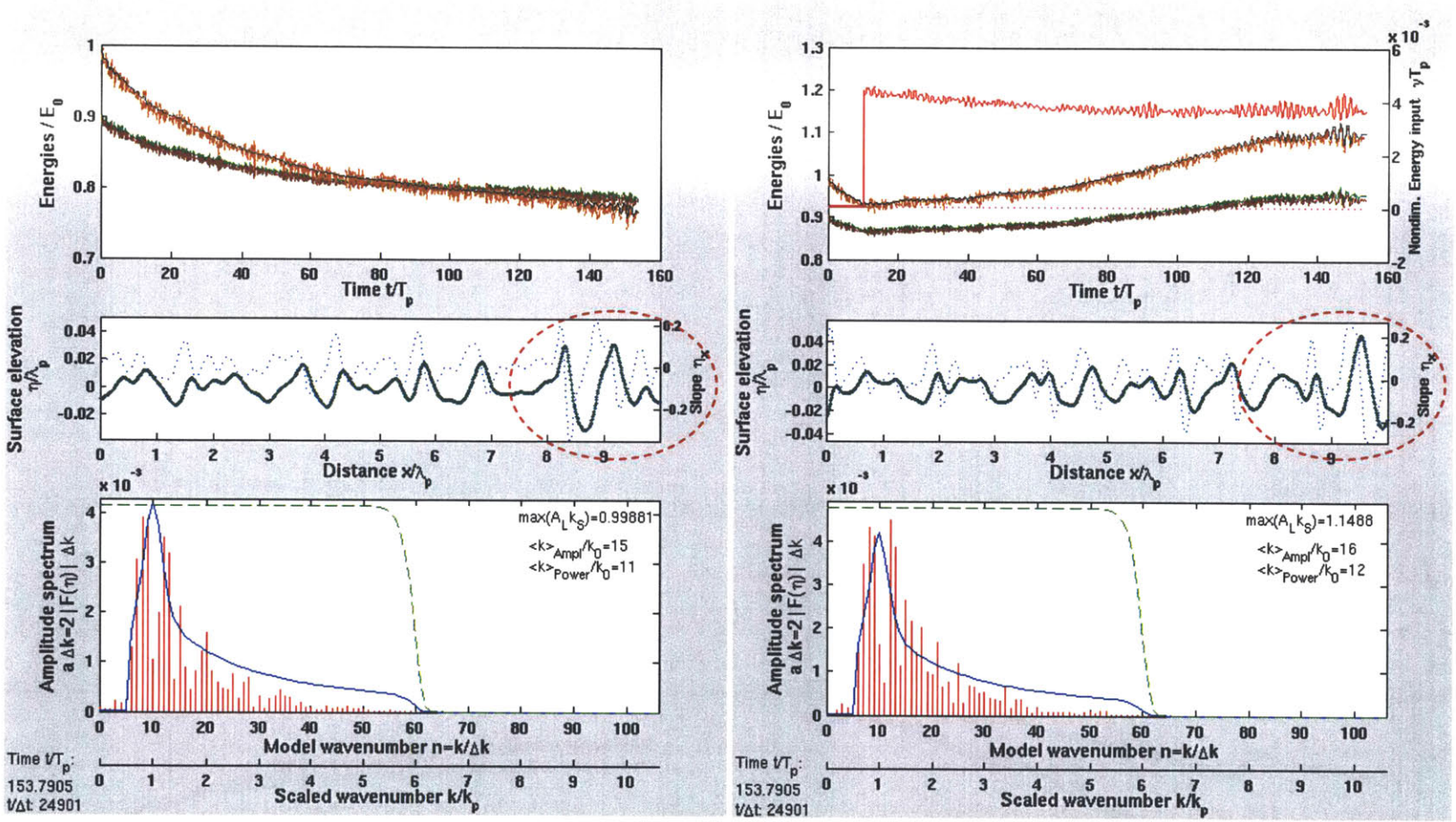

Figure 4.22 Same as Figure 4.21. Time 150 T_p.

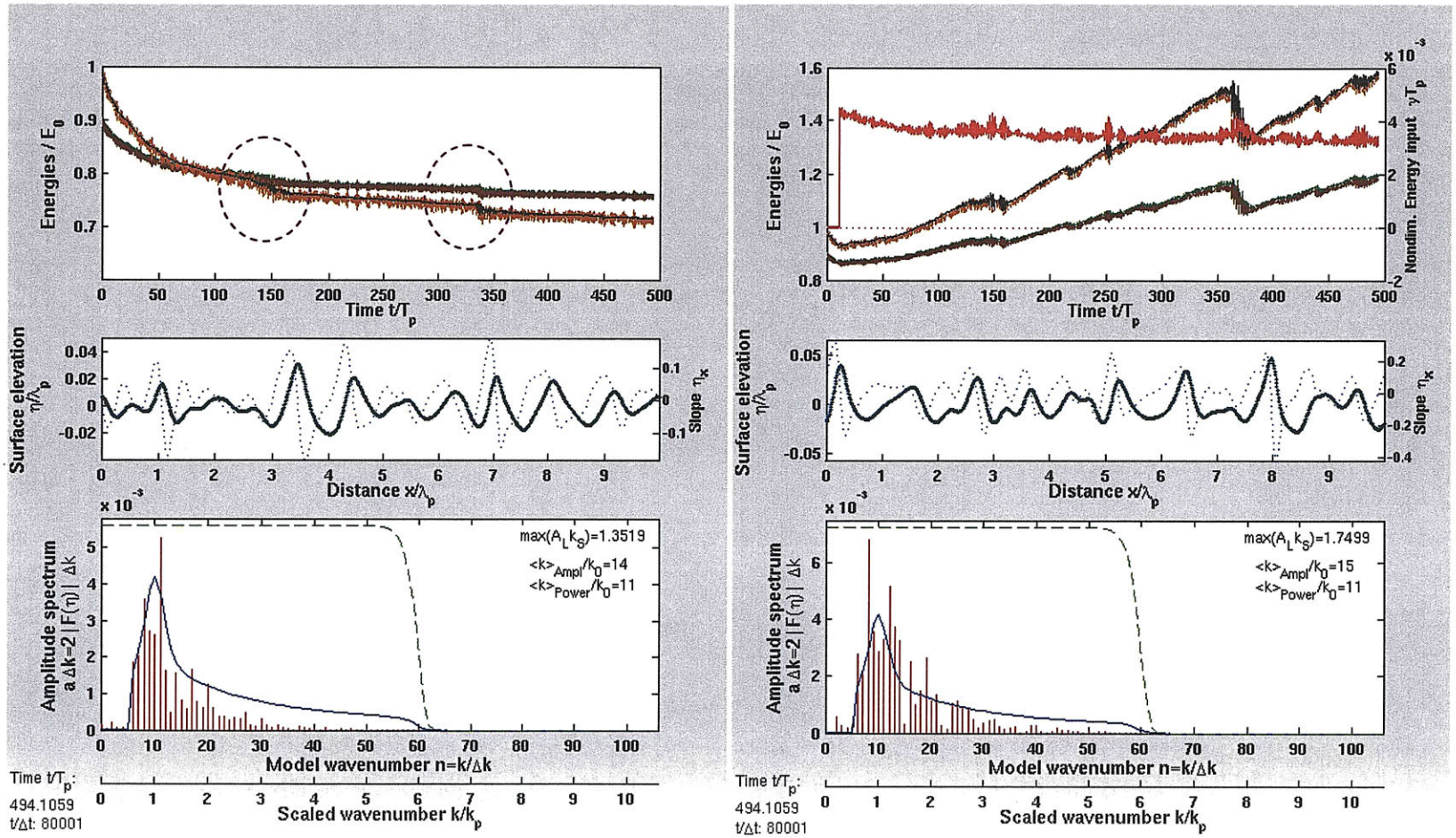

Figure 4.23 Same as Figure 4.21. Time 500 T_p.

Evolution of amplitudes of 5 spectral components near the original spectral peak are shown in Figure 4.24. Since at $O(150\ Tp)$ both simulations seem to have evolved to modulated state of sideband instability induced recurrence, we expect to observe a pattern resembling of Fermi-Pasta-Ulam recurrence. We see, however, that for broadband simulations it is hard to quantify the difference between the two nonlinear simulations. Peak of modulation is still noticeable at 150 Tp in both simulations as the amplitude of the peak component (red) reaches its minimum value. Another qualitative observation to be made is that under wind forcing the oscillations of amplitudes are qualitatively rougher.

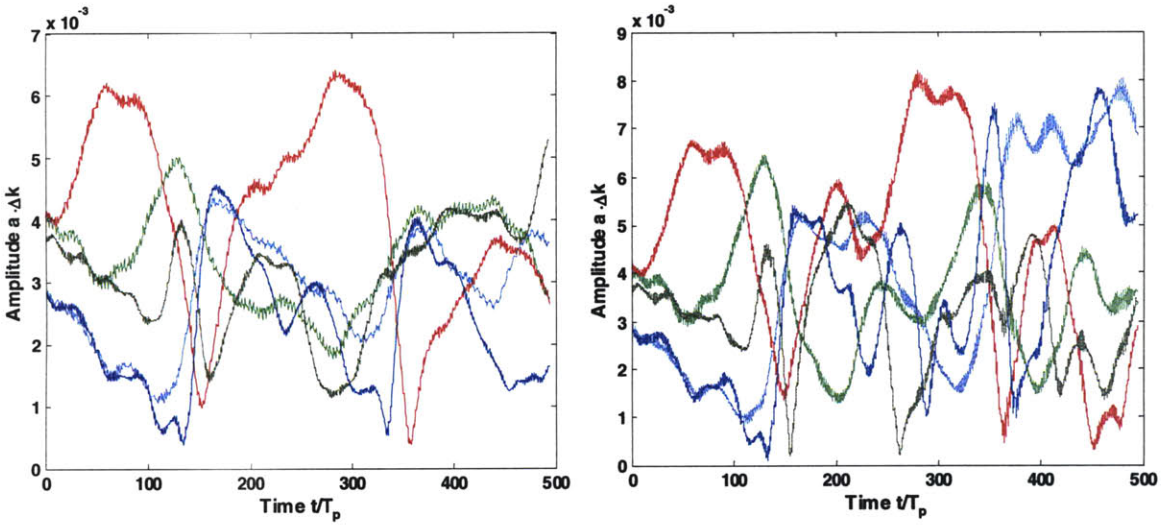

Figure 4.24 Amplitudes of dominant spectral components: peak harmonic (red), 2 upper and 2 lower sidebands.

4.4. *Verification of observed parameterizations and laws*

4.4.1. Duration limited evolution

Simulation of irregular wind wave field in periodic domain under steady homogeneous wind forcing corresponds to the idealized configuration of duration limited growth. In Figure 4.25 simulated duration limited growth is compared to the experimental estimates obtained in Section 2.1.3. Energy growth and frequency downshift are parameterized in fetch limited configuration by Donelan et al. (1985). Fetch to duration conversion is based on "Shore protection manual" (CERC 1984).

Linear energy estimate is compared to the observed duration limited growth parameterization (2.1.14) and to the exponential growth curve with the simulated forcing level

$$\exp\left(\frac{\alpha_* k_p}{g\rho_w}\omega_p t\right). \tag{4.4.1}$$

The exponential growth, which strictly applies to one linear monochromatic wave, appears to match closely the total broadband energy growth before the onset of the intermittent wave breaking. As wave field grows and evolves to certain saturation it starts breaking intermittently and part of energy supplied by the wind is lost making the overall growth rate slower, which corresponds to the duration limited growth. These two different growth laws demonstrate the difference between the fast time scale of exponential response to wind forcing, which appears to correspond to linear instability mechanism (Miles 1957), and the slower time scale of empirical laws of windsea evolution.

In the second plot the simulated wavenumber downshift, expressed by the power weighted average wavenumber, is compared to the observed estimate (2.1.14). After initial upshift period, which is correlated with the initial smooth instability growth, wave breaking begins to remove energy from the higher frequency part of the spectrum leading to intermittent downshift.

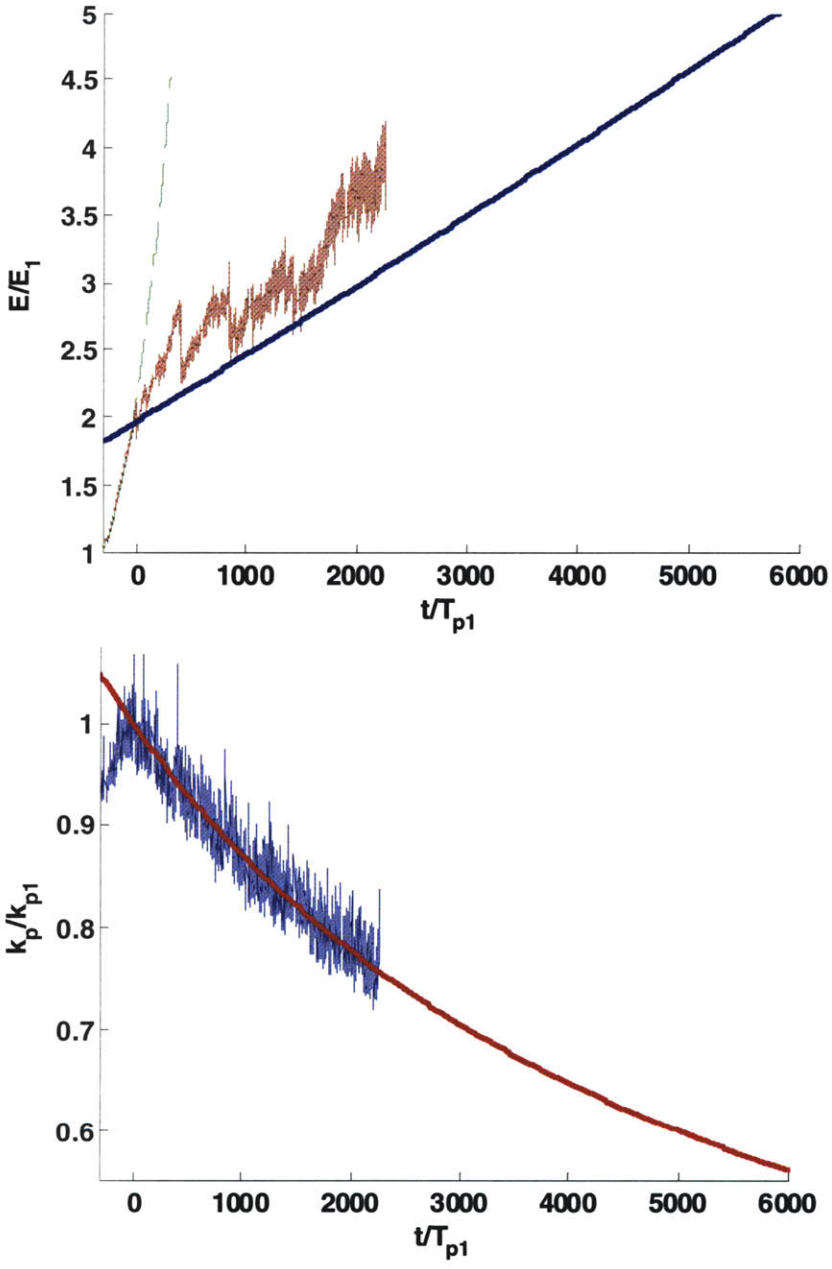

Figure 4.25 Upper plot – simulated energy growth (brown), exponential growth corresponding to the forcing level (green dashed), power law growth corresponding to duration limited growth. Lower plot – simulated wavenumber downshift (blue), duration limited parameterization (red). Time line is shifted to such that time zero corresponds to beginning of duration limited evolution.

4.4.2. Toba 3/2 law

Linear theories of wind forced growth by slope coherent pressure predict exponential growth of wave amplitude and steepness. Observations, however, show that for irregular wind waves steepness doesn't increase with the growing amplitude, but decreases in accordance with Toba 3/2 law. Toba empirical law (1972, 1978, 1997), see Section 2.1.5. , expresses growth of pure wind waves, i.e. actively growing windsea free of swell, by a power relation between wave energy and characteristic period

$$E \propto T_p^3 \propto \lambda_p^{3/2} \tag{4.4.2}$$

Equivalently, in terms of elevation variance or significant wave height the form of the law is

$$H_s \propto T_p^{3/2} \propto \lambda_p^{3/4} \tag{4.4.3}$$

Thus, growing windsea grows both in height and length as it evolves, which is not explained by linear instability theories of wind wave generation (e.g Miles 1957). Toba explains this deviation from linearity by hypothesis of a local quasi-equilibrium of waves with wind, where a nonlinear self-adjustment mechanism governs the balanced growth.

The hypothesized nonlinear quasi-equilibrium of growing windsea is simulated with our simple linear model of wind forcing and highly simplified model of wave breaking. With properly resolved nonlinear wave-wave interactions, this approach appears to suffice for simulation of realistic wavefields satisfying Toba law. The simulations clarify the nonlinear mechanism of irregular wavefield response to wind forcing, showing a gradual transition from wind free swell to the growing quasi-equilibrium of windsea. The key process governing the transition appears to be onset of intermittent wave breaking of much higher frequency and strength compared to the mild breaking of swells. The exponential growth, predicted by the linear theory, is confirmed for the broadband wavefield at the transient state of weak wave breaking. Toba's hypothesized nonlinear self-adjustment mechanism is explained by nonlinear wave-wave interactions in dynamical balance with energy supply by wind and energy loss by wave breaking.

The above understanding is established by ensemble of simulations initialized with Donelan et al. (1985) spectrum of wave age 10. Correspondingly the forcing level is fixed to 0.0004, see Section 2.2.3. Rigid wave breaking filter was applied with parameters $[\beta_{scale}, \beta_{power}]=[6,40]$. Simulation results are shown in Figures 4.23 to 4.28. Lower right plots show the simulated discrete amplitude spectrum vs. the initial spectrum. Smoothed continuous representation of the spectra appears in lower left plots. The smoothing method is a non-periodic running average over half spectral resolution, i.e. $n_p/2$, which was chosen arbitrarily to standardize comparison between different spectral resolutions. It is evident that averaging conceals distinct features of the discrete spectra, but is necessary for concise graphical presentation, especially when spectral resolution is high. Both, simulated and model scaled wavenumbers are shown in the lower axis of the spectra for convenience of visualization of the discretization effect. Wave breaking filter curve is outlined over the spectra, arbitrarily scaled by maximum of each plotted spectrum.

Left panel shows the nonlinear estimate of wind energy input. No wind work is done in first 500 periods. Wind forcing is applied at 500 T_p and kept constant throughout the simulation. The nonlinear wind input fluctuates around mean trend of gradual decrease. The fluctuations diminish with increased spectral resolution, suggesting convergence if the model. The gradual decrease of wind work is the effect of the nonlinear broadband response of the wavefield, in other words it is the actual rate of wind energy extraction by all the spectral components combined. The forcing level, which is the expected exponential nondimensional growth rate of a single mode, is set to 0.0004 in this simulation. Each of the individual components induces energy flux from the wind with this rate. However, due to nonlinear interactions the effective growth of each component is different. The nonlinear interactions modify the rate at which wind energy is absorbed by the waves. Thus, our numerical model allows estimation of the nonlinear response of waves to wind forcing. The nonlinear work is the rate at which energy is extracted by the wavefield. The rate of energy absorption is this work minus the energy lost to the intermittent wave breaking. We note that, during the transient state of fast exponential energy growth all the energy extracted from the wind by the waves is absorbed. At the

intermittent quasi-equilibrium, however, although the wavefield extracts similar amount of energy from the wind, it does not absorb it all and intermittently grows with slower rate. The transition from the linear stage to the nonlinear quasi-equilibrium growth is associated with the gradual onset of the intermittent wave breaking.

The characteristic frequency, quantified by power averaged wavenumber (see Section 4.3.3.) and displayed on top of the growing energy in right panels, downshifts during the initial wind free propagation. The rate of downshift slows down as wavefield adjusts to the low-pass wave breaking filter. After wind forcing is applied, some upshift is observed in all simulations and is clearly associated with the smooth exponential growth. Since at this stage all the supplied wind energy is absorbed, the upshift can be understood (see Section 4.2.3.) by faster growth of the shorter components, which tilt the spectral average to the high frequency side. As the wavefield saturates and deviates from the exponential growth, the mean wavenumber stops increasing and gradually starts downshifting, what marks the transition to the stage of balanced duration limited growth. Fluctuations of the average wavenumber around its mean trend shrink with increased spectral resolution, suggesting spectral convergence. Occasional events of strong wave breaking during the equilibrium growth stage are accompanied by temporary upshifts, which may be explained as fast response to wind forcing. These short time response events appear dominated by the linear mechanism required for fast reconstruction of the spectral tail.

The growing energy is shown plotted versus the evolving period in upper left plots. The parametric plots graphically present wavefield evolution in Toba's parametric space. In first stage of the evolution, without wind forcing, energy drops a small fraction of its initial value and frequency downshifts quickly while the spectrum adjusts itself to the wave breaking filter. Then, when wind turns on, the energy starts to grow quickly, corresponding to the regular exponential growth predicted by the linear theory. The characteristic frequency estimate upshifts $O(5\%)$, corresponding to the saturation of the high frequency spectral range which responses faster to find forcing. The evolution appears to be cluttered by strong oscillations of the characteristic frequency, plotted

curves deviate from the general trend mainly in the horizontal direction. Nevertheless, it is visible how the growth curve transitions from the fast exponential growth to an equilibrium corresponding to Toba's similarity law and continues evolving, although with vigorous fluctuations, along curves of Toba similarity law and Donelan et al. (1985) "local" growth parameterization. The evolution continues for $O(1000)$ periods with local fluctuations being a significant fraction of the overall trend. These fluctuations significantly reduce with increasing spectral resolution, suggesting convergence in discretization of the spectra.

Parametric plots of significant steepness, upper right plots, show that all the simulations start at certain steepness. Then in "swell" stage of evolution the steepness drops down with fast energy loss and downshifting. During the smooth exponential growth the steepness quickly restores to its original level. The system transitions to Toba quasi-equilibrium and continues evolving as steepness gradually decays. The similarity of steepness evolution for all the simulations examined suggests its universality as the underlying physical mechanism, details of which invite further clarification.

Eventually simulations fail. The numerical crush appears to be related to large local steepness $O(1)$. Evolution towards the crush can be visualized on the parametric plots (Figure 4.32). The trace of the curve reveals that the process is gradual. It is accompanied by energy growth and upshift, which indicates that growth of shorter components dominates the spectrum. Thus, tracing wave system trajectory in Toba parametric domain may be a convenient tool for investigation of numerical details of simulation. This is in addition to the direct physical interpretation as Toba 3/2 law.

Different random phase realizations with different resolutions are shown in Figures 4.23 to 4.28. Same principal qualitative features appear in all the simulations. This may be interpreted as validation of consistency of our modeling approach and confirmation of our physical understanding.

T_{wind}=500T_p, np=10, Forcing level=0.0004

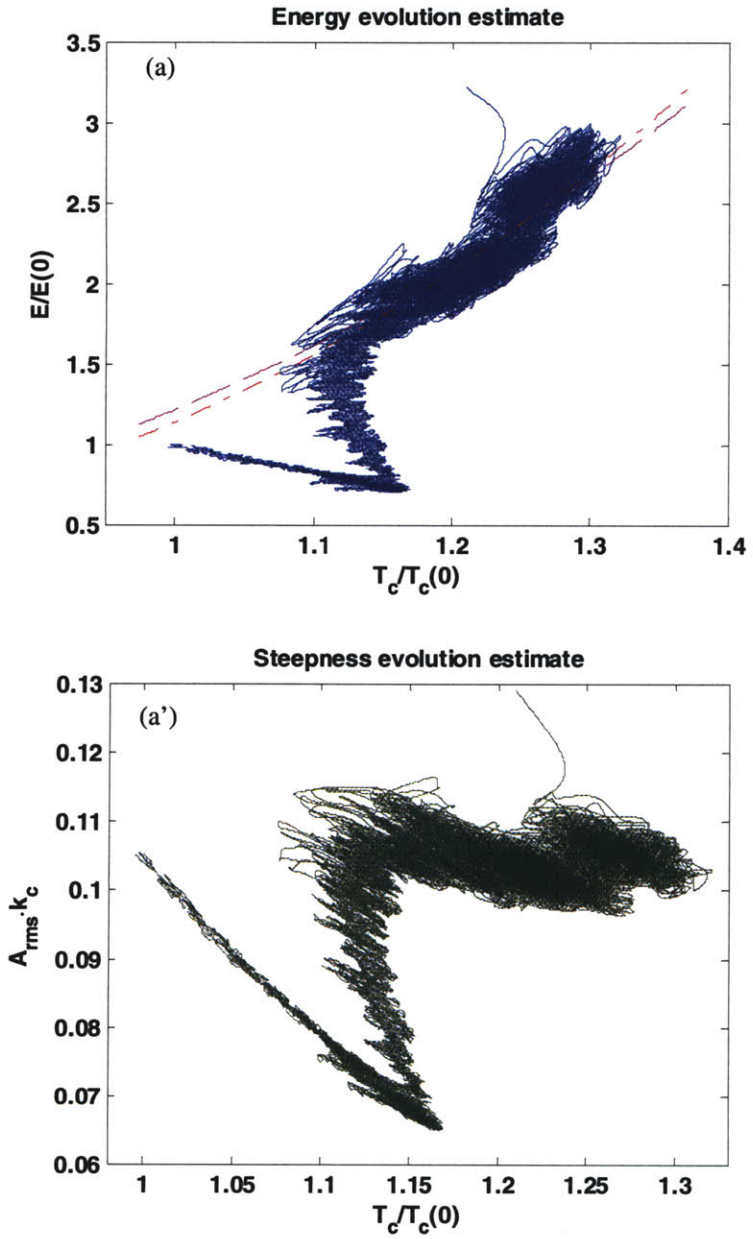

Figure 4.26 Output of simulation as described in the title on this page. Current page plots: (a) - Linear energy estimate vs. characteristic period, compared to Toba 3/2 law and Donelan et al. (1985) parameterization. (a') - Characteristic steepness vs. characteristic period.
Facing page plots: (b) - Linear (brown) and nonlinear (black) energy evolution, exponential growth (dashed cyan), nonlinear wind input (red). (b') - Energy growth as in (b) and power weighted average wavenumber downshift (blue). (c) – Surface elevation (dark green), significant wave height range (dashed gray). (c') Surface elevation (dark green) and local slope (dashed blue). (d) Averaged amplitude spectrum: initial (blue), at time indicated (dark green), breaking filter (dashed green). (d') Discrete amplitude spectrum (green stem), initial spectrum (blue line), breaking filter (dashed green). Time is indicated in left lower corner: number of characteristic periods t/T_p , number of time steps $t/\Delta t$.

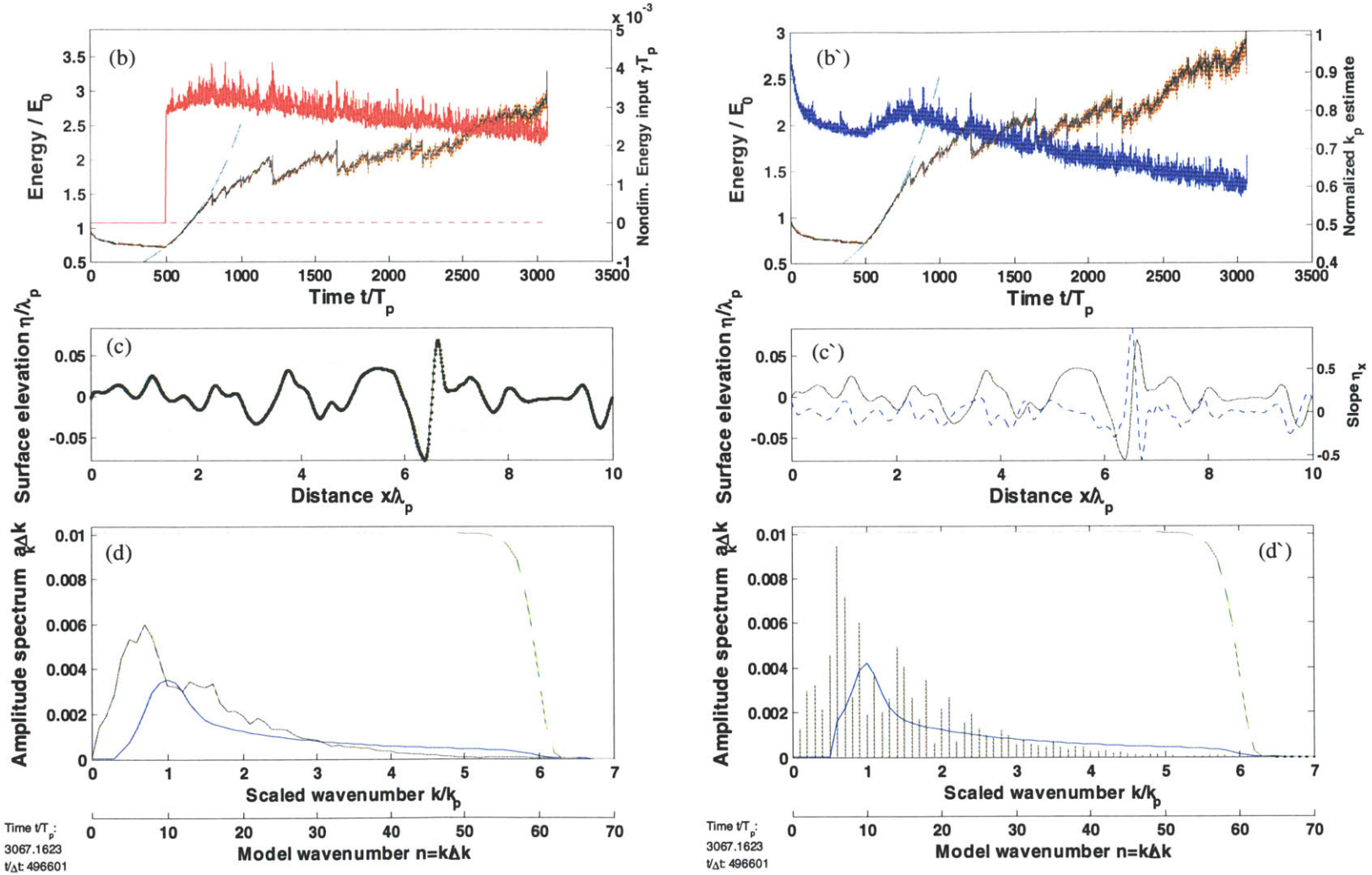

Figure 4.26 (b, b', c, c', d, d') For caption see facing page.

T_{wind}=500T_p, np=20 (random phase realization 1), Forcing level=0.0004

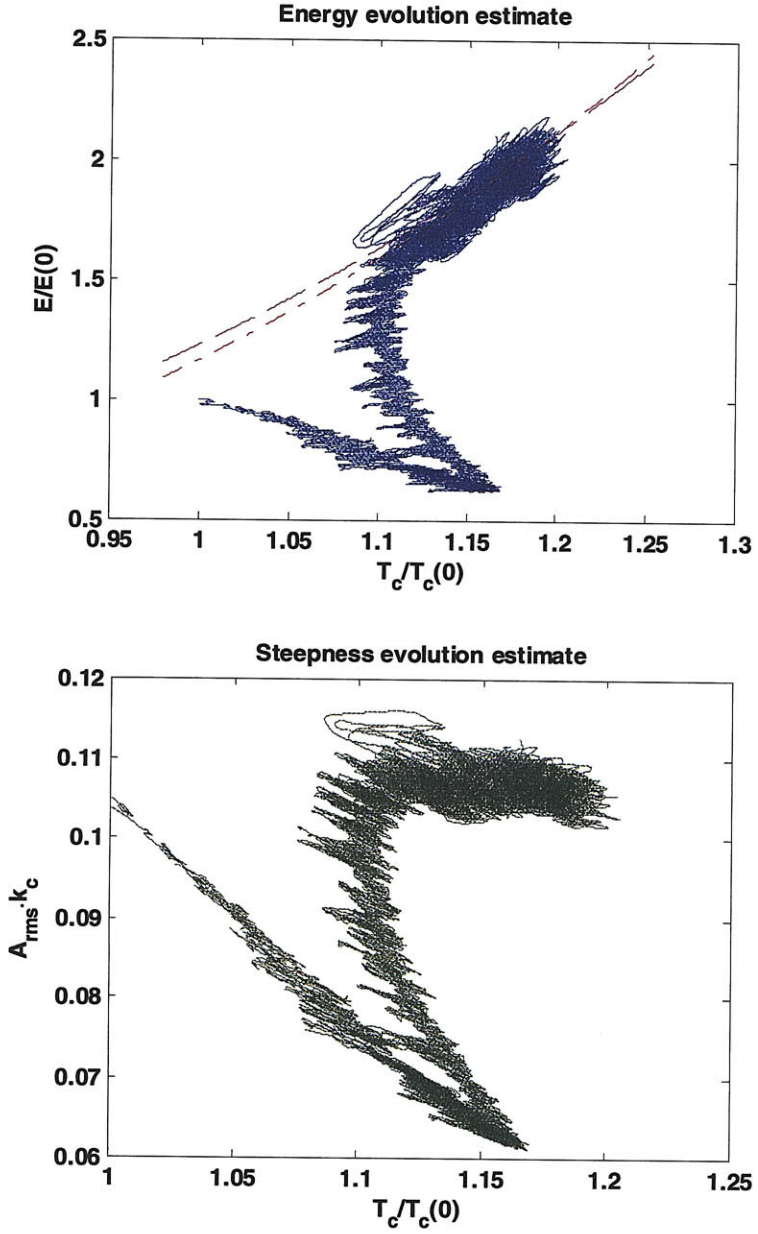

Figure 4.27 Same as Figure 4.26 for simulation described in the title.

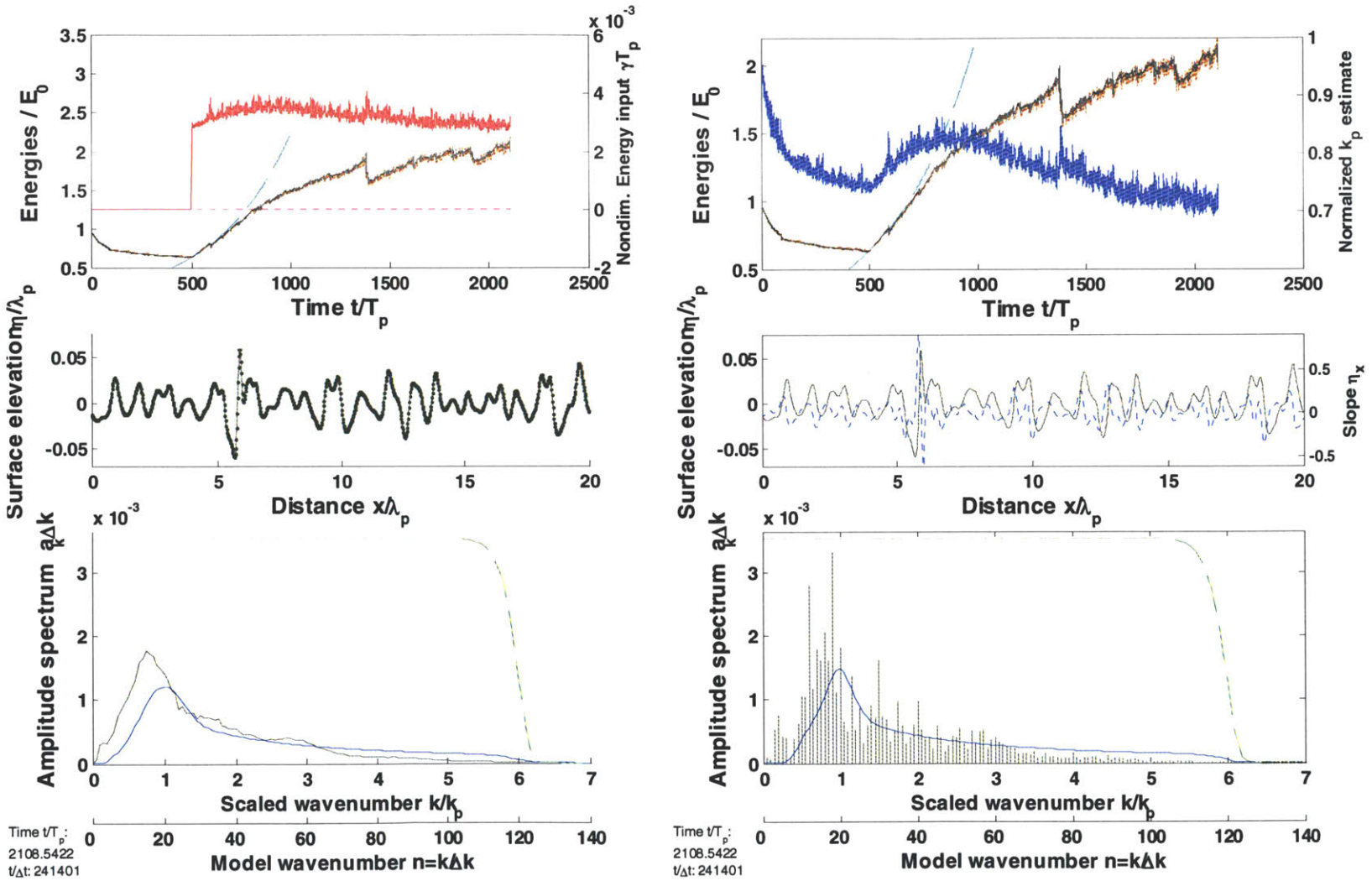

Figure 4.27 (b, b', c, c', d, d') For caption see facing page.

T_{wind}=500T_p, np=20 (random phase realization 2), Forcing level=0.0004

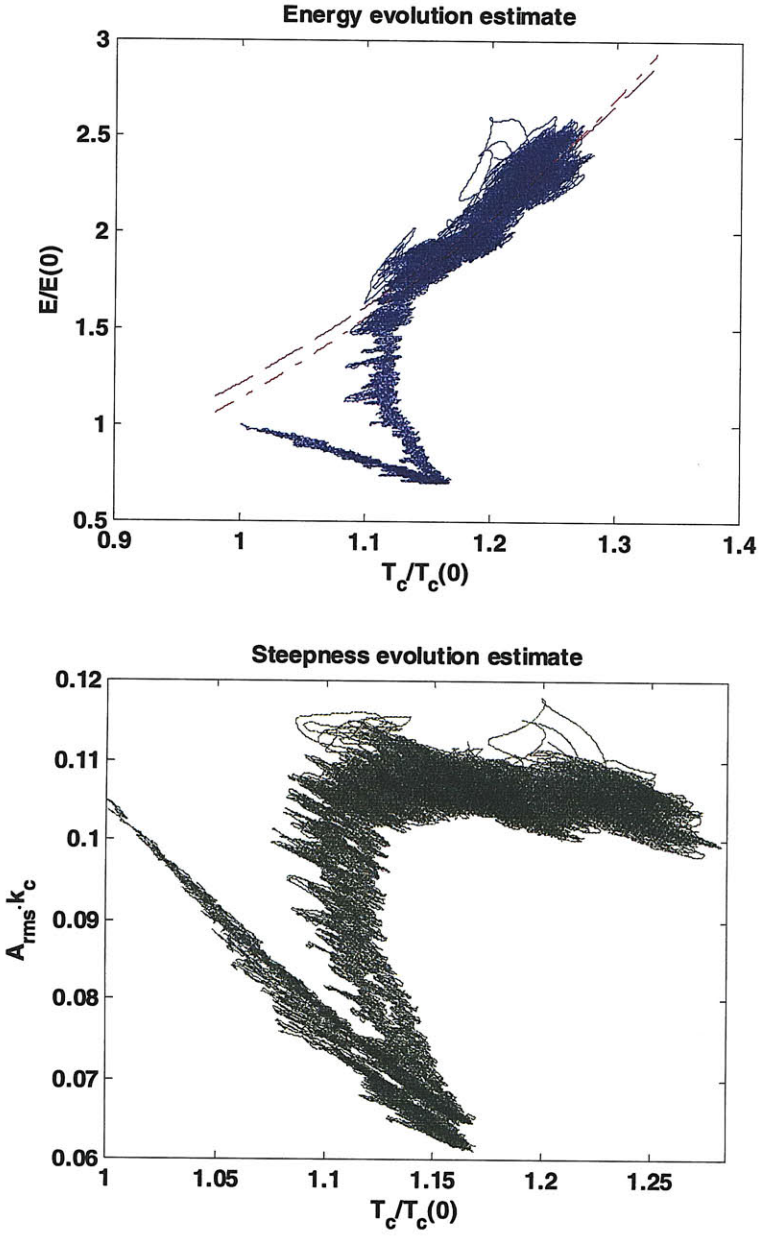

Figure 4.28 Same as Figure 4.26 for simulation described in the title.

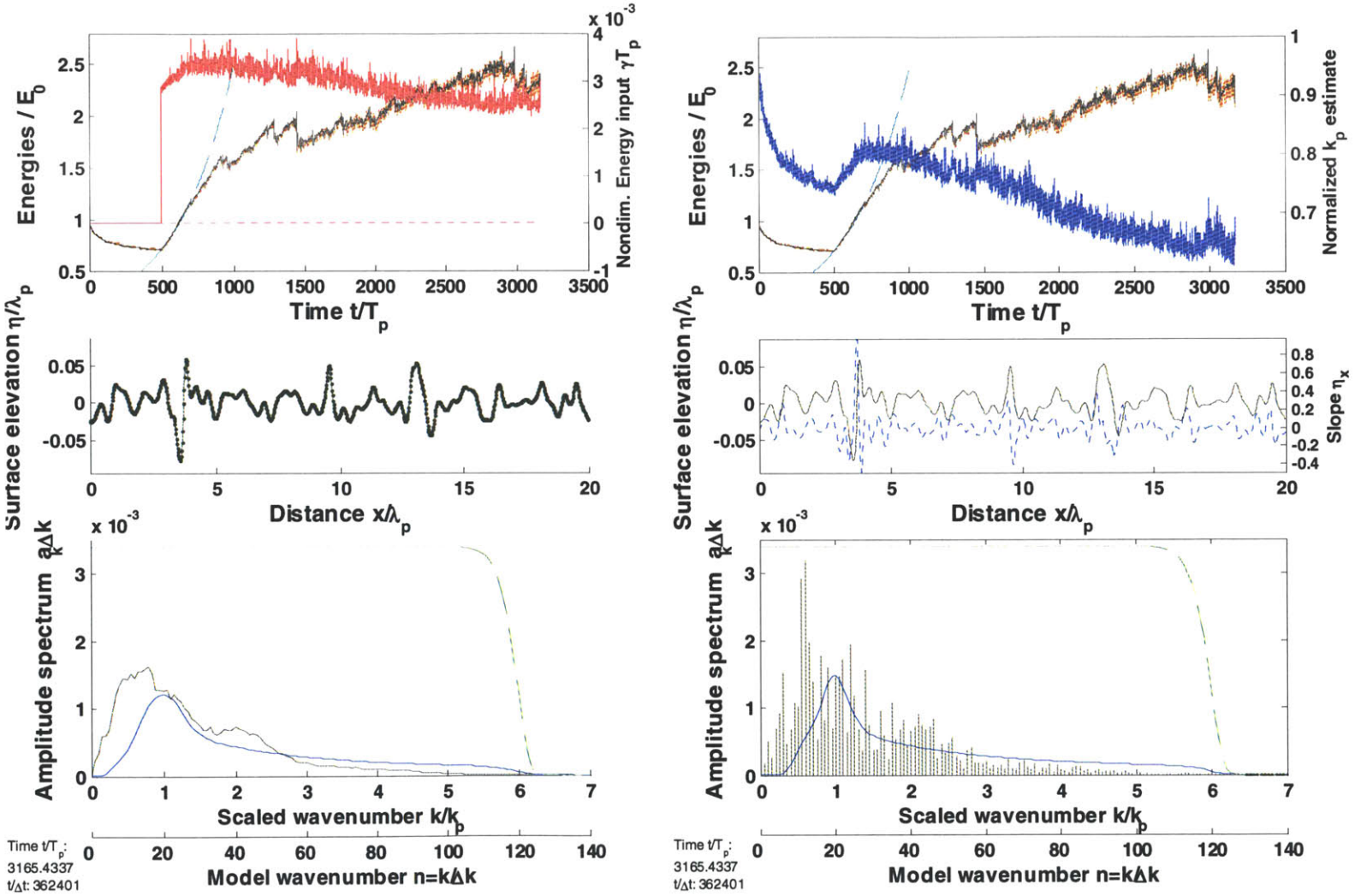

Figure 4.28 (b, b', c, c', d, d') For caption see facing page.

T_{wind}=500T_p, np=40, Forcing level=0.0004

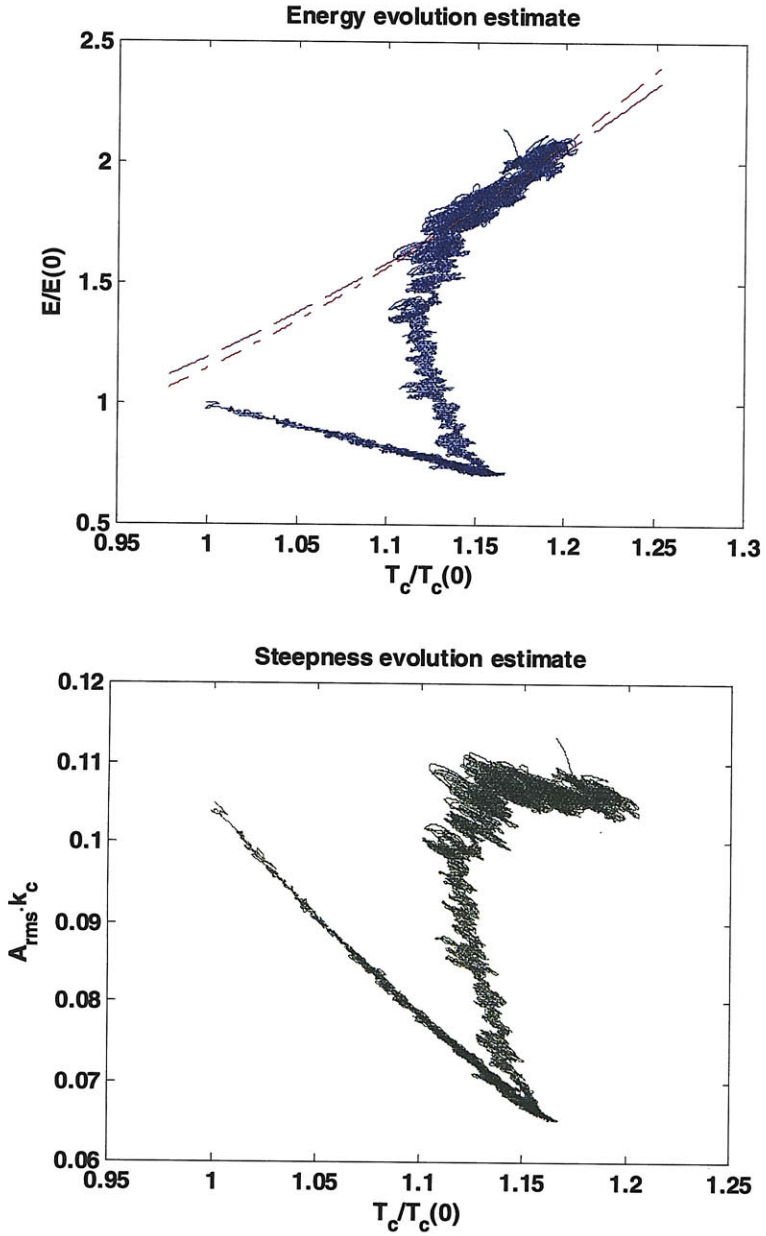

Figure 4.29 Same as Figure 4.26 for simulation described in the title.

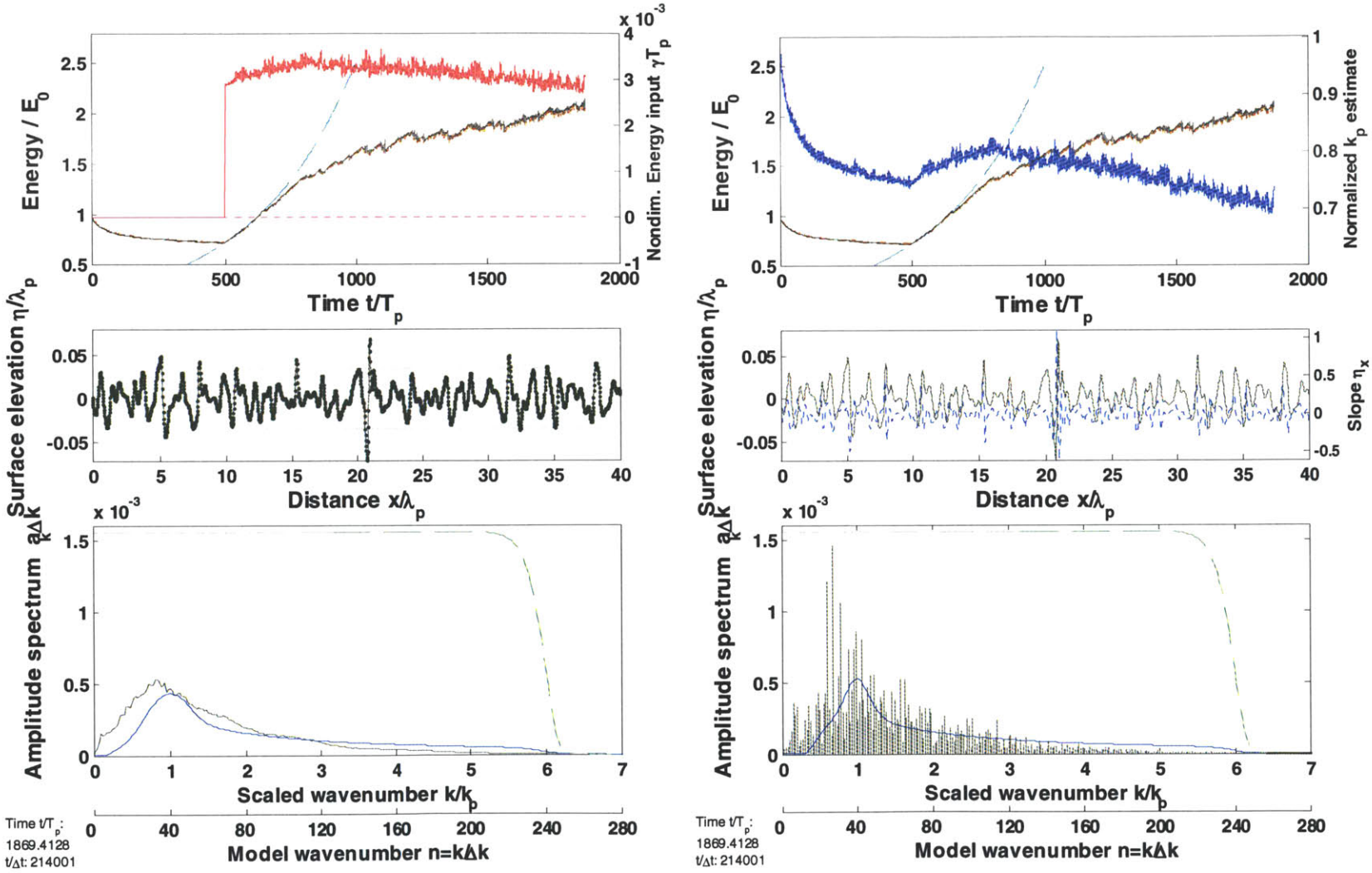

Figure 4.29 (b, b', c, c', d, d') For caption see facing page.

T_{wind}=500T_p, np=80, Forcing level=0.0004

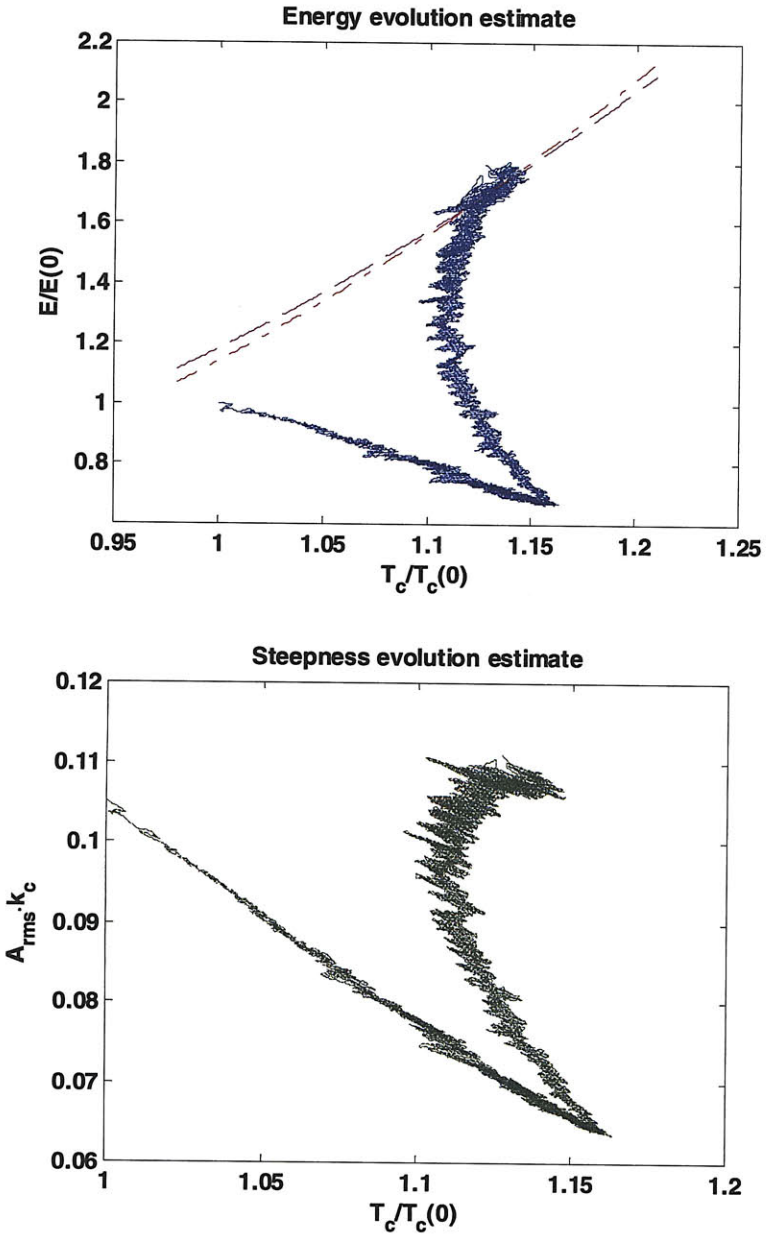

Figure 4.30 Same as Figure 4.26 for simulation described in the title.

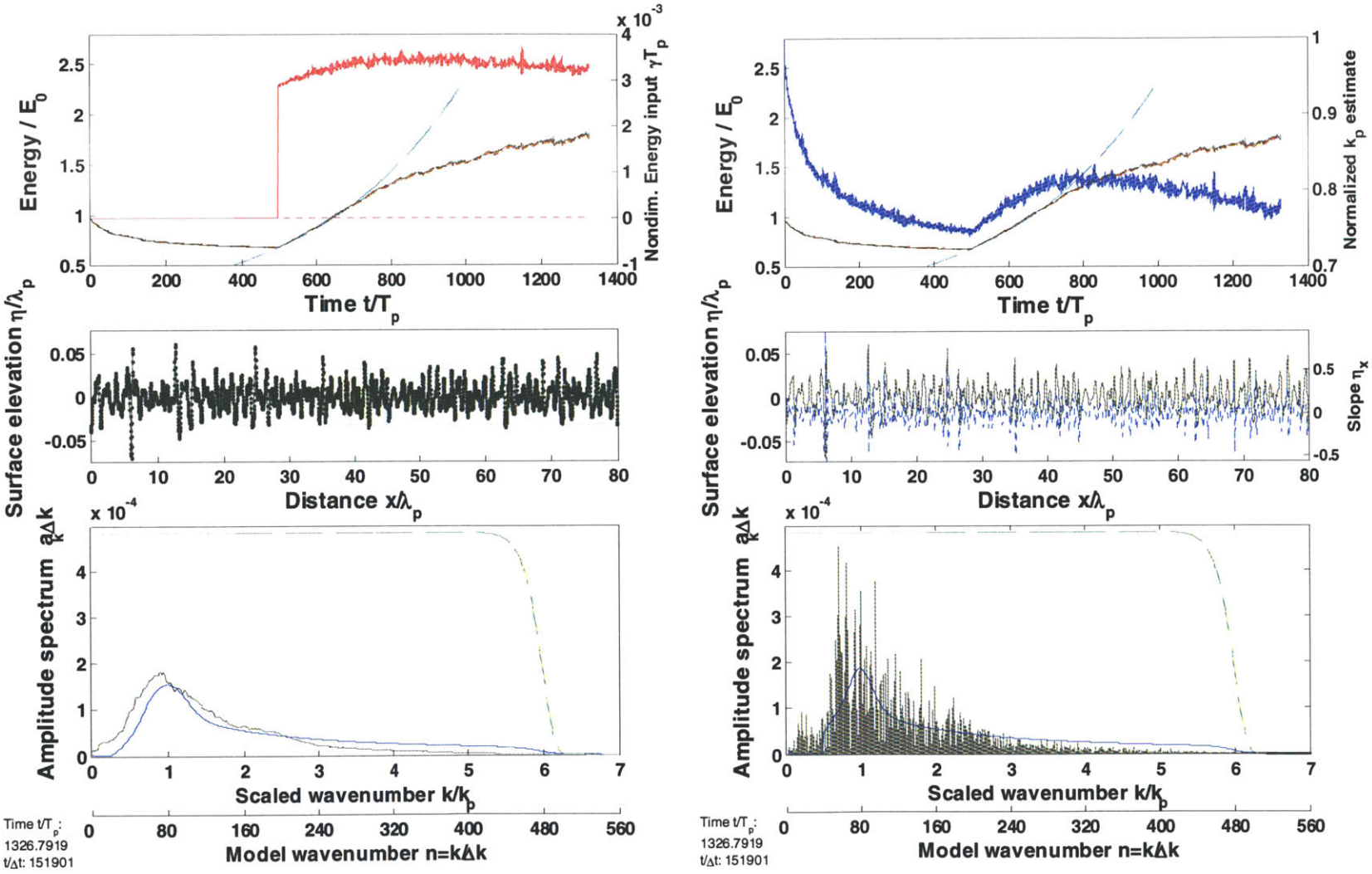

Figure 4.30 (b, b', c, c', d, d') For caption see facing page.

T_{wind}=500T_p, np=160, Forcing level=0.0004

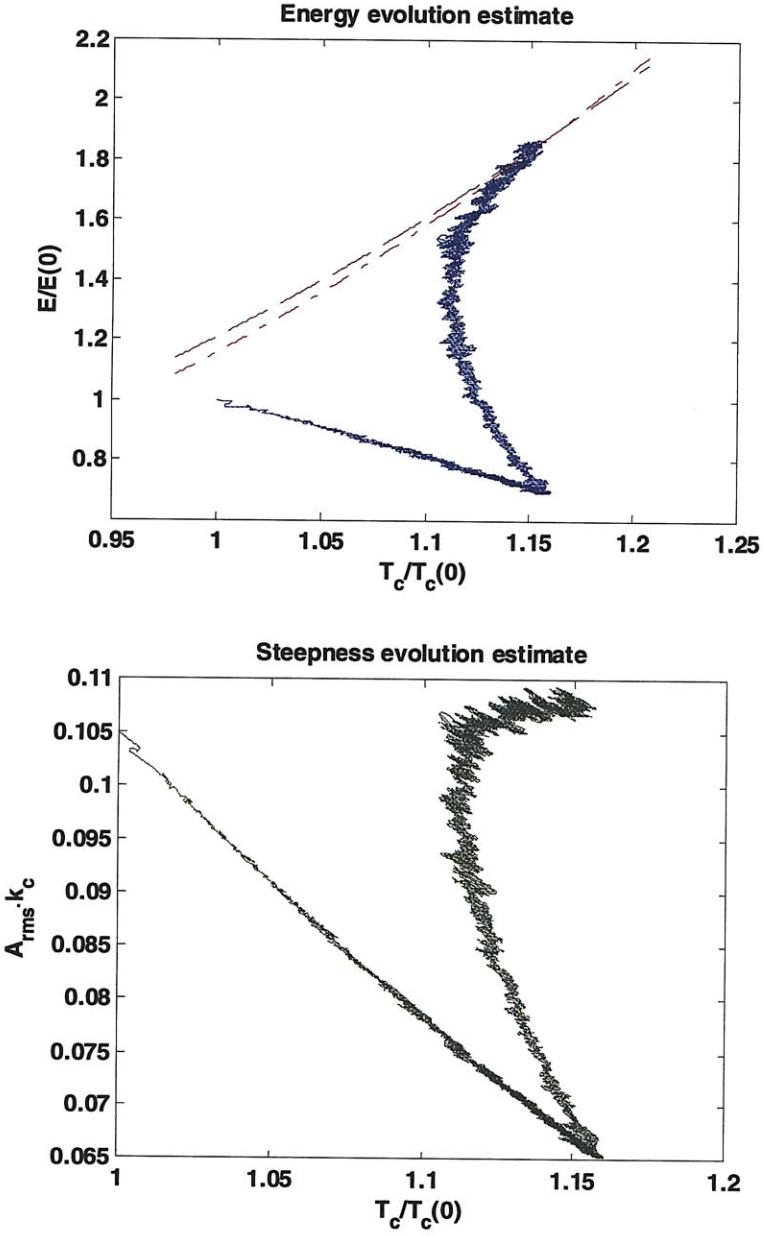

Figure 4.31 Same as Figure 4.26 for simulation described in the title.

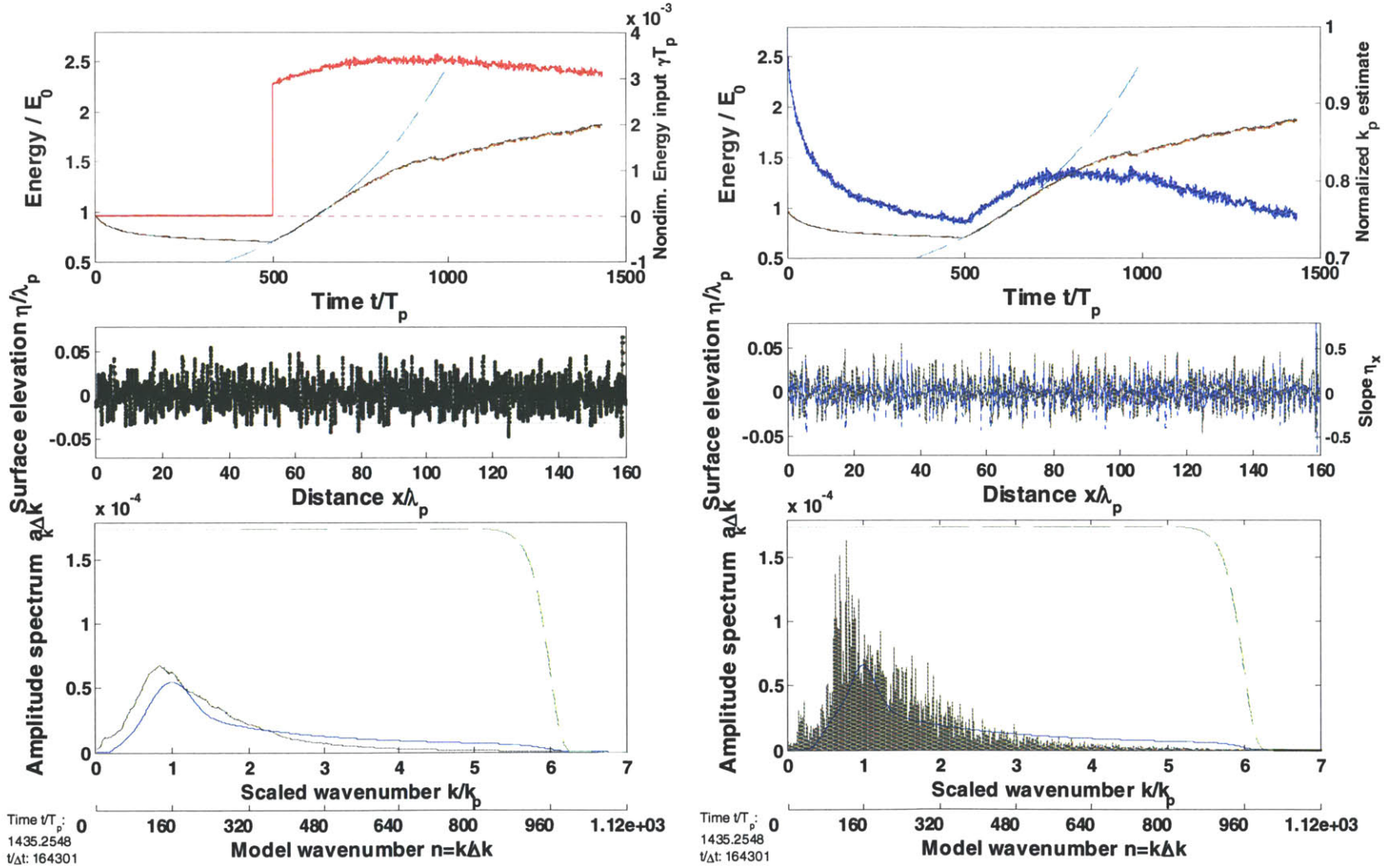

Figure 4.31 (b, b', c, c', d, d') For caption see facing page.

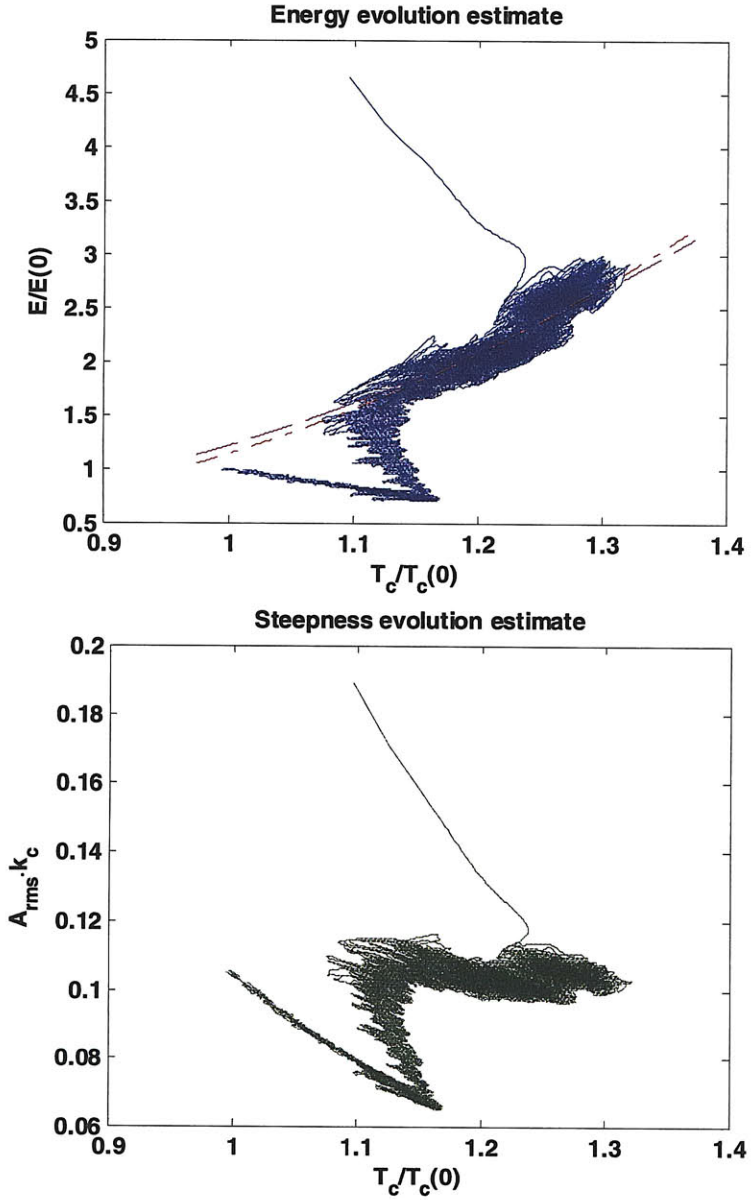

Figure 4.32 Same simulation as in Figure 4.26. Showing the same plots as (a) and (a`) in Figure 4.26 for longer simulation time. Displaying the gradual evolution to simulation crash.

The sensitivity of the results to the length of the initial adjustment period is examined in Figure 4.33 and Figure 4.34. Shorter swell simulations show that the reasonable agreement with Toba law obtained in all the simulations above, which had swell adjustment periods of 500 Tp, is not achieved with shorter adjustment times. The simulated macroscale evolution characteristics are different in both presented cases. The 200 Tp case does capture the initial exponential growth with the supplied forcing level, but does not strictly correspond to Toba 3/2 law in the equilibrium growth stage. Although downshift is correlated with intermittent growth, in Toba configuration space the growth is too fast or equivalently the downshift is too slow. The significant steepness is nearly constant during the downshifting stage and does not decrease as implied by Toba law. The 10 Tp case doesn't capture the regular exponential growth stage at all, the growth is slower than expected from the linear theory for the applied forcing level. Wave breaking seems to start influencing the dynamics right away by removing the energy supplied by the wind to the wave field. This does not allow the transient linear growth stage when all wind work is absorbed. There is no upshift stage and simulation breaks after 1000 periods, not allowing enough evolution time for confirmation of quasi-equilibrium adjustment. We conclude that simulation adjustment time cannot be neglected. The simulation cannot adjust to the unbalanced initial conditions under wind forcing, simultaneously with wind adjustment. Separate adjustment times have to be allowed.

$T_{wind}=200T_p$, np=20, Forcing level=0.0004

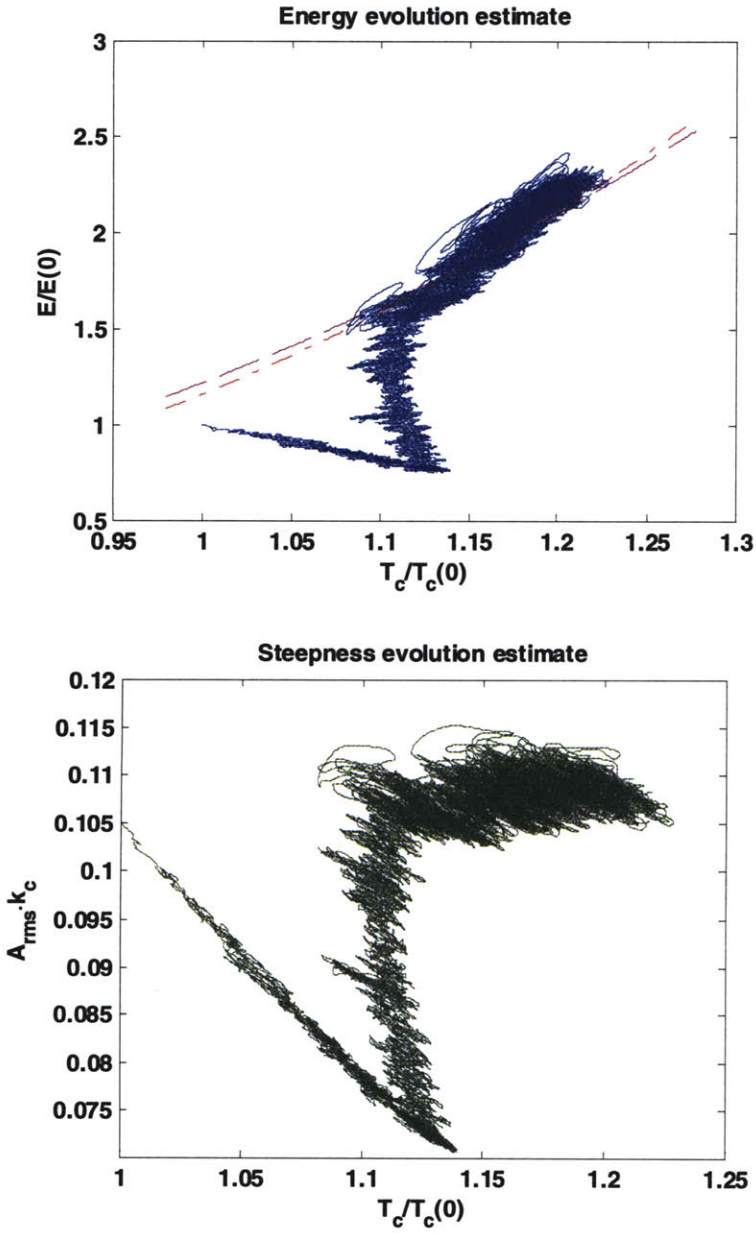

Figure 4.33 Same as Figure 4.26 for simulation described in the title.

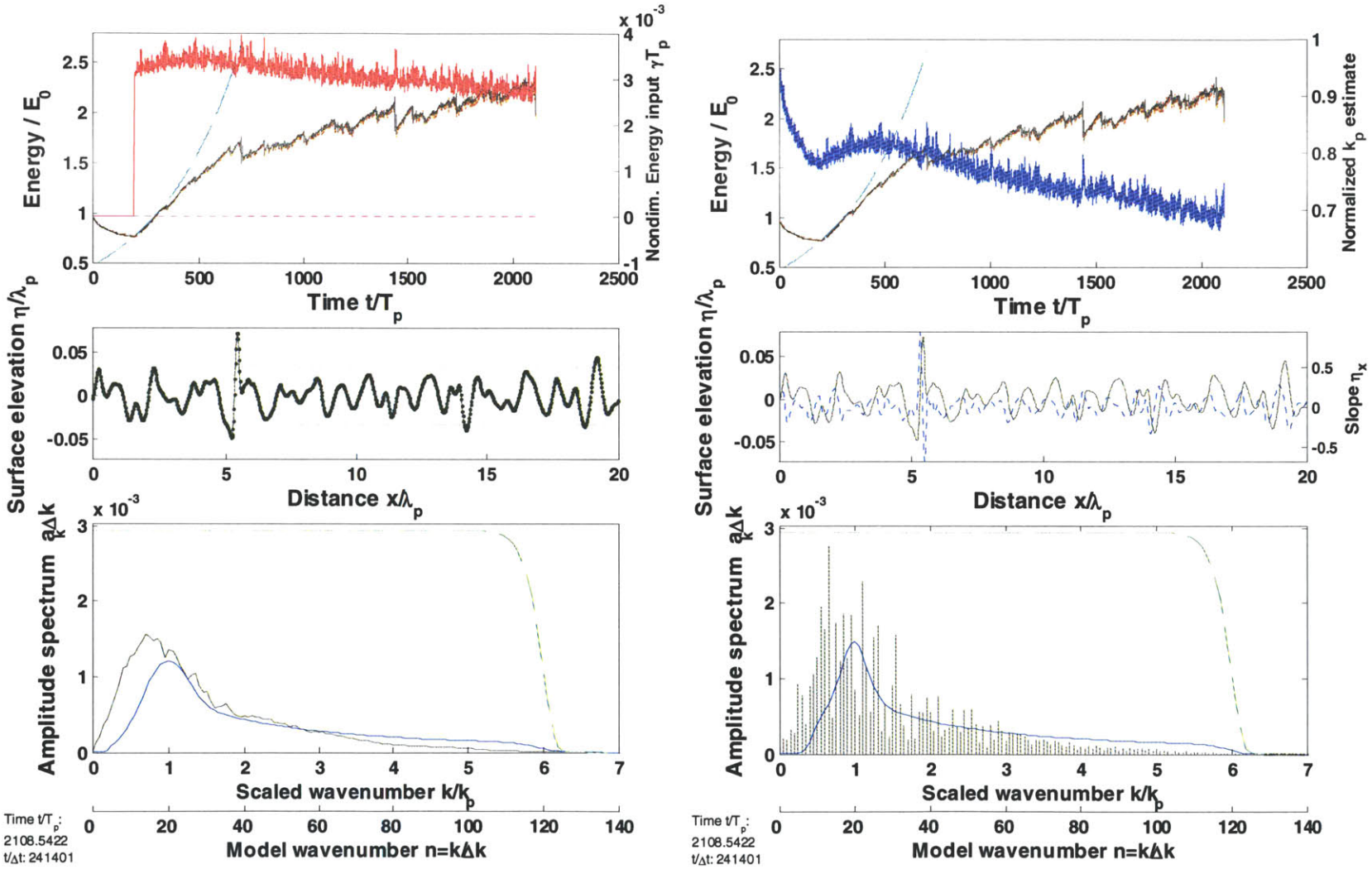

Figure 4.33 (b, b', c, c', d, d') For caption see facing page.

$T_{wind}=10T_p$, np=20, Forcing level=0.0004

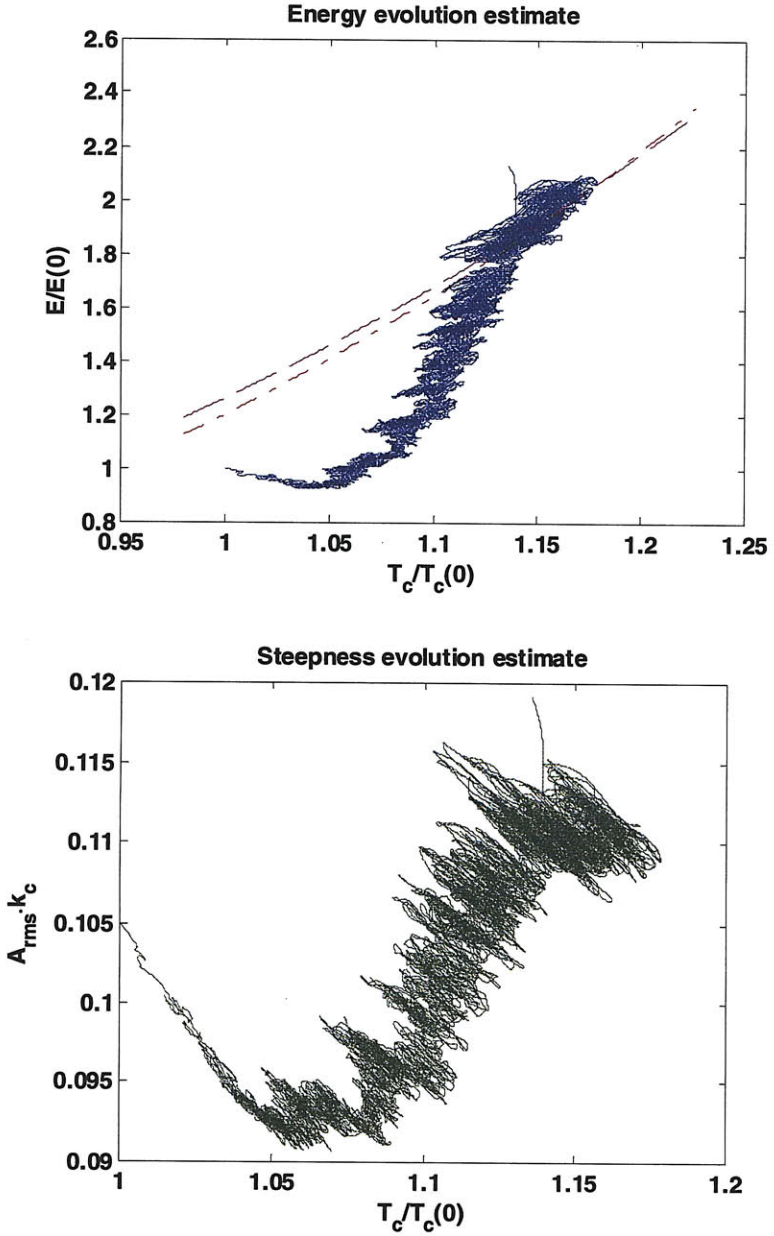

Figure 4.34 Same as Figure 4.26 for simulation described in the title.

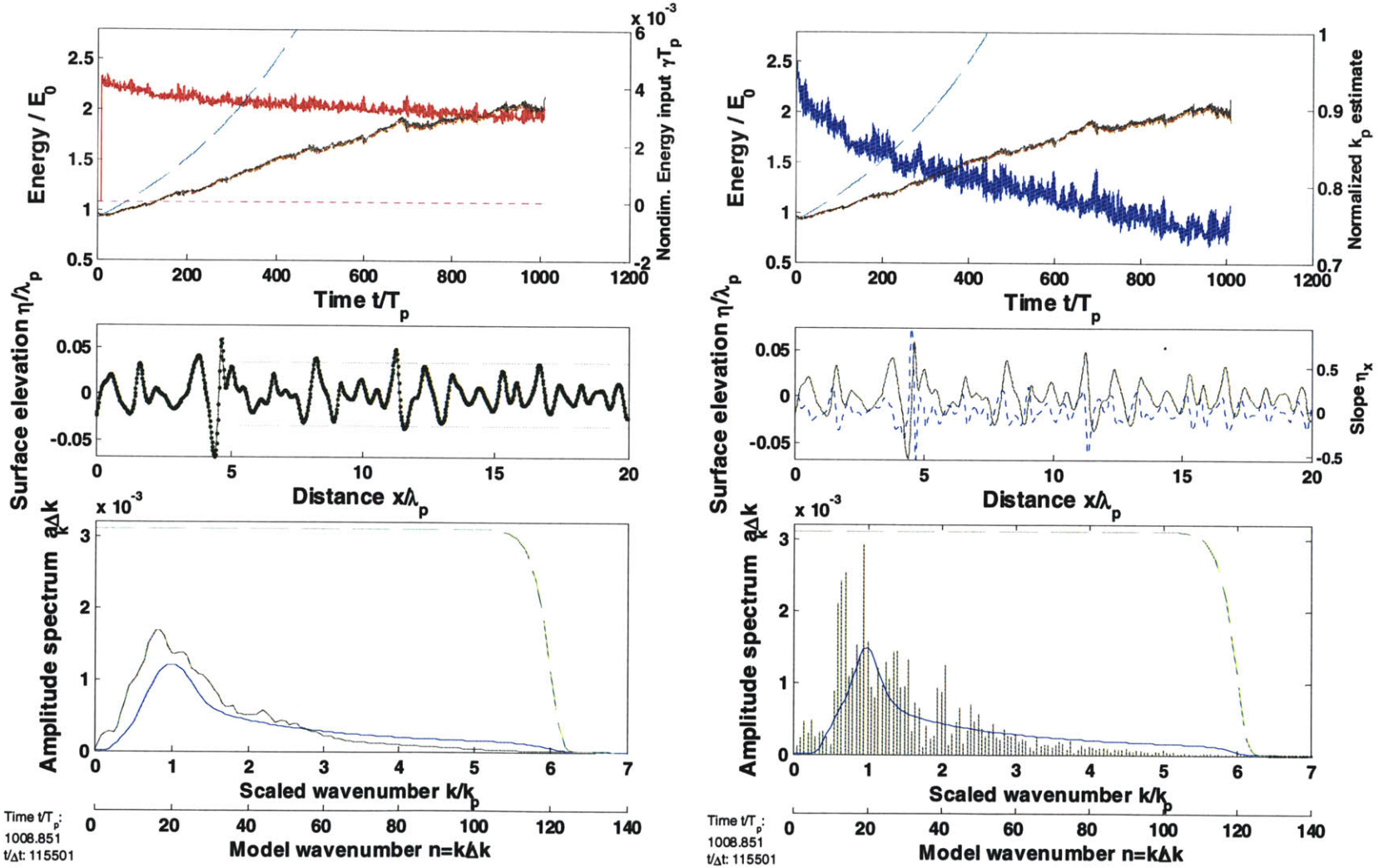

Figure 4.34 (b, b', c, c', d, d') For caption see facing page.

For additional validation of our modeling approach we checked the above results with a modified forcing level in the simulations. Different forcing levels were applied within the scatter of the measured growth rate, consistently with our forcing parameterization approach, see Section 2.2.3. The results for forcing levels 0.0003, 0.0002, and 0.0005 are compared to the simulation shown in Figure 4.26 with forcing level 0.0004. All the other computational and physical parameters are kept the same. The figures show that reducing the forcing level allows to generate longer lasting simulations, 4000 and 6000 Tp respectively, which confirm Toba 3/2 law. The simulation with stronger forcing level crashes after 2000 Tp, but still conforms to Toba law constraints. In all the cases the simulations reproduce the smooth exponential growth with nondimensional growth rate exactly corresponding to the different forcing levels. The deviation from Toba curve of the initial swell evolution, the exponential fast adjustment in the linear regime and the nonlinear quasi-equilibrium – are all reproduced in the simulations, confirming our modeling approach. Nonetheless, these results should be considered preliminary since failure of the simulations is not controlled at this stage. Moreover, the simulations with forcing levels 0.0002 and 0.0003 continued running beyond time displayed in the plots and developed instabilities in 4^{th} harmonic of the initial peak wavenumber. These instabilities as well as the details of phase resolved evolution and simulation crash are not examined in this Thesis, but do suggest further work.

T_{wind}=500T_p, np=10, Forcing level=0.0003

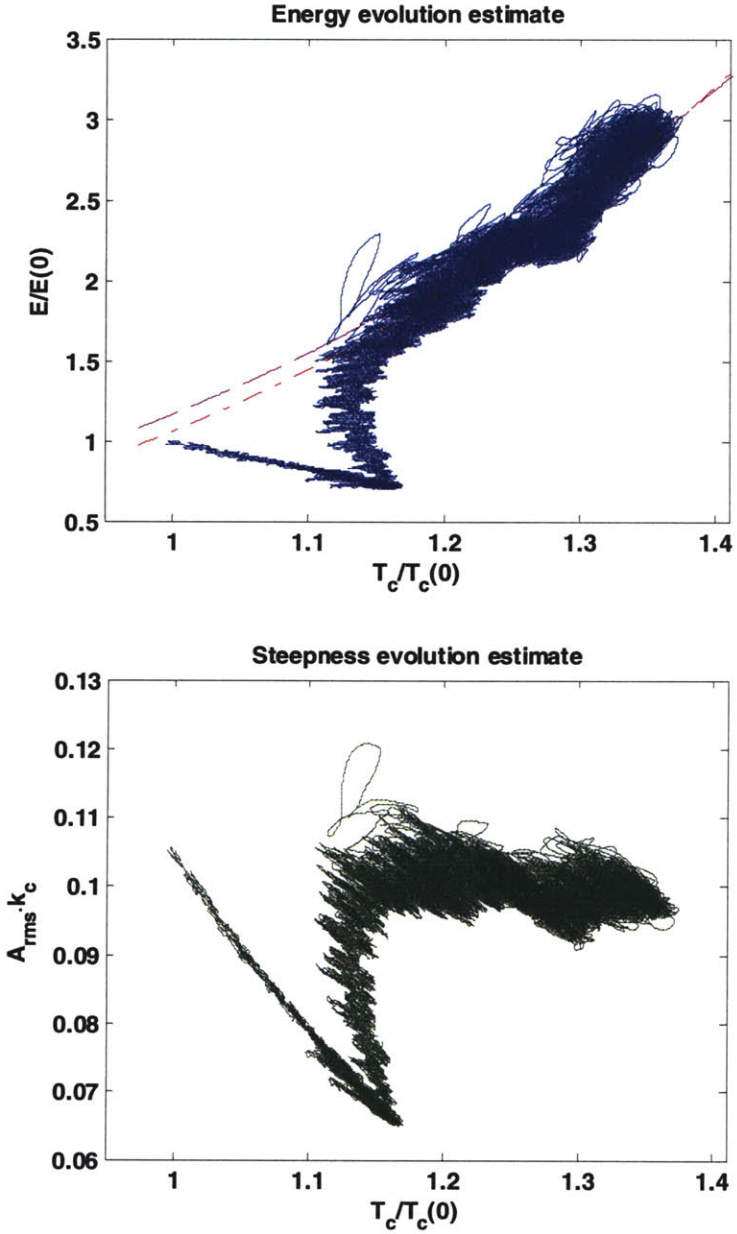

Figure 4.35 Same as Figure 4.26 for simulation described in the title.

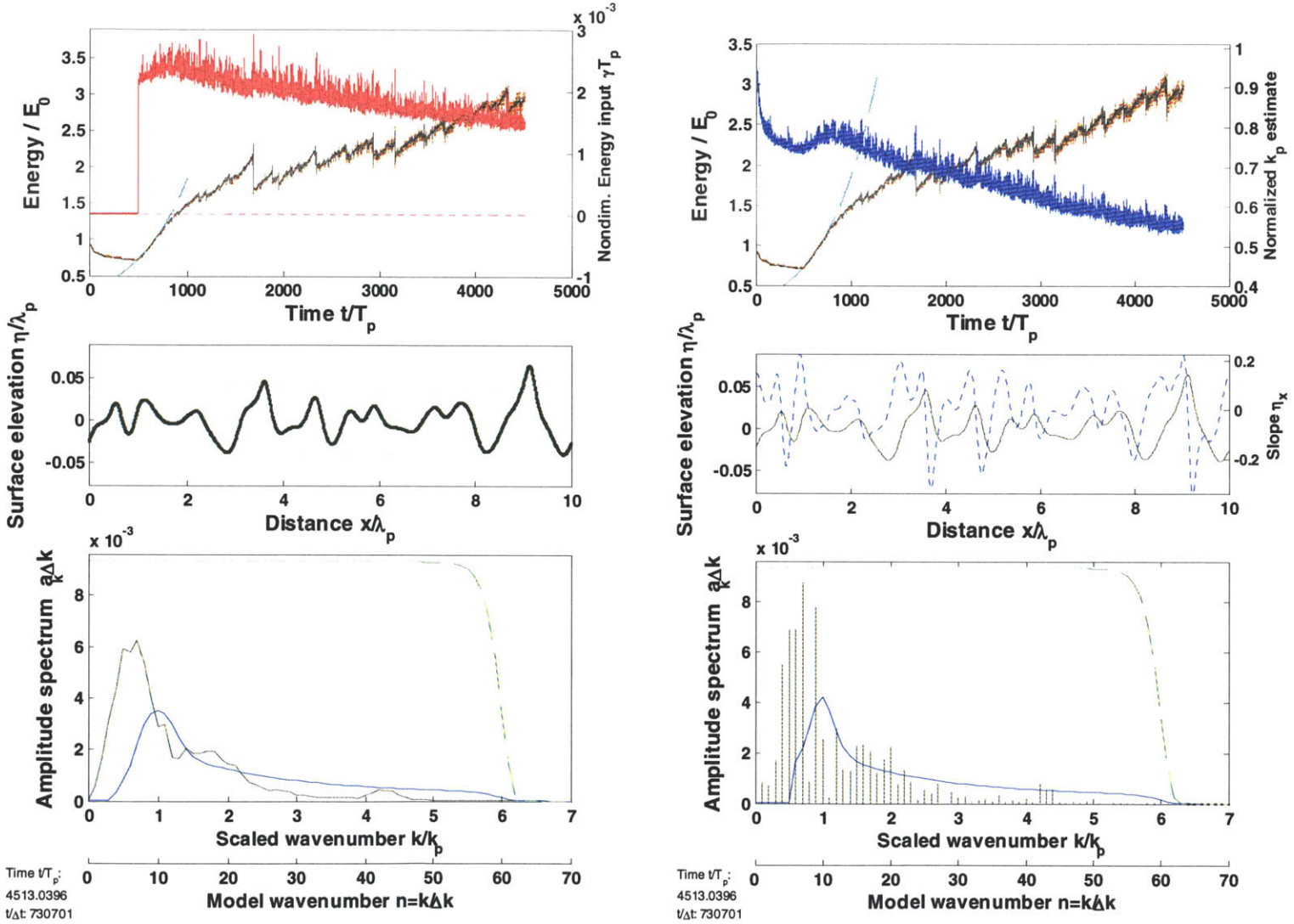

Figure 4.35 (b, b', c, c', d, d') For caption see facing page.

T_{wind}=500T_p, np=10, Forcing level=0.0002

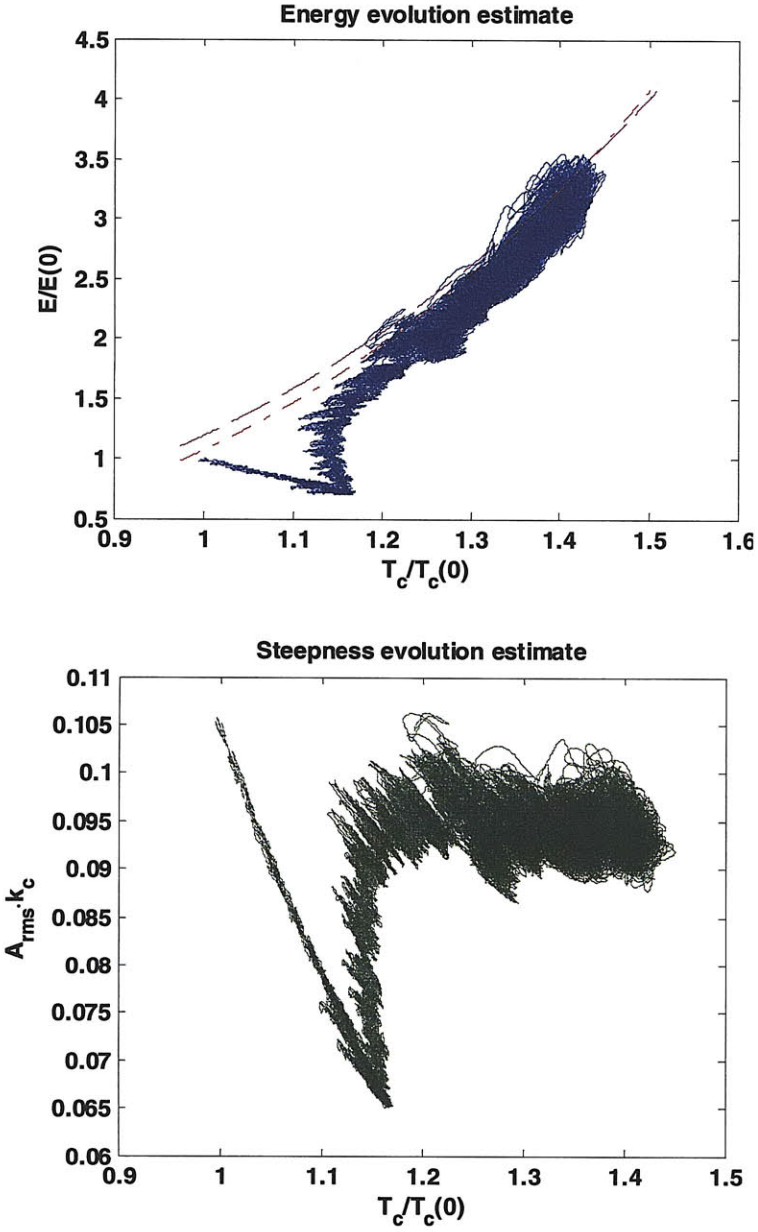

Figure 4.36 Same as Figure 4.26 for simulation described in the title.

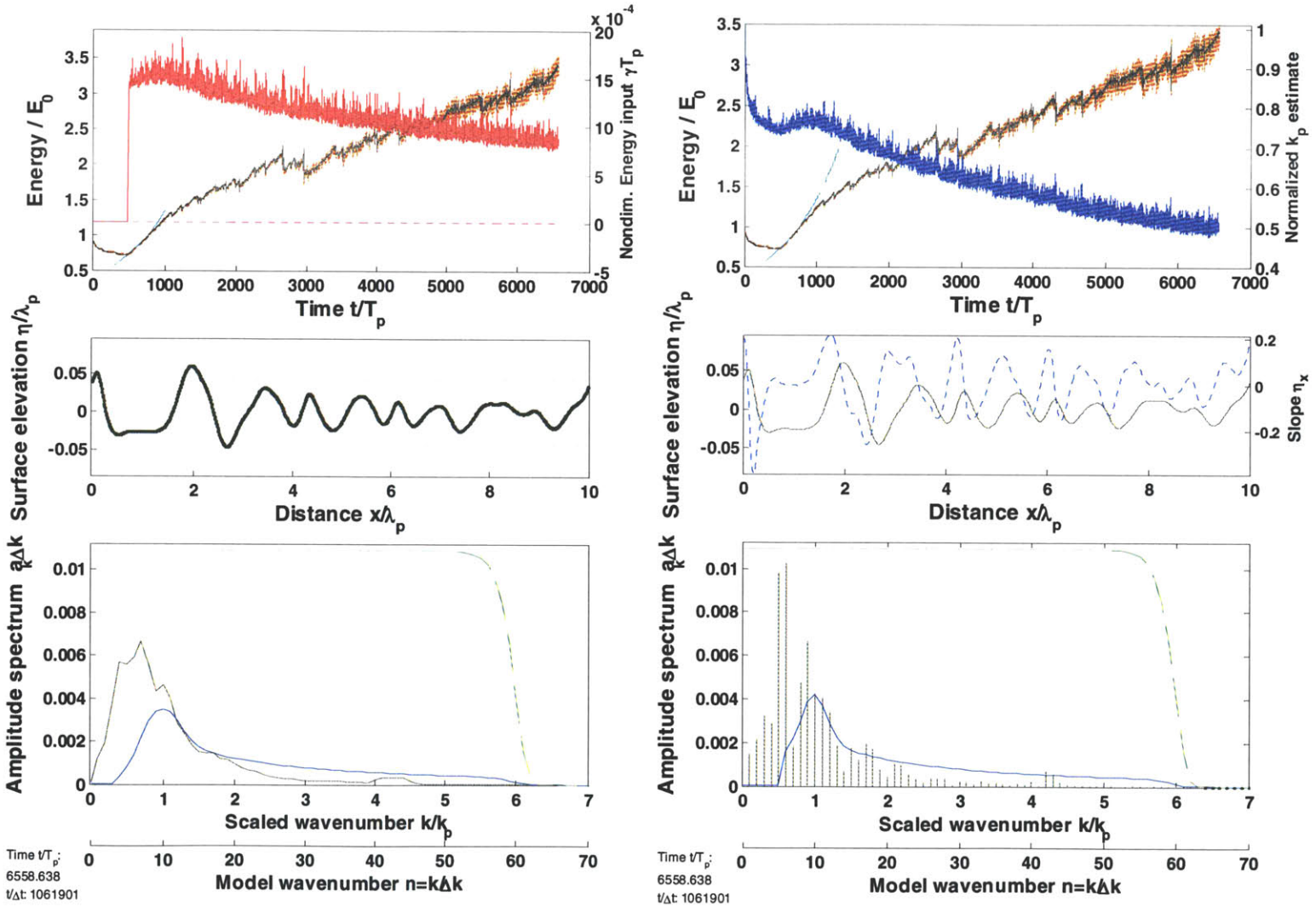

Figure 4.36 (b, b', c, c', d, d') For caption see facing page.

T_{wind}=500T_p, np=10, Forcing level=0.0005

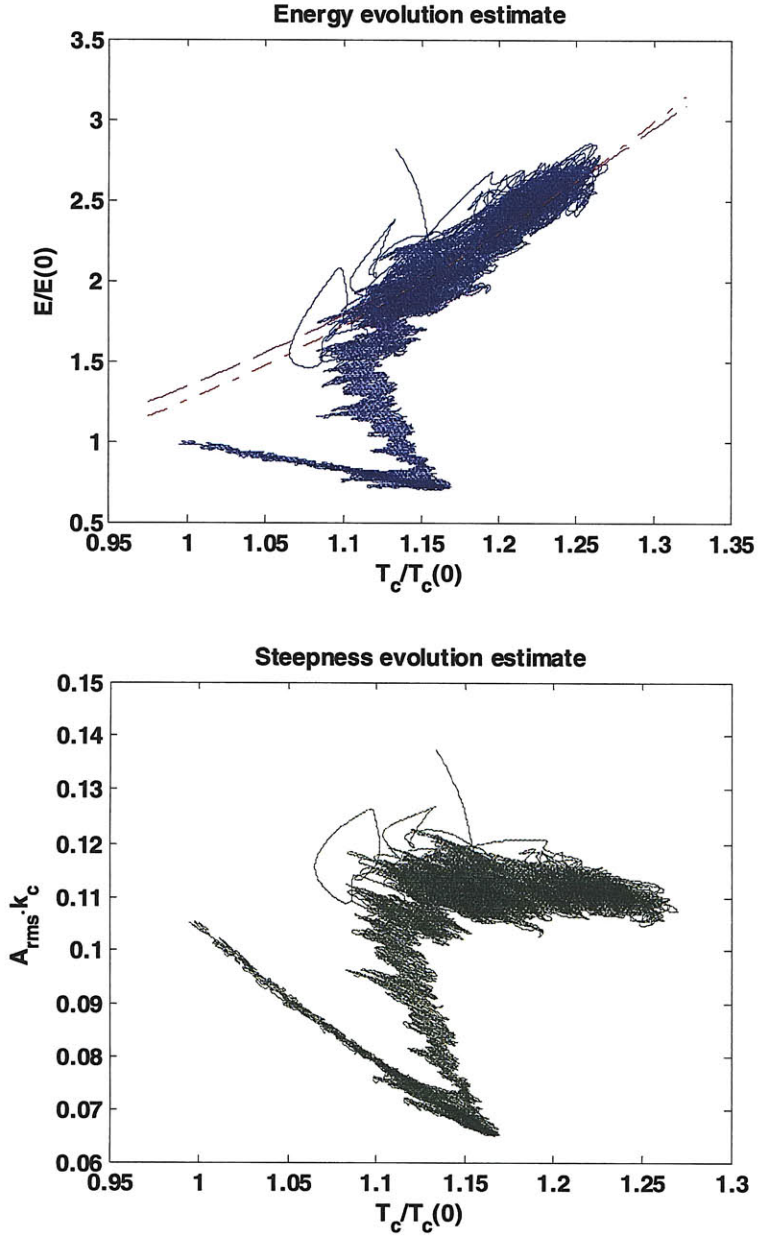

Figure 4.37 Same as Figure 4.26 for simulation described in the title.

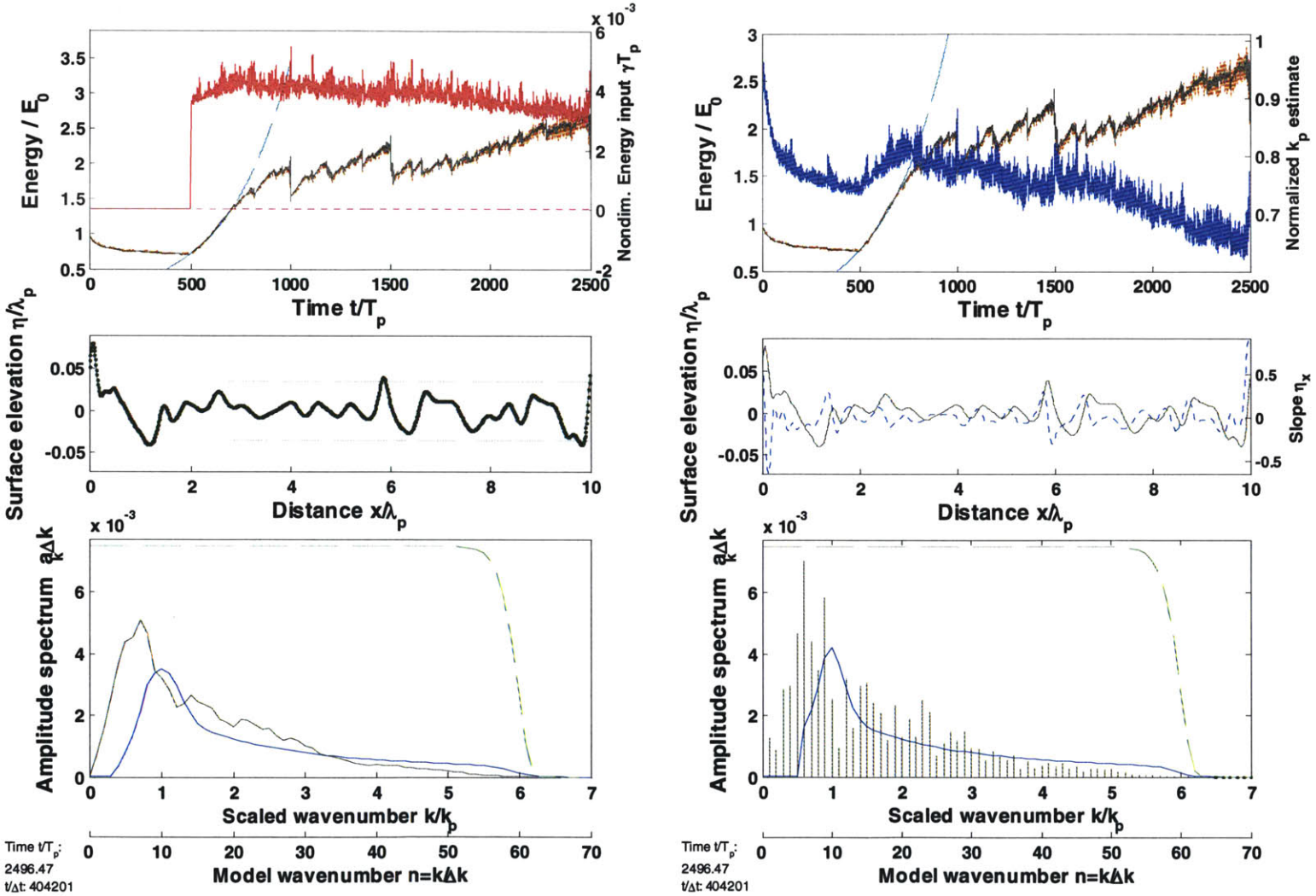

Figure 4.37 (b, b', c, c', d, d') For caption see facing page.

4.4.3. Toba law as upper bound on mixed windsea and swell evolution

Simulations presented in the previous section examined wind wave evolution in three stages observed in the real ocean. Figure 4.38 summarizes these three stages, displaying the evolution curve of simulation from Figure 4.28 in log-log plot. The swell, corresponding to evolution from point A to point B, propagates free of wind forcing slowly downshifting and decaying away from Toba equilibrium curve. Pure windsea, C to D, slowly grows in intermittent quasi-equilibrium with the wind following the 3/2 law. The transition between swell and windsea, B to C, is fast and governed by linear growth mechanism resulting in exponential growth. Note, that although in this graphical presentation the exponential transition leg appears longer that the path along Toba curve, it is the equilibrium growth that takes an order of magnitude longer time in the simulation.

Understanding of the three stages of evolution allow qualitative comparison to real observations obtained in mixed windsea and swell conditions. Figure 4.38 shows the simulated data on the same scale as data of Ebuchi et al. (1992). Although the simulated swell conditions deviate a little distance from the equilibrium curve and the simulated equilibrium growth spans only a small portion of the measured range, the model explains the observations. The asymmetry of the measured data, which appears only on one side of Toba curve, is explained by simulated decay of swell and the fast exponential growth under wind forcing. The simulation shows that wind forced waves do not grow arbitrarily, but are constrained by Toba law. Toba 3/2 law is confirmed by both observations and simulations as the universal upper bound on evolution of irregular wind waves under steady wind forcing.

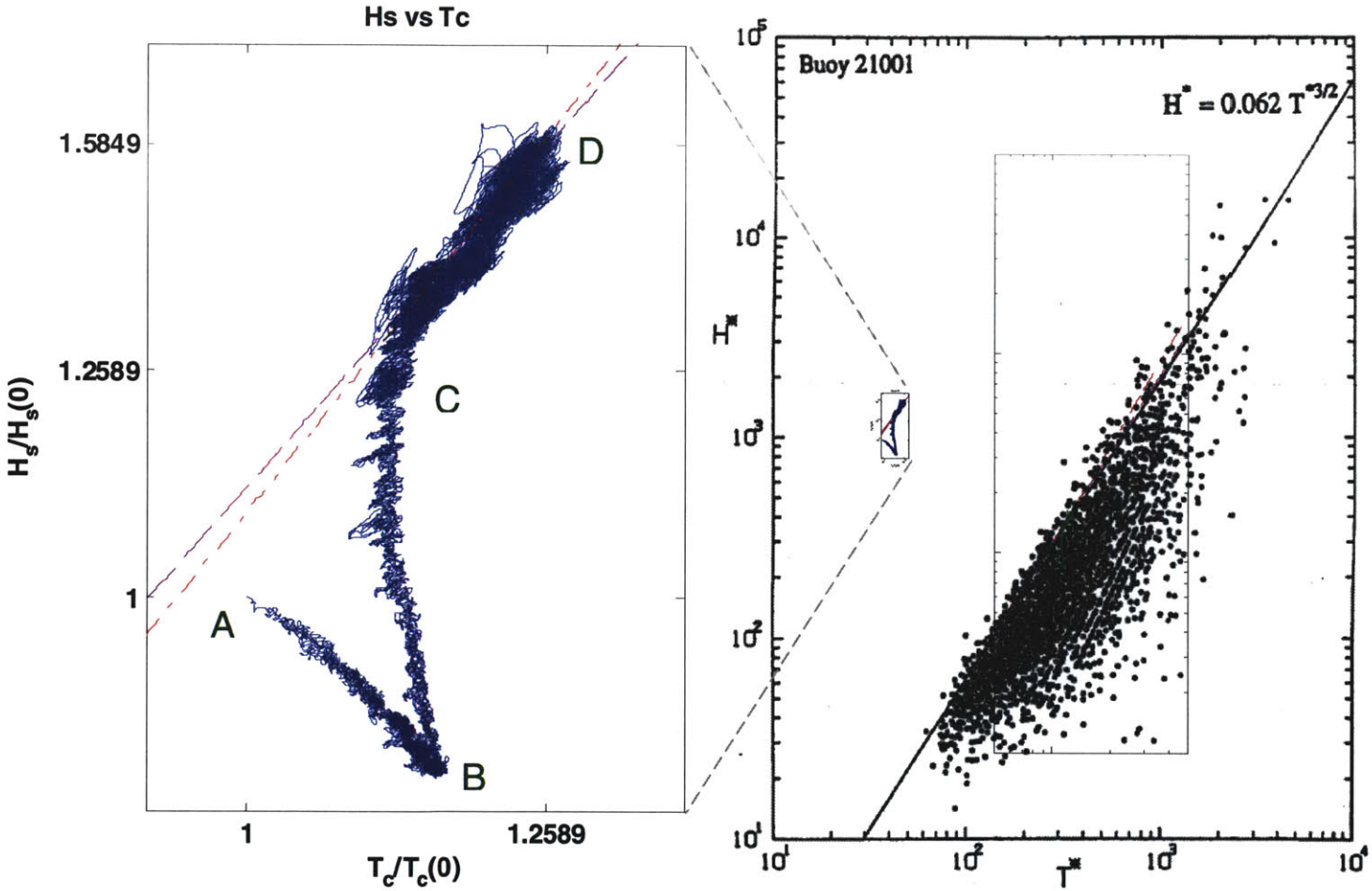

Figure 4.38 Significant wave height vs. characteristic period. Left plot – simulation data from Figure 4.28 compared to Toba 3/2 law (magenta dashed line) and Donelan et al. (1985) parameterization (red dash-dotted line). Right plot – simulation data scaled and compared to observations of Ebuchi et al. (1992).

4.4.4. Nonlinear wind forcing

The goal of this Thesis is modeling wind forcing for phase resolving simulation of nonlinear wind waves. Analysis of the available experiments and the existing linear theory suggested implementation of a simple linear forcing model as the leading order approximation of the real forcing mechanism. Because the exact nonlinear mechanism of wind forcing is not currently understood, application of the linear forcing mechanism in nonlinear simulation allows a plausible model of the nonlinear wind forcing mechanism by simulation of the nonlinear wind-wave interaction process. The nonlinear irregular wave field interacts with wind described by the simplified model, each spectral component induces some energy transfer from the wind. The integral flux of energy to the broadband nonlinear wave system is the estimate of the nonlinear wind forcing. The nonlinear work of wind is given by (4.2.2) and is calculated at every time step of the model. Example of such nonlinear energy flux calculation is shown in Figure 4.39 nondimensionalized by the changing energy and mean frequency

$$\frac{\dot{E}}{\omega_p E} \tag{4.4.4}$$

Wind work is zero in the first 500 periods of this simulation. During the smooth linear response to wind forcing the integral nonlinear wind work increases slightly O(10%), which is also the scale of the intermittent fluctuations in this simulation. After the system reaches quasi-equilibrium growth stage the nonlinear wind work decreases gradually. Interesting to note that both the increase and the decrease of the normalized wind work is observed despite the opposing effect of the mean wavenumber, which is used to normalize the wind work and grows during the exponential growth and downshifts during the equilibrium stage.

The simulated nonlinear wind input function is compared to the experimental data on Figure 4.40. The calculated wind work is plotted against the measured growth rate due to direct wind input. It is compared to the linear parameterization of growth rate and is found to follow a similar trend, but is about 20% stronger in magnitude. The stages of

simulation from the previous Section are shown for convenience. The abrupt start of wind forcing corresponds to point B (yellow circle). Then wave age decreases slightly, corresponding to the slight upshift during the linear response of the wave system (B to C), and wind input increases. After the simulation transitions to the balanced growth state (C to D), wind input is reduced along with wave age increase. This dynamics reproduces the observed evolution of wind waves and is consistent with the conceptual framework of developing wind wave system.

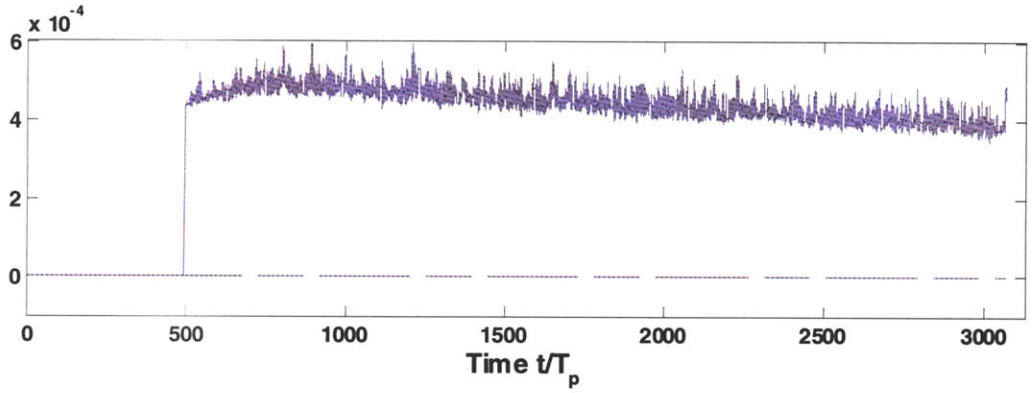

Figure 4.39 Normalized nonlinear wind work in simulation data from Figure 4.28 as function of simulation time.

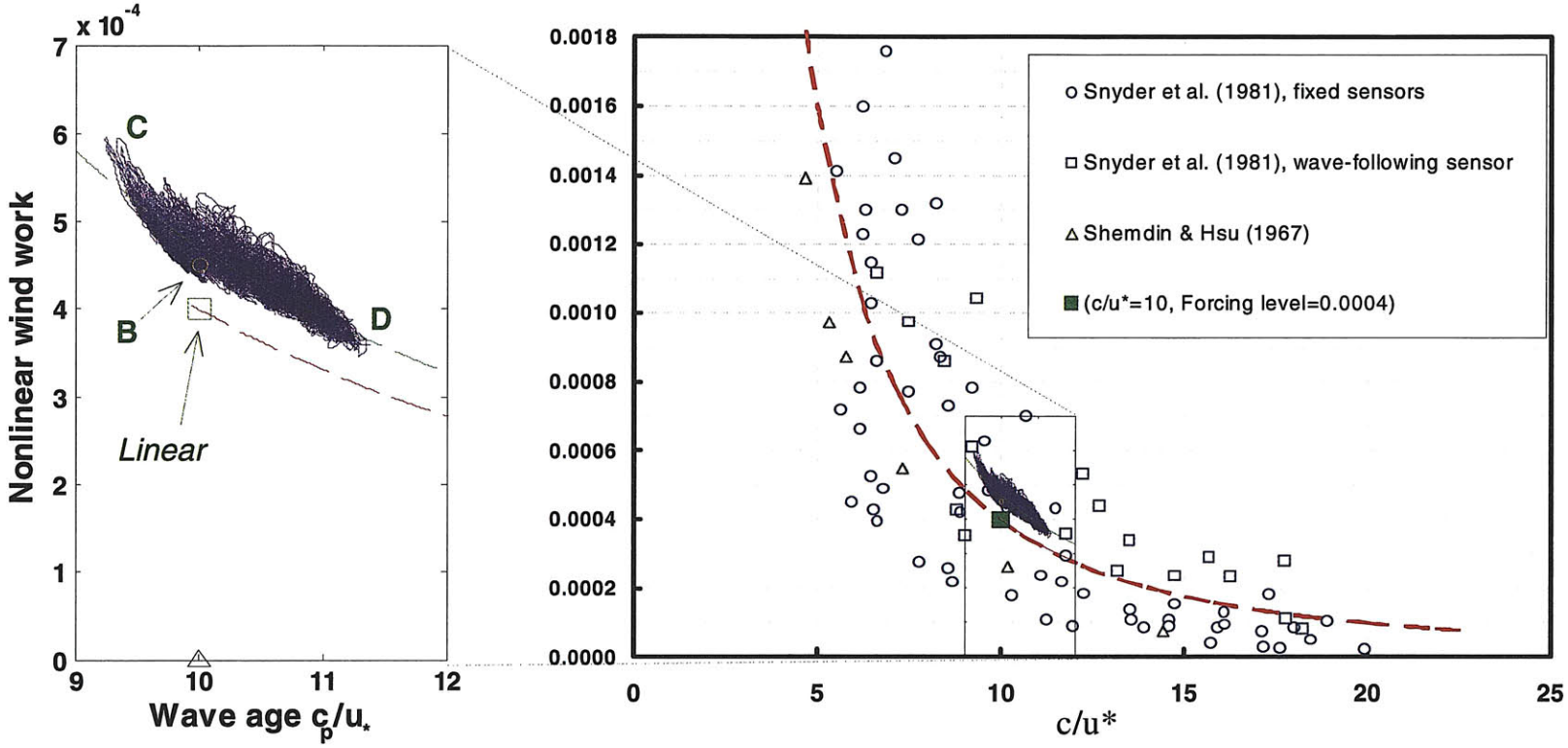

Figure 4.40 Normalized nonlinear wind work vs. wave age for simulation data from Figure 4.28. The initial simulated point (green square) corresponds to wave age 10 and linear forcing level 0.0004. Green dashed line is $(c_p / u_*)^{-2}$ fit with constant α corresponding to the nonlinear forcing, see Section 2.2.3.

Chapter 5. Summary and Discussion

5.1.1. Approach

The goal of this thesis was to develop a direct phase resolving modeling methodology for simulation of nonlinear wind waves. The motivation for high resolution phase resolving simulation capability is driven by modern applications' demand and increasing computational power opportunity. Contemporary wind wave forecasting models resolve only phase averaged power spectra and statistical parameters, which do not provide detailed hydrodynamic information on complex wave fields. On the other hand, the existing phase resolving hydrodynamic simulation techniques are computationally intensive and are not scalable to realistic scales of geophysical interest. The method developed in this thesis overcomes the limitations of both alternatives. The model is scalable and computationally efficient. It resolves the detailed kinematics and geometry of complex irregular wave fields. Model formulation is based on primitive equations and Hamiltonian formalism, which allow it to resolve the governing nonlinear dynamics with high level of theoretical validity.

The developed model is based on the High Order Spectral (HOS) method (Dommermuth and Yue 1987), which is a pseudo-spectral numerical technique for phase resolving simulation of free regular waves in periodic domain. In this thesis the HOS method is discussed in detail and modified for simulation of irregular wind waves. The modifications required development of wind forcing and wave breaking extensions for the method. They also required development of methodology for simulation of broadband irregular non-stationary wave field in a discrete numerical grid. A principal challenge encountered was consistent resolution of the observed non-conservative dynamics with a conservative numerical scheme dependent on numerical dissipation for stabilization of computational instabilities.

The model of wind forcing developed in this thesis is physics based, consistent with Miles' linear theory and calibrated by available experimental data. Wind forcing is

assumed to be primarily a form drag mechanism acting on the surface through a wave-induced slope-coherent distribution of normal stress. The mechanism is parameterized in terms of wave age in linearized framework of weakly interacting spectral components of the wave field, and its magnitude is adjusted by the observed growth rates. Linear formulation of the forcing is adopted and applied directly to the nonlinear evolution equations.

To model the effect of wave breaking we adopted the low-pass filtering approach which was developed originally as numerical stabilization technique. The low-pass model of wave breaking is justified phenomenologically by associating the fine structure of breaking crests with high wavenumber variability, dissipation of which is assumed to represent the energy lost in distinct wave breaking events. In our simulations the small scale energy content is removed continuously by a smooth zero-phase low-pass filter. The undesirable effect of this constant filtering is blending the physical mechanism of wave breaking with artificial numerical dissipation. The high frequency spectral components are effectively assumed unessential to dynamics of energy containing waves.

This thesis presents detailed derivation of our nonlinear phase resolving model and tracks the procedure of simulation development and calibration. The model is validated versus linear theory expectations and established experimental parameterizations. The successful simulations provide new insight into the physics of energy containing wind waves. The theoretical hypothesis (Toba 1998) of nonlinear quasi-equilibrium of waves with wind as the governing mechanism of intermittent turbulent growth is confirmed numerically and shown to satisfy the observed parameterizations. The simulations resolve the transition from initial growth, due to direct wind input, to the equilibrium growth in non-conservative balance of wind forcing and wave breaking dissipation. Observed duration limited evolution is explained by the balanced growth, which satisfies Toba 3/2 law and acts as the upper bound on development of mixed windsea and swell sea states under steady winds.

This study is limited to two dimensional system of deep long crested waves. This is the natural setting for extension of the linear wind-wave interaction theory (Miles 1957), which is also formulated only for deep long crested waves. Also, there is sufficient experimental evidence that generation and initial growth of wind waves is a two dimensional process (Kawai 1979, Veron and Melville 2001), which justifies our modeling approach. Nonetheless, the observed wind waves in the ocean are three dimensional. Full account for the nonlinearity of irregular ocean waves may require three dimensional considerations. It is therefore an interesting open question to extend this study to three dimensions and examine the applicability of our potential flow framework to real ocean waves. It must be noted that doubts regarding such extension appear since the observed transition of two dimensional waves to three dimensional irregular wave fields must be coupled to additional three dimensional processes like Langmuir circulations and water side turbulence, which are beyond the applicability of our potential flow based approach. Another extension of current study is the effect of finite depth on growth of long wind waves. This is within the applicability of potential flow framework and is relevant in coastal areas.

5.1.2. Challenges

HOS method is an established and capable means for simulation of regular nonlinear waves free of wind forcing. Its application to large scale simulation of realistic ocean wind waves requires, however, resolving the principal limitations of HOS theoretical formulation and current numerical implementation. In the context of adding wind forcing, the key challenge is the fundamental incompatibility of HOS energy conserving formulation and the ad-hoc non-conservative implementation. The problem appears when wind energy input is added to a model that is stabilized by energy removal. The delicate balance of filtered out instabilities is disturbed, growth that was considered only a numerical artifact is now blended with a valid response to supplied forcing. Insufficient theoretical grounds of the subject contribute to the confusion, since theory of non-conservative nonlinear wave dynamics appears to be lacking. A detailed analysis of the nonlinear response of nonlinear wave system to wind forcing would illuminate the

underlying dynamics and necessarily contribute to application of HOS method to the problem of realistic wind waves.

Development of the theoretical foundations of the model is not finished in several aspects. There are no rigorous bounds or guidelines for choice of computational parameters and theory of model convergence has not been established, except for specific demonstrations for few idealized cases (Dommermuth and Yue 1987). There are no definite guidelines how to prevent simulation crash. The model was found to be numerically unstable and by inspection this was attributed to growing round-off errors. No specific stability analysis or tracing of the exact nature of numerical instabilities was published. The simulations are stabilized by filtering out of high frequency components, which may violate the dynamical consistency as was demonstrated in the case of volume conservation violation. Wave breaking dissipation routine is based on same low-pass filtering idea. Existing physics based wave breaking theories were not implemented yet. The problem of consistent initial conditions and simulation initialization procedure is not solved, ad-hoc "ramp up" and "warm start" techniques (Dommermuth 2000) are implemented for no theory based alternative was established.

Beyond specifics of HOS method, the general concept of phase resolved modeling for real ocean waves is still a subject of ongoing research. Fundamental questions exist with regard to ergodicity, randomness and deterministic predictability of irregular broadband non-stationary wavefields (Huang et al. 1999, Liu 1999, Liu et al. 2001) and validity of their representation in discrete spectral models (Bretherton 1964, Rasmussen and Stiassnie 1999, Tanaka and Yokoyama 2004, Lvov et al. 2006). Another weak point of the HOS method is resolution of long-short wave interactions and the effects broadbandedness and scale separation (Brueckner and West 1988, Zhang et al. 1993). Effects of slow viscous dissipation have been partially addressed (Wu et al. 2006) and are in the focus of current active research.

The key technical challenge in developing nonlinear wind wave model was generation of simulations of sufficient length. Given the basic questions above, which provide a basis

for further theoretical investigation and expose the insufficient theoretical foundation of the model, the development of nonlinear simulations was based on random optimization of computational parameters. The main challenge was wave breaking. Although the stabilizing effect of the low-pass filter was confirmed, different wave breaking filters were found to have competing effects on length and quality of the simulations. On the one hand, stronger filters with lower cut-off wavenumber allow longer simulations. But this is achieved by removal of meaningful spectral content. In other words, longer simulations are potentially less meaningful. Stronger filters limit the bandwidth resolution of the simulations. Also, on the other hand, the narrower bandwidth simulations appeared rougher with more intermittent fluctuations of the output, which suggests opposite of convergence. The wider bandwidth simulations appeared smoother and converged, but crushed earlier due to wave breaking. No direct solution to this conflict was found, and the progress was achieved by choosing the stronger filtering approach. Although the mathematical convergence of the narrowband strongly filtered simulations is questionable, their longer extent revealed qualitatively different dynamics. The longer simulations evolved from the smooth response to wind forcing to a rough and intermittent state of growing and breaking chaotically. It is this irregular dynamics that was interpreted to be the proper representation of the natural process.

An explanation for the abandonment of the smooth converged simulations in favor of the intermittent irregular ones may be found by understanding the disparity between the turbulent non-conservative nature of the actual phenomenon of irregular wind waves and our modeling approach based on the conservative HOS scheme. HOS model was developed for regular waves, propagating free of wind forcing, interacting nonlinearly and breaking occasionally loosing only small fraction of their energy. Thus, HOS model is consistent with nearly conservative dynamics of free waves, the minor energy losses of which are successfully simulated by artificial numerical dissipation. Modeling of wind waves, however, required development of non-conservative simulations which capture the irregular dynamics due to wind forcing and breaking dissipation, which is the mechanism explained by Toba as local quasi-equilibrium. It was discovered that as the

waves grow, their breaking characteristics change from isolated weak discrete events to continuous intermittent and violent energy loss. When the length of simulations was $O(10^3\ T_p)$ the simulations remained smooth and reproduced only exponential growth consistent with the linear theory. Only the success to generate longer simulations, $O(10^4\ T_p)$, allowed capturing the transition to the intermittent growth and breaking balance, which we interpreted as the local quasi-equilibrium of growing windsea.

5.1.3. Contributions

Both stages of simulated wave growth in response to wind forcing can be interpreted in terms of established observations. The initial smooth exponential growth, which corresponds to linear instability mechanism, is interpreted as initial growth measured in laboratory conditions (Larson and Wright 1975, Kawai 1979, Veron and Melville 2001). Wave breaking is weak. All the energy supplied by the wind is absorbed in the wave field. As the wave field grows and saturates, it transitions to the intermittent non-conservative regime, when a significant fraction of energy supplied by the wind is continuously lost in wave breaking. The balance of energy supply and loss appears to be in equilibrium with the applied wind forcing, which is consistent with Toba's explanation (1978, 1998) of this regime as a local quasi-equilibrium of windsea, governed by a nonlinear adjustment mechanism. We show that this regime is consistent with Toba 3/2 law and the observed parameterizations of duration limited evolution.

During the wind free evolution the trajectory of sea state diverges from Toba equilibrium curve corresponding to simulation of swell conditions. As soon as wind is applied wave field responds fast and adjusts back to the equilibrium curve and continues to evolve slowly along it. This confirms Toba hypothesis of fast equilibrium adjustment to wind forcing. The equilibrium curve, or equivalently Toba 3/2 law or duration limited evolution, act as an upper bound on development of mixed windsea and swell sea states explaining the data collected by Ebuchi et al. (1992).

The three stages of simulated wind wave evolution: swell, windsea and fast transition have been also seen in evolution of the significant steepness as function of the characteristic period. The evolution starts from a value that corresponds to the observed Donelan et al. (1985) spectrum, goes down during wind free evolution and restores quickly to the initial value as wind forcing is turned on. Then it slowly decays as the downshift overwhelms the energetic growth corresponding to Toba similarity law.

Eventually, we can quantitatively answer the key modeling question: How much energy does wind transfer to waves for broadband nonlinear spectrum. The model allows direct nonlinear calculation of the integral nonlinear wind work. Initial broadband growth is superposition of separately growing spectral components each independently satisfying the linear theory. The integral growth rate is dominated by the strong characteristic modes and the total growth rate is consistent with linear estimates for the peak mode. Gradually the growing wave field saturates and transitions to intermittent breaking equilibrium, when fraction of energy supplied by the wind is lost to breaking and the total growth rate is in accordance with the observed duration limited parameterizations.

5.1.4. Conclusions

Interesting practical conclusion can be drawn from this study regarding to the approach to simulation of complex turbulent systems. It appears that when the goal is to simulate an irregular non-stationary system, the desired result doesn't lie in the smooth and ordered balanced evolution, but in the rough intermittent apparently chaotic disorder, where the validity of the method itself might be questionable. Surprisingly this chaotic variability provides valuable insight about the nature of the complex turbulent phenomena and is in accordance with the established experimental metrics.

We have shown that our simple model was sufficient to resolve the apparent complexity of the coupled wind-wave system. It appears that with proper account for nonlinearity, with even simple parameterizations of the non-conservative source functions, our phase resolving approach succeeds to capture both the characteristic irregularity and ordered

similarity of the non-stationary evolving system. Our simple model of wind forcing, which does not account for air turbulence, appears sufficient to induce realistic irregular wind-wave field, which can be explained solely by the nonlinearity of wave hydrodynamics with only crude account for wave breaking dissipation. This suggests that the complex properties of the observed wind waves may be reproduced in a deterministic model that properly resolves the inherent properties of the nonlinear waves and no resort to randomness or air turbulence models is required. Thus, our phase resolving nonlinear method for wind-wave simulation may be sufficient to capture the essential physics of ocean wind waves and may be the basis for development of new generation of highly accurate wave forecasting models. Therefore we conclude that our modeling approach provides a feasible computational basis for development of novel phase resolving systems for simulation and forecasting of realistic ocean wind waves.

Appendix A. Linear theory of response to wind forcing

In Section 2.2.2. the model of wind forcing on linear monochromatic wave was derived heuristically. External slope coherent surface pressure distribution was applied on the surface of a linear wave. The work done by this pressure on surface particles moving as prescribed by the solution of free linear wave was calculated and assumed to be fully absorbed by the wave. Energy balance was utilized then to quantify the growth of the linear wave, i.e. the amplitude of the wave was assumed to grow in accordance to the increase of its linear energy estimate. This approach does not appear fully consistent. The motion of the particles on the surface of a growing wave may not be exactly the same as for a free wave. Thus the work done by the prescribed surface pressure on a growing wave may be different from the work that was calculated. Further, the assumption that linearized energetics compel the dynamic response of the system requires substantiation. It is not obvious a priori that all the work done on the wave can be absorbed in dynamically consistent manner.

Below we describe an alternative approach. We solve directly the original linearized equations of motion for forced surface wave. We compare this solution to the free wave solution and to the result of the heuristic argument. We will show that the exact properties of the growing linear wave are different from the approximate result of the heuristic approach. However, in the observed range of parameters relevant to the energy containing waves in the ocean the differences are small. This justifies the heuristic approach in linear and almost linear studies. Nonetheless, in higher order nonlinear study these differences may have important effects and have to be considered.

A.1. Linear solution and free wave

Consider the standard linear solution for surface wave. The nonlinear equations of motion

$$\begin{cases} \Delta\varphi = 0 & |_{z\le\eta} \\ \varphi_z = \eta_t + \varphi_x\eta_x & |_{z=\eta} \\ \varphi_t + g\eta + \frac{1}{2}\nabla\varphi\cdot\nabla\varphi = -\dfrac{P}{\rho_w} & |_{z=\eta} \\ \varphi_z = 0 & |_{z=-\infty} \end{cases} \tag{A.1}$$

reduce to

$$\begin{cases} \Delta\varphi = 0 & |_{z\le 0} \\ \varphi_z = \eta_t & |_{z=0} \\ \varphi_t + g\eta = -\dfrac{P}{\rho_w} & |_{z=0} \\ \varphi_z = 0 & |_{z=-\infty} \end{cases} \tag{A.2}$$

Combining the kinematic and dynamic boundary conditions the governing equation is

$$\varphi_{tt} + g\varphi_z = -\frac{P_t}{\rho_w} \quad |_{z=0} \tag{A.3}$$

For given wavenumber k the relevant solution of Laplace equation is

$$\varphi = \mathrm{Re}\left[\psi(t)e^{ikx}e^{kz}\right] \quad |_{z\le\eta} \tag{A.4}$$

The governing equation in terms of surface potential amplitude is

$$\psi_{tt} + gk\psi = -\frac{P_t}{\rho_w}e^{-ikx} \tag{A.5}$$

The solutions are obtained from the standard ansatz

$$\psi(t) = e^{\gamma t} \tag{A.6}$$

For free wave it is

$$
\begin{aligned}
&\gamma^2 + gk = 0 \\
&\gamma = \pm i\sqrt{gk} \equiv \pm i\omega_0 \\
&\varphi = \mathrm{Re}\left[Ae^{\pm i\omega_0 t} e^{ikx} e^{kz} \right] \\
&\eta = \pm A\sqrt{\frac{k}{g}} \sin(kx \pm \omega_0 t)
\end{aligned}
\tag{A.7}
$$

A is an arbitrary amplitude. The wave oscillates and propagates with phase velocity according to the linear dispersion relation.

A.2. Forced wave: elevation coherent pressure

For linear wave forced by elevation coherent surface pressure

$$
\frac{P}{\rho_w} = b\eta \tag{A.8}
$$

the governing equations are

$$
\begin{aligned}
&\begin{cases} \varphi_z = \eta_t \\ \varphi_t + g\eta = -b\eta \end{cases} \\
&\varphi_{tt} + g\varphi_z = -b\varphi_z \\
&\psi_{tt} + gk\psi = -bk\psi
\end{aligned}
\tag{A.9}
$$

The eigenvalue equation

$$
\gamma^2 + gk + bk = 0 \tag{A.10}
$$

can be expressed in terms of a modified gravity

$$
\begin{aligned}
&g' \equiv g + b \\
&\gamma^2 + g'k = 0
\end{aligned}
\tag{A.11}
$$

The solution is similar to the free wave case only with modified dispersion relation

$$
\begin{aligned}
&\omega = \pm\sqrt{(g+b)k} \\
&\eta = \mathrm{Re}\left[\mp i\sqrt{\frac{k}{g}} Ae^{ikx \pm i\omega t} \right]
\end{aligned}
\tag{A.12}
$$

We note that when surface pressure is in anti-phase with the elevation and is strong enough

$$b < -g \tag{A.13}$$

the forced wave does not propagate but grows exponentially. This instability mechanism is briefly discussed by Lighthill (1962), who highlights that it is not a mechanism of wave growth. This mechanism is known as aerodynamic suction and is equivalent to the Kelvin-Helmholtz instability at the sheared interface of two uniform flows. Physically, this mechanism is responsible for generation of spray over high waves in strong wind. Its direct effect in wind wave generation is not typically recognized.

A.3. Forced wave: slope coherent pressure

For linear wave forced by slope coherent surface pressure

$$\frac{P}{\rho_w} = a\eta_x \tag{A.14}$$

the governing equations become

$$\begin{cases} \varphi_z = \eta_t \\ \varphi_t + g\eta = -a\eta_x \\ \varphi_{tt} + g\varphi_z = -a\varphi_{zx} \\ \psi_{tt} + gk\psi = -aik^2\psi \end{cases} \tag{A.15}$$

The quadratic eigenvalue equation is

$$\gamma^2 + gk + iak^2 = 0 \tag{A.16}$$

Its solutions are

$$\gamma = \pm(a^2k^4 + g^2k^2)^{\frac{1}{4}} e^{i\frac{1}{2}\mathrm{atan}(ak^2/gk) + i\pi/2} \tag{A.17}$$

To clarify the presentation of the solution we define

$$\Gamma \equiv ak/g \tag{A.18}$$

The eigenvalue equation is written as

$$\gamma^2 = -gk\left(1+iak/g\right) = -gk\left(1+i\Gamma\right) \tag{A.19}$$

The solution as

$$\gamma = \pm\sqrt{gk}\left(\Gamma^2+1\right)^{1/4} e^{i\left(\frac{1}{2}\operatorname{atan}\Gamma+\frac{\pi}{2}\right)} = \pm\frac{\sqrt{gk}}{\sqrt{2}}\left[\sqrt{\sqrt{\Gamma^2+1}-1} - i\sqrt{\sqrt{\Gamma^2+1}+1}\right] \tag{A.20}$$

Where trigonometric identities were used

$$\begin{aligned}
\sin\left(\frac{1}{2}\operatorname{atan}\Gamma\right) &= \frac{1}{\sqrt{2}}\sqrt{\frac{\sqrt{\Gamma^2+1}-1}{\sqrt{\Gamma^2+1}}} \\
\cos\left(\frac{1}{2}\operatorname{atan}\Gamma\right) &= \frac{1}{\sqrt{2}}\sqrt{\frac{\sqrt{\Gamma^2+1}+1}{\sqrt{\Gamma^2+1}}}
\end{aligned} \tag{A.21}$$

The solution for elevation should be obtained from

$$\eta(t) = \int_{t_0}^{t} \varphi_z dt' \tag{A.22}$$

Up to arbitrary initial conditions the solution is

$$\eta = kA\,\mathrm{Re}\left[\frac{1}{\gamma}e^{ikx+\gamma t}\right] \tag{A.23}$$

which up to arbitrary amplitude and phase may be written as

$$\eta = \exp\left(\pm\omega\mathbf{G}t\right)\cdot\cos(kx \mp \omega t) \tag{A.24}$$

where

$$\omega = \omega_0\sqrt{\sqrt{\Gamma^2+1}+1}/\sqrt{2} \qquad \xrightarrow[\Gamma\to 0]{} \omega_0 \tag{A.25}$$

$$\mathbf{G} = \sqrt{\frac{\sqrt{\Gamma^2+1}-1}{\sqrt{\Gamma^2+1}+1}} \qquad \xrightarrow[\Gamma\to 0]{} \frac{\Gamma}{2} \tag{A.26}$$

Note the alternating signs – right propagating wave is growing exponentially. The linear energy growth rate is

$$\frac{\dot{E}}{E\omega} = 2\mathbf{G} \xrightarrow[\Gamma \to 0]{} \Gamma \tag{A.27}$$

It can be seen that in the limit of small forcing level Γ the solution recovers exactly the result of the heuristic argument: the wave oscillates and propagates according to the linear dispersion relation, its nondimensionalized growth rate is equal to the forcing level. However, it must be noted that in the general case the response of the wave to the slope coherent forcing is more complex. The dependence of the actual frequency and amplitude growth rate on the forcing level is plotted in Figure A.1 and Figure A.2. We can see two asymptotic regimes. In the limit of weak forcing we recover the slowly growing free wave in accordance with the intuition of the heuristic argument. The growth rate asymptotes the straight line of constant forcing level. The plot shows that the exponential growth rate of the linear response to forcing deviates from the supplied forcing level for forcing O(1) and higher. Strongly forced wave responds such that its growth is slower that the forcing level. In the asymptotic limit of strong forcing level the nondimensional growth rate is bounded by value 1. The frequency and phase velocity of such strongly forced wave is much faster than the free wave.

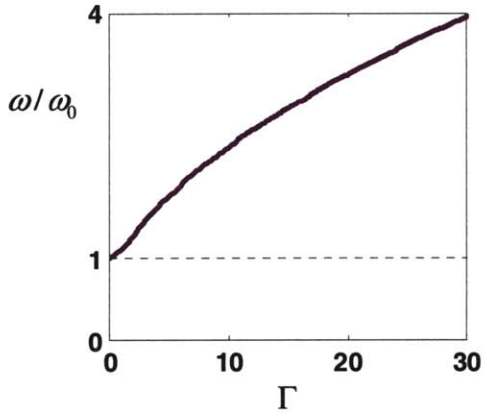

Figure A.1 The normalized frequency of response against nondimensional forcing level.

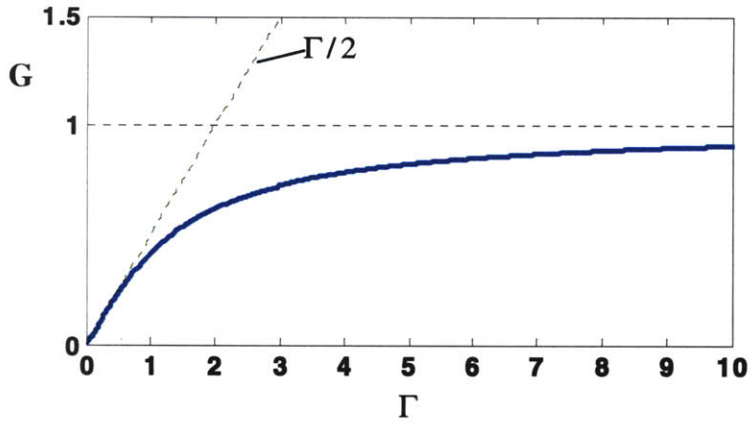

Figure A.2 Amplitude growth rate against nondimensional forcing level.

The presented discussion is set in a linear framework, the demonstrated deviations from the simple result of the heuristic argument are not due to nonlinearity of the wave. These linear effects highlight the difference between free and forced waves. Similar effects have been recognized in the literature (Donelan et al. 1985, see references therein). However, the magnitude of these effects on scale of realistic ocean waves is negligibly small to the leading approximation. For largest measured laboratory growth rates of 0.28, which correspond to wave age 0.4 the relative error from the estimated forcing level is only O(2%). Nonetheless, in higher order nonlinear studies these linear effects may be comparable to higher order nonlinear effects. This suggests further investigation.

References

Banner, M. L., and J. B. Song, 2002: On determining the onset and strength of breaking for deep water waves. Part II: Influence of wind forcing and surface shear. *J. Phys. Oceanogr.*, **32**, 2559-2570.

Benney, D. J., and A. C. Newell, 1967: The propagation of nonlinear wave envelopes. *J.Math.Phys*, **46**, 133-139.

Bretherton, F. P., 1964: Resonant interactions between waves. The case of discrete oscillations. *J. Fluid Mech.*, **20**, 457-479.

Brueckner, K. A., and B. J. West, 1988: Vindication of mode-coupled descriptions of multiple-scale water wave fields. *J. Fluid Mech.*, **196**, 585–92.

Cavaleri, L. and Coauthors, , 2007: Wave modelling–The state of the art. *Prog. Oceanogr.*, **75**, 603-674.

Csanady, G. T., 2001: *Air-sea interaction: Laws and Mechanisms.* Cambridge Univ. Press,

Dommermuth, D., 2000: The initialization of nonlinear waves using an adjustment scheme. *Wave Motion*, **32**, 307-317.

Dommermuth, D. G., and D. K. P. Yue, 1987: A High-Order Spectral Method for the Study of Nonlinear Gravity-Waves. *J. Fluid Mech.*, **184**, 267-288.

Donelan, M. A., 1999: Wind-induced growth and attenuation of laboratory waves. *Wind-Over-Wave Couplings*, , 183–194.

Donelan, M. A., J. Hamilton, and W. H. Hui, 1985: Directional Spectra of Wind-Generated Waves. *Philosophical Transactions of the Royal Society of London.Series A, Mathematical and Physical Sciences (1934-1990)*, **315**, 509-562.

Donelan, M. A., A. V. Babanin, I. R. Young, and M. L. Banner, 2006: Wave-follower field measurements of the wind-input spectral function. Part II: Parameterization of the wind input. *J. Phys. Oceanogr.*, **36**, 1672-1689.

Dyachenko, A. I., and Y. V. Lvov, 1995: On the Hasselmann and Zakharov approaches to the kinetic equations for gravity waves. *J. Phys. Oceanogr.*, **25**, 3237-3238.

Ebuchi, N., Y. Toba, and H. Kawamura, 1992: Statistical study on the local equilibrium between wind and wind waves by using data from ocean data buoy stations. *J. Oceanogr.*, 48, 77-92.

Hara, T., and C. C. Mei, 1991: Frequency downshift in narrowbanded surface waves under the influence of wind. *J. Fluid Mech.,* **230**

Hasselmann K., T. Barnett, E. Bouws, H. Carlson, D. Cartwright, K. Enke, J. Ewing, H. Gienapp, D. Hasselmann, P. Kruseman, A. Meerburg, P. Miller, D. Olbers, K. Richter, W. Sell and H. Walden, 1973: Measurements of wind-wave growth and swell decay during the joint north sea wave project (JONSWAP), *Deutsche Hydrographische Zeitschrift* **12** (A8), 95 pp.

Huang, N. E., Z. Shen, and S. R. Long, 1999: A new view of nonlinear water waves: The Hilbert Spectrum. *Annu. Rev. Fluid Mech.,* **31**, 417-457.

Janssen, P., 2004: *The Interaction of Ocean Waves and Wind.* Cambridge University Press,

Janssen, P. A. E. M., G. J. Komen, and W. J. P. Voogt, 1987: Friction velocity scaling in wind wave generation. *Bound. -Layer Meteorol.,* **38**, 29-35.

Jeffreys, H., 1925: On the Formation of Water Waves by Wind. *Proceedings of the Royal Society of London. Series A, Containing Papers of a Mathematical and Physical Character,* **107**, 189-206.

Jeffreys, H., 1926: On the Formation of Water Waves by Wind (Second Paper). *Proceedings of the Royal Society of London. Series A, Containing Papers of a Mathematical and Physical Character,* **110**, 241-247.

Kalmykov, V. A., 1996: The interaction of surface waves in the presence of wind. *Phys. Oceanogr.,* **7**, 91-97.

Kalmykov, V. A., 1998: Phase velocities of surface waves in a sea of finite depth. *Phys. Oceanogr.,* **9**, 121-127.

Kawai, S., 1979: Generation of initial wavelets by instability of a coupled shear flow and their evolution to wind waves. *J. Fluid Mech.,* **93**, 661–703.

Kinsman, B., 1969: Historical notes on the original Beaufort scale. *Marine Observer,* **39**, 116-124.

Kinsman, B., 1965: *Wind waves, their generation and propagation on the ocean surface.* Prentice-Hall, 676 pp.

Komen, G. J., L. Cavaleri, M. Donelan, K. Hasselmann, S. Hasselmann, and P. Janssen, 1994: Dynamics and Modelling of Ocean Waves. Cambridge University Press, Cambridge.

Krasitskii, V. P., 1994: On reduced equations in the Hamiltonian theory of weakly nonlinear surface waves. *Journal of Fluid Mechanics (ISSN 0022-1120),* **272**

Kunishi, H., 1963: An experimental study on the generation and growth of wind waves. Bulletin of Disaster Prevention Research Institute, Kyoto Univ, 61, 1-41.

Liu, P. C., 2000: Is the wind wave frequency spectrum outdated. *Ocean Eng.,* **27**, 577-588.

Liu, P. C., D. J. Schwab, and R. E. Jensen, 2002: Has wind–wave modeling reached its limit? *Ocean Eng.,* **29**, 81-98.

Longuet-Higgins, M., 1969: On wave breaking and the equilibrium spectrum of wind-generated waves. *Proceedings of the Royal Society of London. Series A, Mathematical and Physical Sciences,* **310**, 151-159.

Longuet-Higgins, M. S., 1969: A nonlinear mechanism for the generation of sea waves. *Proceedings of the Royal Society of London. Series A, Mathematical and Physical Sciences,* **311,** 371-389.

Longuet-Higgins, M. S., and E. D. Cokelet, 1976: The deformation of steep surface waves on water. I. A numerical method of computation. *Proceedings of the Royal Society of London.Series A, Mathematical and Physical Sciences,* **350**, 1-26.

Longuet-Higgins, M. S., and R. W. Stewart, 1960: Changes in the form of short gravity waves on long waves and tidal currents. *J. Fluid Mech.,* **8.**

Lvov, Y. V., S. Nazarenko, and B. Pokorni, 2006: Discreteness and its effect on water-wave turbulence. *Physica D,* **218**, 24-35.

Mei, C. C., M. Stiassnie, and D. K. P. Yue, 2005: *Theory and applications of ocean surface waves.* World Scientific.

Melville, W. K., 1983: Wave modulation and breakdown. *J. Fluid Mech.,* **128**, 489-506.

Melville, W. K., 1996: The role of surface-wave breaking in air-sea interaction. *Annu. Rev. Fluid Mech.,* **28**, 279-321.

Onorato, M., A. R. Osborne, and M. Serio, 2007: On the relation between two numerical methods for the computation of random surface gravity waves. *European Journal of Mechanics/B Fluids,* **26**, 43-48.

Peirson, W. L., and A. W. Garcia, 2008: On the wind-induced growth of slow water waves of finite steepness. *J. Fluid Mech.,* **608**, 243-274.

Plant, W. J., 1982: A relationship between wind stress and wave slope. *Journal of Geophysical Research,* **87**, 1961-1967.

Rasmussen, J. H., and M. Stiassnie, 1999: Discretization of Zakharov's equation. *European Journal of Mechanics/B Fluids,* **18**, 353-364.

Schwartz, L. W., 1974: Computer extension and analytic continuation of Stokes' expansion for gravity waves. *J. Fluid Mech.,* **62**, 553-578.

Stewart, R. W., 1961: The wave drag of wind over water. *J. Fluid Mech.,* **10.**

Stewart, R. W., 1967: Mechanics of the Air—Sea Interface. *Phys. Fluids,* **10**, S47.

Stiassnie, M., and L. Shemer, 1984: On modifications of the Zakharov equation for surface gravity waves. *J. Fluid Mech.,* **143.**

Tanaka, M., and N. Yokoyama, 2004: Effects of discretization of the spectrum in water-wave turbulence. *Fluid Dyn. Res.,* **34**, 199-216.

Toba, Y., 1972: Local balance in the air-sea boundary processes. I. On the growth process of wind waves. *J. Oceanogr.,* **28**, 109-120.

Toba, Y., 1978: Stochastic form of the growth of wind waves in a single-parameter representation with physical implications. *J. Phys. Oceanogr.,* **8**, 494-507.

Toba, Y., 1997: The 3/2-power law for ocean wind waves and its applications. *Advances in Coastal and Ocean Engineering,* **3**, 31-66.

Toba, Y., 1998: Wind-forced strong wave interactions and quasi-local equilibrium between wind and windsea with the friction velocity proportionality. *Nonlinear Ocean Waves,* **59.**

Toba, Y., 2003: *Ocean-Atmosphere Interactions.* Kluwer Academic Pub,

Trulsen, K., and K. B. Dysthe, 1997: Frequency downshift in three-dimensional wave trains in a deep basin. *J. Fluid Mech.,* **352**, 359-373.

Tsai, W. T., and D. K. P. Yue, 1996: Computation of nonlinear free-surface flows. *Annu. Rev. Fluid Mech.,* **28**, 249-278.

Tulin, M. P., 2003: Future Directions in the Study of Nonconservative Water Wave Systems. *Journal of Offshore Mechanics and Arctic Engineering,* **125**, 3.

van Gastel, K., P. Janssen, and G. J. Komen, 1985: On phase velocity and growth rate of wind-induced gravity-capillary waves. *J. Fluid Mech.*, **161**, 199-216.

Veron, F., and W. K. Melville, 2001: Experiments on the stability and transition of wind-driven water surfaces. J. Fluid Mech., 446, 25-65.

Wu, H. Y., E. Y. Hsu, and R. L. Street, 1979: Experimental study of nonlinear wave-wave interaction and white-cap dissipation of wind-generated waves. Dyn. Atmos. Oceans, 3, 55-78.

Wu, G. Y., Y. M. Liu, and D. K. P. Yue, 2006: A note on stabilizing the Benjamin-Feir instability. *J. Fluid Mech.*, **556**, 45-54.

Yuen, H. C., and B. M. Lake, 1982: Nonlinear dynamics of deep-water gravity waves. *Adv. Appl. Mech.*, **22**, 67–229.

Zhang, J., K. Y. Hong, and D. K. P. Yue, 1993: Effects of Wavelength Ratio on Wave Modeling. *J. Fluid Mech.*, **248**, 107-127.